Voltage control of magnetism in multiferroic ferromagnetic/ferroelectric heterostructures

Veronica Sireus

ADVERTIMENT. L'accés als continguts d'aquesta tesi queda condicionat a l'acceptació de les condicions d'ús establertes per la següent llicència Creative Commons: http://cat.creativecommons.org/?page_id=184

ADVERTENCIA. El acceso a los contenidos de esta tesis queda condicionado a la aceptación de las condiciones de uso establecidas por la siguiente licencia Creative Commons: http://es.creativecommons.org/blog/licencias/

WARNING. The access to the contents of this doctoral thesis it is limited to the acceptance of the use conditions set by the following Creative Commons license: https://creativecommons.org/licenses/?lang=en

Universitat Autònoma
de Barcelona

Voltage control of magnetism in multiferroic ferromagnetic/ferroelectric heterostructures

Veronica Sireus

Tesi doctoral

Programa de Doctorat en Ciència de Materials

Jordi Sort Viñas (director)

Enric Menéndez Dalmau (director)

Departament de Física

Facultat de Ciències
2022

Universitat Autònoma
de Barcelona

Memòria presentada per aspirar al Grau de Doctor

Per

Veronica Sireus

Vist i plau

Dr. Jordi Sort Viñas (director)	Dr. Enric Menéndez Dalmau (director)

Bellaterra, 20/06/2022

El **Dr. Jordi Sort Viñas**, professor ICREA del Departament de Física de la Universitat Autònoma de Barcelona,

i el **Dr. Enric Menéndez Dalmau**, professor lector Serra Húnter del Departament de Física de la Universitat Autònoma de Barcelona,

CERTIFIQUEN que:

Veronica Sireus ha realitzat la seva tesi doctoral sota la seva direcció.

Que el disseny dels experiments, síntesi de mostres, llur caracterització, i la redacció d'aquesta memòria són fruit del treball d'investigació realitzat per Veronica Sireus.

I perquè així consti, signem el present certificat.

Dr. Jordi Sort Viñas Dr. Enric Menéndez Dalmau

Bellaterra, 20 de Junio de 2022

Abstract

This Thesis dissertation tackles the design, fabrication and magnetoelectric characterization of artificial multiferroic ferromagnetic/ferroelectric heterostructures; in particular, iron-aluminum/lead-magnesium-niobate-lead titanate (FeAl/PMN-PT). These hybrid systems are intended to reduce heat dissipation and power consumption when magnetoelectrically actuated.

One of the main strategies to control magnetism with voltage is the use of magnetostrictive/ferroelectric hybrid materials. However, different processes can occur simultaneously when these heterostructures are exposed to an electric field such as piezostrain-mediated effects, electronic charging, or voltage-driven oxygen migration (magnetoionics). This makes the interpretation of magnetoelectric effects not straightforward and, often, it leads to misconceptions. Because the induced strain (and variations in the magnetization) is proportional to the square of the ferroelectric polarization, the strain-mediated magnetoelectric response is usually symmetric with the sign of the applied voltage. Conversely, asymmetric responses can be obtained from electronic charging and voltage-driven oxygen migration. Here, ferromagnetic/ferroelectric heterostructures based on FeAl/[011]-oriented PMN-PT have been engineered in terms of layer thickness, composition, and microstructure to exhibit a highly asymmetric magnetoelectric response to be able to disentangle the aforementioned magnetoelectric effects. Specifically, Fe atomic % around 75 and large thicknesses (> 20 nm) allow dismissing any possible charge accumulation effect, whereas no evidence of magnetoionics is observed experimentally, as expected from the high resistance to oxidation of $Fe_{75}Al_{25}$, leaving strain as the only mechanism to modulate the asymmetric magnetoelectric response.

In parallel, this approach has been scaled down to microscale patterned FeAl dots on [011]-oriented PMN-32PT substrates, using UV-lithography. Interestingly, 50 nm thick $Fe_{75}Al_{25}$ (at. %) disks grown onto 10 nm Cu/[011]-oriented PMN-32PT show a range of magnetic properties, ranging from multidomain to vortex-like behavior, as a consequence of the interplay between in-plane magnetic properties and voltage actuation.

Resumen

La presente Tesis doctoral abarca el diseño, la fabricación y la caracterización magnetoeléctrica de heteroestructuras ferromagnéticas/ferroeléctricas artificiales; en particular, de hierro-aluminio/ niobato de plomo y magnesio - titanato de plomo (FeAl/PMN-PT). Estos sistemas híbridos están destinados a reducir la disipación de calor y el consumo de energía cuando se accionan magnetoeléctricamente.

Una de las principales estrategias para controlar el magnetismo con voltaje es el uso de materiales híbridos magnetostrictivos/ferroeléctricos. Sin embargo, cuando estas heteroestructuras se exponen a un campo eléctrico pueden producirse simultáneamente diferentes procesos, como los efectos mediados por la piezodeformación, la carga electrónica y la migración de oxígeno inducida por voltaje (magnetoiónica). Esto hace que la interpretación de los efectos magnetoeléctricos no sea sencilla y que, a menudo, se produzcan errores de interpretación. Dado que la deformación inducida (y las variaciones en la magnetización) son proporcionales al cuadrado de la polarización ferroeléctrica, la respuesta magnetoeléctrica mediada por la deformación suele ser simétrica respecto al signo de la tensión aplicada. Por el contrario, se pueden obtener respuestas asimétricas a partir de la carga electrónica y la migración de oxígeno inducida por voltaje. En esto caso, las heteroestructuras ferromagnéticas/ferroeléctricas basadas en FeAl y PMN-PT orientado según [011] han sido diseñadas en términos de espesor de capa, composición y microestructura para mostrar una respuesta magnetoeléctrica altamente asimétrica y poder desentrelazarlos efectos magnetoeléctricos mencionados. En concreto, el % atómico de Fe en torno al 75 y los grandes espesores (> 20 nm) permiten descartar cualquier posible efecto de acumulación de carga, mientras que no se observa experimentalmente ninguna evidencia de magnetoiónica, como era de esperar por la alta resistencia a la oxidación de la aleación $Fe_{75}Al_{25}$, lo que deja a la deformación como único mecanismo para modular la respuesta magnetoeléctrica asimétrica.
Paralelamente, este enfoque se ha miniaturizado a discos de FeAl en la microescala sobre sustratos de PMN-32PT orientados según [011], utilizando litografía UV.

Curiosamente, el comportamiento magnetoeléctrico de los discos de 50 nm de espesor de $Fe_{75}Al_{25}$ (at. %) crecidos sobre PMN-32PT orientado según [011], previamente cubierto con 10 nm de Cu, muestran una gama de propiedades magnéticas, que van desde el comportamiento multidominio hasta el de tipo vórtice, como consecuencia de la interacción entre las propiedades magnéticas en el plano y la actuación mediante voltaje aplicado.

Glossary

- <D>: Crystallite size
- A: Amplitude oscillation
- ADF: Annular dark field
- AEM: Analytical electron microscopy
- AFM: Atomic force microscopy
- B: Magnetic induction or magnetic flux density
- BTO: Barium titanate, $BaTiO_3$
- c-MFs: Composite multiferroic materials
- CME: Converse magnetoelectric effect
- d_{31}: Transverse piezoelectric coefficient 31
- d_{33}: Longitudinal piezoelectric coefficient 33
- DART: Dual amplitude resonance tracking
- DME: Direct magnetoelectric effect
- E-field: Electric field
- EDX: Energy dispersive X-ray analysis
- EELS: Electron energy loss spectroscopy
- FE: Ferroelectric
- FEG: Field emission guns
- FM: Ferromagnetic
- GIXRD: Grazing incidence X-ray diffraction
- GMR: Giant magnetoresistance
- H: Magnetic field
- $\hbar$: Reduced Plank constant
- HAADF: High angle annular dark field
- H_C: Coercivity
- H_{dm}: Demagnetizing field
- HRTEM: High-resolution transmission electron microscopy
- k_{33}: Electromechanical coupling factor
- L-MOKE: Longitudinal MOKE
- l: Orbital angular momentum
- m: Magnetic moment
- M: Magnetization
- MAE: Magnetic anisotropy energy

- ME-RAMs: Magneto-electric random-access memories
- MFM: Magnetic force microscopy
- MFs: Multiferroic materials
- MOKE: Magneto-optical Kerr effect
- MPB: Morphotropic phase boundaries
- M_R: Remanence
- M_R/M_S: Squareness ratio
- MRAMs: Magnetic random-access memories
- M_S: Saturation magnetization
- MTJ: Magnetic tunnel junction
- P-MOKE: Polar MOKE
- P: Polarization
- PFM: Piezoresponse force microscopy
- PMA: Perpendicular magnetic anisotropy
- PMN-PT: Lead magnesium niobate-lead titanate, (1-x) $Pb(Mg_{1/3}Nb_{2/3})O_3$–$xPbTiO_3$ (PMN-xPT)
- ϕ: Magnetic flux
- Q: Quality factor
- s-MFs: Single-phase multiferroic materials
- s: Intrinsic spin
- SEM: Scanning electron microscopy
- SI: International system of units
- SST-RAMs: Spin-transfer-torque random-access memories
- SST: Spin-transfer-torque
- STEM: Scanning transmission electron microscopy
- T-MOKE: Transversal MOKE
- T_C: Curie temperature
- TEM: Transmission electron microscopy
- UV- Photolithography: Ultraviolet photolithography
- V: Volume
- VCM: Voltage control of magnetism
- VSM: Vibrating sample magnetometer
- XRD: X-ray diffraction
- β_C: Cauchy contribution to the integral peak width β
- β_G: Gaussian contribution to the integral peak width β

- $H_{applied}$: External magnetic field
- λ: Magnetostrictive coefficient
- λ: Wavelength
- μ: Permeability
- μ_0: Permeability of free space
- μ_B: Bohr magneton
- μ_r: Relative permeability
- ρ: Density
- χ: Magnetic susceptibility

Table of contents

Abstract VII

Resumen VIII

Glossary X

Table of contents XIII

1. Introduction 3

1.1 Essentials on magnetism 3

- 1.1.2 Magnetization as a function of the applied magnetic field: hysteresis loops 8
- 1.1.3 Magnetic recording 10

1.2 Voltage control of magnetism 14

- 1.2.1 Magnetoelectricity and multiferroics 14
- 1.2.2 Converse magnetoelectric (ME) effect 15
  - 1.2.2.1 Intrinsic ME coupling 16
  - 1.2.2.2 Charge accumulation (i.e., direct field effects) 16
  - 1.2.2.3 Voltage-driven ion migration mechanism 17
  - 1.2.2.4 Strain-mediated mechanism 18

1.3 Why FeAl/PMN-PT heterostructures? 19

- 1.3.1 FeAl alloys as ferromagnetic materials 19
- 1.3.2 Lead magnesium niobate- lead titanate (PMN-PT) as ferroelectric material 22

References 26

2. Experimental methods 37

2.1 Sample preparation 37

- 2.1.1 Sputtering 37
  - 2.1.1.1 Sputtering ratio 40

    2.1.1.2 Experimental details 41
  2.1.2 UV Photolithography 41
    2.1.2.1 Experimental details 43
2.2 Structural and morphological techniques 45
  2.2.1 X-ray diffraction 45
    2.2.1.1 Modes of XRD 47
      2.2.1.1.1 Bragg-Brentano 47
      2.2.1.1.2 Grazing Incidence 48
    2.2.1.2 Experimental details 48
  2.2.2 Scanning electron microscopy (SEM) 49
    2.2.2.1 Experimental details 51
  2.2.3 Transmission electron microscopy (TEM) 51
    2.2.3.1 Imaging and diffraction mode 54
    2.2.3.2 STEM 56
    2.2.3.3 Experimental details 57
  2.2.4. Atomic force microscopy (AFM) 57
    2.2.4.1 Experimental details 60
2.3 Magnetic characterization techniques 60
  2.3.1 Vibrating sample magnetometry (VSM) 60
  2.3.2. Magneto-optical Kerr effect (MOKE) 62
  2.3.3. Magnetic force microscopy (MFM) 65
    2.3.3.1. Experimental details 65
2.4 Electric characterization 66
  2.4.1 Ferroelectric hysteresis measurements (Polarization-Field loops) 66
    2.4.1.1. Experimental details 67
  2.4.2 Piezoresponse force microscopy (PFM) 67
    2.4.2.1. Experimental details 69
2.5 Magnetoelectric characterization 70

2.5.1 Magnetoelectric characterization of the thin film with vibrating sample magnetometry (VSM) 70
2.5.2 Magnetoelectric characterization of the lithographed sample with magneto-optical Kerr effect (MOKE) 72
2.5.2.1 Longitudinal and transverse MOKE 72
2.5.2.2 Polar MOKE 73
References 76

3. Results and discussion **82**
3.1 Voltage control of magnetism in continuous FeAl/PMN-32PT 83
3.1.1 Heterostructures preparation 83
3.1.2 Structural and morphological characterization 83
3.1.3 Ferroelectric characterization 87
3.1.4 Magnetic characterization 88
3.1.5 Magnetoelectric characterization 89
3.1.6 Discussion 95
3.2 Voltage control of magnetism in patterned FeAl dots on PMN-32PT 101
3.2.1 Heterostructures preparation 101
3.2.2 Morphological characterization 102
3.2.3 Ferroelectric characterization 103
3.2.4 Magnetoelectric characterization 107
3.2.5 Discussion 120
References 124

4. Conclusions **129**
4.1 Voltage control of magnetism in continuous FeAl/PMN-32PT 129
4.2 Voltage control of magnetism in patterned FeAl dots on PMN-32PT 130

5. Future perspectives 135

6. Curriculum vitae 139

1

Introduction

1. Introduction

Today we are surrounded by devices that aim to simplify daily actions. From television to smartphones, through diagnostics and information storage, these devices have something in common: a magnetic component. The magnetic materials that compose them can be different depending on their use. Therefore, to better understand how these devices are made, the following subsections provide a brief explanation of magnetism and magnetic materials. Furthermore, all equations are expressed in the international systems of units (SI).

1.1 Essentials on magnetism

When a material is dipped into a magnetic field (H), such material responds to it. The way and the intensity of the response depend on the intrinsic nature of the material. The magnetic moment, m, for an isolated atom originates from the electrons' intrinsic spin and the electrons' orbital motion around the nucleus [1]. The magnetic moment, for an individual electron, is described by:

$$\mathrm{m} = -\frac{\mu_B}{\hbar}(\mathrm{l} + 2s) \qquad \mathrm{Eq.\,1}$$

Where: μ_B is the Bohr magneton ($\mu_B = 9.27 \times 10^{-24}$ JT^{-1}); ħ is the reduced Plank constant (ħ = 1.055 x 10^{-34} Js); l the orbital angular momentum and s the intrinsic spin. In condensed matter, the magnetic moments of the atoms add up and the magnetization M is defined as the magnetic moment per unit volume:

$$\mathrm{M} = \frac{\mathrm{m}}{\mathrm{V}} \qquad \mathrm{Eq.\,2}$$

The response of a certain material to an applied magnetic field H is called magnetic induction, or magnetic flux density B. A characteristic property of the material itself is the relation between H and B. There is a linear relation between B and H in vacuum, as shown in equation 3:

$$\mathrm{B} = \mu_0 \mathrm{H} \qquad \mathrm{Eq.\,3}$$

Where μ_0 is the permeability of free space ($\mu_0 = 4\pi \times 10^{-7}$ N·A^{-2}). The total magnetic field is described by $\mathrm{H} = \mathrm{H}_{\mathrm{applied}} + \mathrm{H}_{\mathrm{dm}}$, where $H_{applied}$ is the external magnetic field that exists in the absence of any magnetized material (i.e., the applied magnetic field), and H_{dm} is the demagnetizing field, that is created by the magnet, i.e., the magnetic field inside the magnetic material. Permeability (μ) can be interpreted, in the presence of H, as the ability a material has to arrange its spins in response to the magnetic field. Inside a magnetic material, B and H are different in terms of magnitude due to the magnetization M:

$$\mathrm{B} = \mu_0(\mathrm{H} + \mathrm{M}) \qquad \mathrm{Eq.\,4}$$

When the magnetization M is parallel to the magnetic field H one can define:

$$\mathrm{M} = \chi\mathrm{H} \qquad \mathrm{Eq.\,5}$$

Where χ is the magnetic susceptibility [1].

The linear relationship between B and H can be rewritten as follows:

$$\mathrm{B} = \mu_0(\mathrm{H} + \mathrm{M}) = \mu_0\mathrm{H} + \mu_0\chi\mathrm{H} = \mu_0(1 + \chi)\mathrm{H} = \mu_0\mu_r\mathrm{H} = \mu\mathrm{H} \qquad \mathrm{Eq.\,6}$$

Where $\mu_r = 1 + \chi$ is the relative permeability and μ_0 is the vacuum permeability. Typical values for the relative permeability are:

in vacuum: $\mu_r = 1$

in matter generally: $\mu_r \geq 1$

As mentioned before, the response of materials, when an external magnetic field is applied, depends on the intrinsic nature of the materials themselves. Furthermore, depending on the type of response, magnetic materials can be classified as follows (figure 1.1):

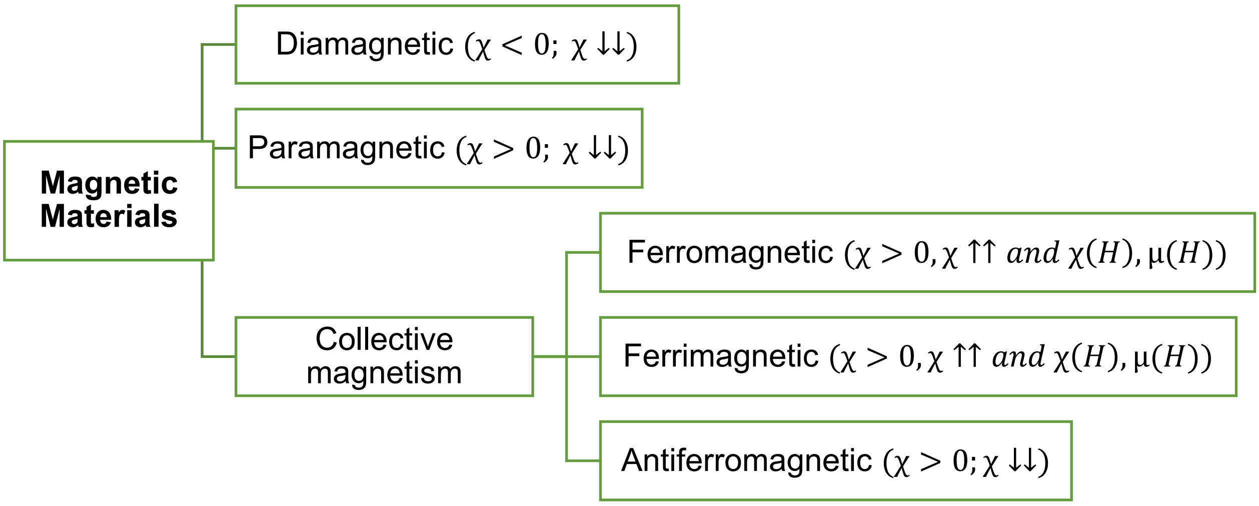
Magnetic Materials
Diamagnetic ($\chi < 0;\ \chi \downarrow\downarrow$)
Paramagnetic ($\chi > 0;\ \chi \downarrow\downarrow$)
Collective magnetism
Ferromagnetic ($\chi > 0, \chi \uparrow\uparrow and\ \chi(H), \mu(H)$)
Ferrimagnetic ($\chi > 0, \chi \uparrow\uparrow and\ \chi(H), \mu(H)$)
Antiferromagnetic ($\chi > 0; \chi \downarrow\downarrow$)

Figure 1.1. Diagram that illustrates the classification of magnetic materials; the term “collective magnetism” means “*a result of the exchange interaction between permanent magnetic dipoles*” [1,2].

- **Diamagnetism:** is an induction effect. Indeed, a magnetic field H causes magnetic dipoles to be antiparallel aligned with respect to the external field H. This is a reaction linked to the Lenz’s law. Hence, diamagnetism shows negative susceptibility:

$$\chi^{\mathrm{dia}} = \mathrm{const.} < 0 \qquad \mathrm{Eq.}\,7$$

All materials have diamagnetic components. In some cases, other contributions can overcome the weak diamagnetic signal. Furthermore, diamagnetic substances are usually composed of elements with orbital shells completed, with no unpaired electrons. Diamagnetism disappears, as it relies on the external magnetic field, after H is removed.

- **Paramagnetism:** The presence of non-interacting permanent magnetic dipoles is a key precondition for the existence of paramagnetism. The spins tend to align with the external magnetic field generating a small response. In paramagnets, exchange interactions are overcome by thermal fluctuation, so that spins become misaligned in the absence of H (figure 1.2 (c)). The susceptibility of paramagnetic materials is characterized by:

$$\chi^{\mathrm{para}} > 0 \qquad \mathrm{Eq.}\,8$$

$$\chi^{\mathrm{para}} = \chi^{\mathrm{para}}\,(\mathrm{T}) \qquad \mathrm{Eq.\,9}$$

In addition, the efficiency of the field in aligning the moments is opposed by the randomizing effects of temperature. This results in a temperature-dependent susceptibility, known as the Curie Law.

- **Ferromagnetism:** it is a type of *collective magnetism* in which the magnetic moments of neighboring atoms are aligned parallel to each other (positive exchange interactions). Spontaneous magnetization is observed when these materials are below a critical temperature, i. e. the magnetic moments exhibit an orientation which is not enforced by an external magnetic field. This critical temperature is the so-called Curie temperature [3], T_C, where:

$$\chi = \mathrm{C}\frac{\rho}{\mathrm{T} - \mathrm{T_C}} \qquad \text{and} \qquad 0 < \mathrm{T} < \mathrm{T_C} \qquad \mathrm{Eq.\,10}$$

Where C it is a characteristic constant of the material and ρ is density (figure 1.2 (a)).

- **Ferrimagnetism:** it is another type of *collective magnetism* in which the magnetic moments form two sublattices that are antiparallel to each other (negative exchange interactions) and exhibit different magnitude. Upon application of a magnetic field, even if some spins tend to oppose the applied H, the overall response does not vanish and, therefore, ferrimagnets have a positive net magnetic moment. In other words, the lattice degenerates into two ferromagnetic sublattice A and B of different magnetization both in terms of magnitude and direction (figure 1.2 (d)):

$$\mathrm{M_A} \neq \mathrm{M_B} \qquad \mathrm{Eq.\,11}$$

whereas

$$\mathrm{M} = \mathrm{M_A} + \mathrm{M_B} \neq 0 \qquad \text{for } \mathrm{T} < \mathrm{T_C} \qquad \mathrm{Eq.\,12}$$

with M being the total magnetization.

- **Antiferromagnetism:** this class of materials may be seen as consisting of two magnetic sublattices (A and B) which are oriented antiparallel and fully compensated. In this case, the critical temperature is called Néel temperature, T_N and it is characterized by:

$$|M_A| = |M_B| \neq 0 \quad \text{for } T < T_N \qquad \text{Eq. 13}$$

and

$$M_A = -M_B \quad (\text{e.g.}, \uparrow\downarrow\uparrow\downarrow\uparrow\downarrow) \qquad \text{Eq. 14}$$

Therefore, the total magnetization vanishes (figure 1.2 (b)):

$$M = M_A + M_B \equiv 0 \qquad \text{Eq. 15}$$

Above the critical temperature T_N, the collective interacting magnetism vanishes and shows a paramagnetic character.

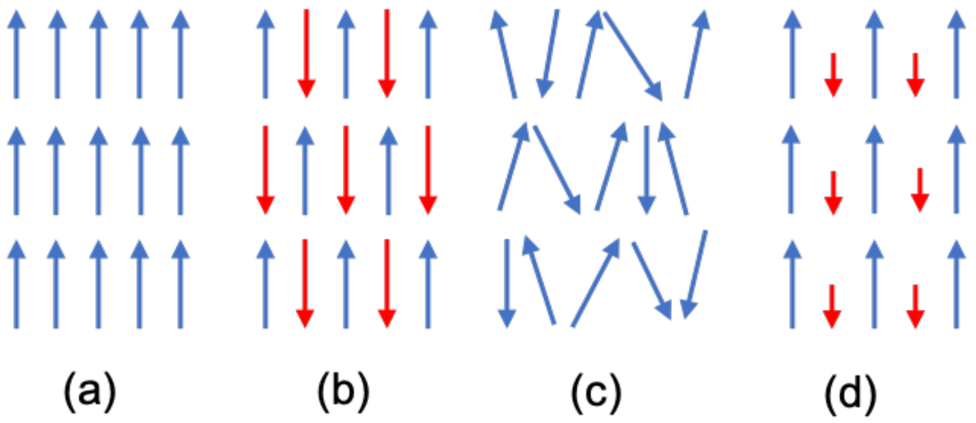

Figure 1.2. Spin arrangements in ferromagnetic (a); antiferromagnetic (b); paramagnetic (c) and ferrimagnetic materials (d). For the antiferromagnetic and ferrimagnetic materials, the blue and red arrows represent the two “ferromagnetic sublattices”.

1.1.2 Magnetization as a function of the applied magnetic field: hysteresis loop

As mentioned before, when a magnetic material is placed under the action of a magnetic field it will respond to it. The result is a hysteresis loop, or a curve, where magnetization (M) is plotted as a function of the external magnetic field ($H_{applied}$). These hysteresis loops are like “fingerprints” of the magnetic materials and determine their potential applications. The magnetic material must be imagined as a set of small magnetic domains. These domains are heavily dependent on several parameters, such as the exchange energy, magneto crystalline anisotropy that arises from the spin-orbit coupling and the electrostatic crystal field [4], magnetostatic energy that represents the self-induced energy (it is also responsible for the shape anisotropy since the demagnetization field is heavily dependent on sample’s shape), and an energy term which depends on the external applied field (Zeeman energy)) [1]. The energy balance among these contributions changes when the external magnetic field is swept from one value to another, giving rise to the hysteretic character of the ferromagnetic and ferrimagnetic materials, as shown in figure 1.3. For diamagnetic, antiferromagnetic, and paramagnetic materials, M vs. H shows a linear behavior with different slopes, negative for diamagnetic materials and positive for antiferromagnetic and paramagnetic. Moreover, important parameters can be extracted from a hysteresis loop, such as saturation magnetization (M_S), remanent magnetization (o remanence M_R), the so-called squareness ratio (M_R/M_S), or the coercivity (H_C).

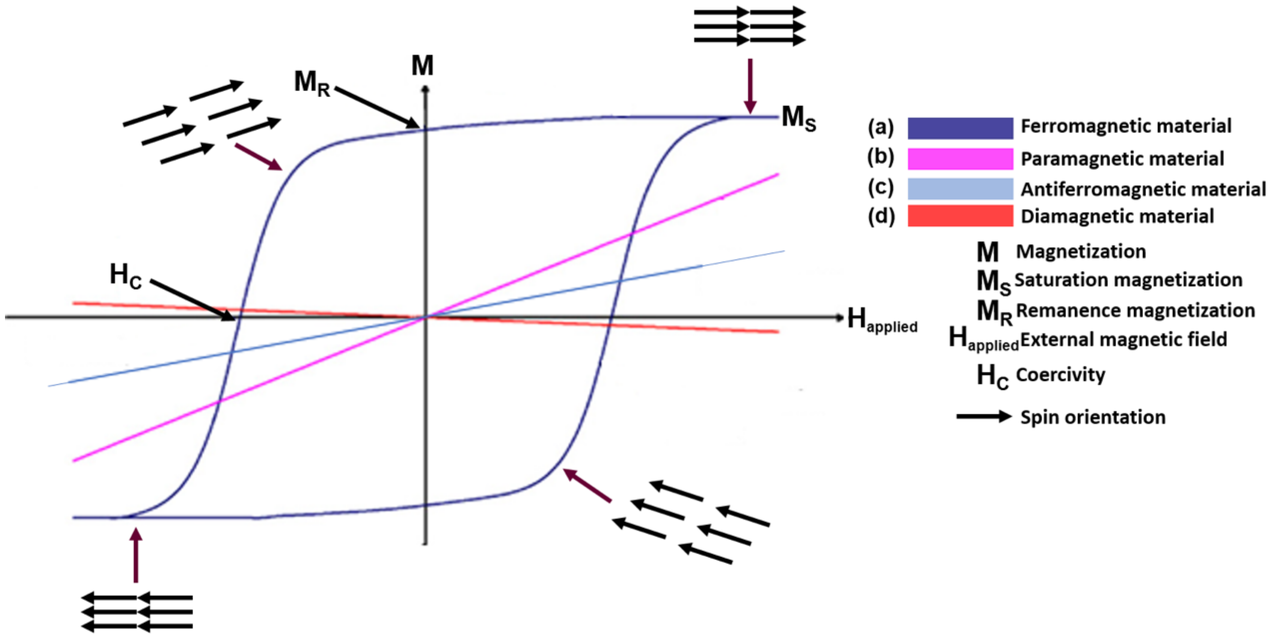
M
M_R
M_S
H_C
$H_{applied}$
(a) Ferromagnetic material
(b) Paramagnetic material
(c) Antiferromagnetic material
(d) Diamagnetic material
M Magnetization
M_S Saturation magnetization
M_R Remanence magnetization
$H_{applied}$ External magnetic field
H_C Coercivity
Spin orientation

Figure 1.3. M vs. $H_{applied}$ dependence for different magnetic materials. The different dependences are not to scale.

M_S represents the magnetization achieved by a material when all the moments are aligned along the direction of the applied magnetic field, while M_R is the magnetization that remains after saturation when $H_{applied}$ is brought back to zero. H_C accounts for the magnetic field needed to suppress the net magnetization remaining in the material.

Moreover, ferroelectric, and ferromagnetic materials have somewhat analogous properties. Ferroelectric (FE) materials are, by definition, those materials undergoing a phase transition from a high-temperature phase, that acts as an ordinary dielectric, to a low-temperature phase with a spontaneous polarization that can be switched via an applied electric field. The electric polarization, P (for FE), corresponding to the magnetization M (for FM); the electric field, E, corresponding to the magnetic field, H; and the electric displacement, D, corresponding to the magnetic flux density, B. FE materials have domains and show a hysteretic response of both polarization and electric displacement when an electric field is applied, as shown in figure 1.4 [5].

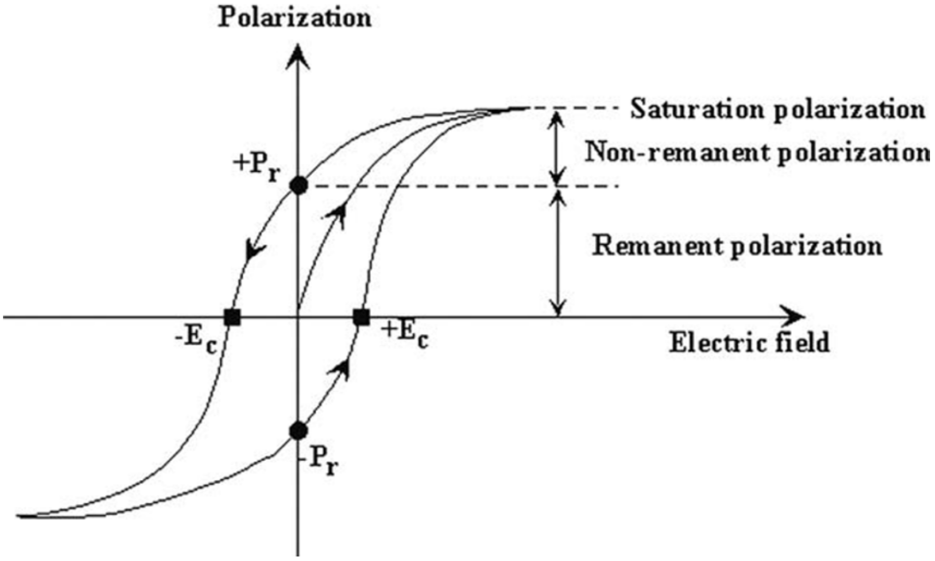

Figure 1.4. Representative P-E curve of a standard ferroelectric material [5].

At T_C, a very small external electrical field will cause a large polarization of these materials, hence, the onset of spontaneous electrical polarization coincides with the divergence in static dielectric permeability, ϵ. Moreover, the fact that their concentration of electric flux density coincides with high dielectric permeability means that these materials can be used as capacitors. They find application as electromechanical transducers and actuators, due to the change in electric polarization that is followed by a change in shape (i.e., they show piezoelectric behavior) [6, 7].

1.1.3 Magnetic recording

Digital information was traditionally stored in in-plane magnetic recording media. These tapes, with a 2D configuration, are usually created by embedding, in a polymer matrix, magnetic nanoparticles. The media is first in a demagnetized state, it means that the magnetization directions of the single magnetic domains are distributed randomly. Passing through the proximity of a recording head, the external local magnetic field is used to locally orient the magnetic material, as shown in figure 1.5. Conventionally, the magnetic recording was based on longitudinal recording media, where the bits were stored in the plane of the recording media. This design was widely used in the field of audio and video recording technology, although the information density was not so high [8]. Moreover, there were technical limitations related to the signal-to-noise ratio, which was proportional to the number of particles in a bit, or the protective coating and also the dispersion of magnetic characteristics. Reduction of grain size while guaranteeing stabilization against thermal fluctuations is required to increase storage capacity.

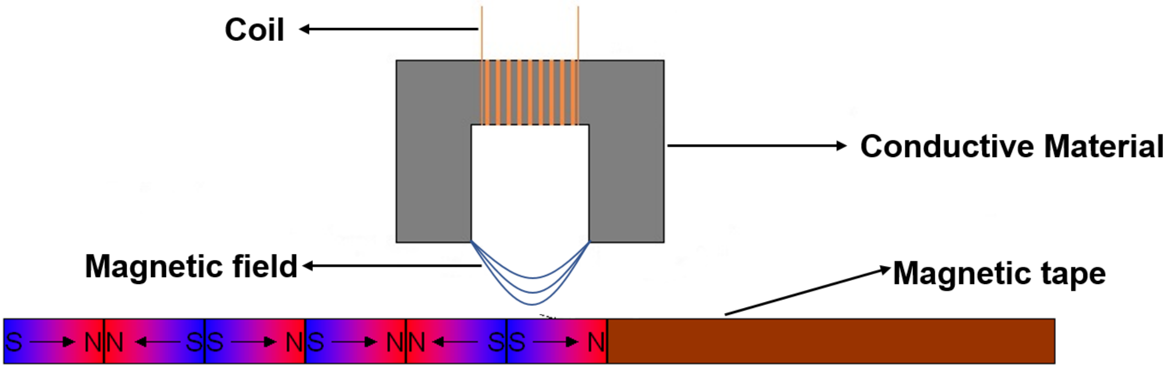

Figure 1.5. Schematic representation of an in-plane (longitudinal) magnetic recording medium [9].

Those systems were replaced later by devices that could store more information. They exploited the production of perpendicularly aligned bits. Massive data storage devices, for modern hard drives, usually consist of many single magnetic units (bits) where information is stored. These bits are made of materials with high magnetic anisotropy and coercivity, to provide stability to the stored data. The magnetization, for each bit, can be up or down, like a binary system (i.e., 1 for up and 0 for down for example), generating the binary codification for information storage, figure 1.6. This information, however, is not stored permanently since the orientation of bits is dynamically changed at will. The magnetic switching is conventionally achieved by locally applying an external magnetic field.

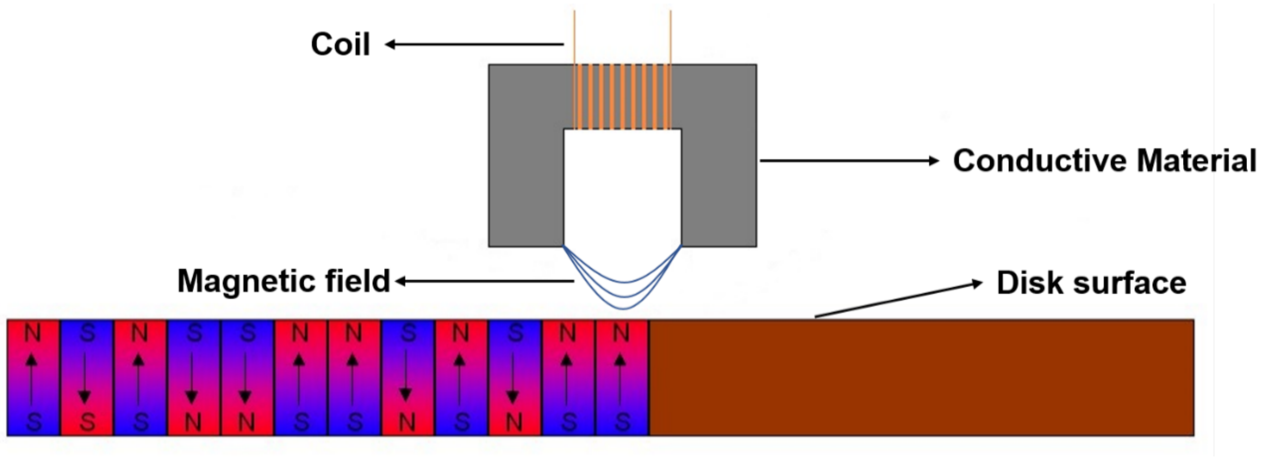

Figure 1.6. Schematic representation of an out-of-plane (perpendicular) magnetic recording medium [9].

However, in these devices, if the bit is too small, they become more sensitive to thermal fluctuations (≈ K_BT), increasing the need for materials with higher magnetic anisotropy. But if the anisotropy is too high, the local magnetic field needed to switch the bit is also significantly increased, requiring larger electromagnetic coils to generate it and, thus, making miniaturization difficult. In other words, reducing the storage density. Also, the need of larger applied fields implies higher electrical currents in the electromagnets which cause a large fraction of energy dissipated in the form of Joule heating effects.

In the last decades, extensive work on magnetic manipulation has been carried out to improve the performance of magnetically actuated devices. Current spintronic devices largely rely on *magnetoresistance*, which accounts for the change of electric conductivity due to the presence of a magnetic field. This effect was first discovered in 1856 by William Thompson (Lord Kelvin), but at that time it was not possible to modify electrical resistance using magnetic fields by more than 5%. This effect was given the name of anisotropic magnetoresistance (AMR) or spontaneous magnetoresistance anisotropy (SMA) [10].

Spintronics (spin-based electronics), also known as *magneto-electronics*, came into light by the advent of the so-called "Giant Magnetoresistance (GMR) effect" in 1988 [11]. GMR is a quantum mechanical effect observed in thin film heterostructures made up of two ferromagnetic layers separated by a non-ferromagnetic metallic spacer (e.g., Cu, Cr). Depending on the orientation of the ferromagnetic layers, there is a significant difference in terms of electrical resistance, when a magnetic field is applied. The antiparallel orientation of the ferromagnetic layers gives a higher resistance compared to the parallel orientation. GMR effect is much stronger than ordinary magnetoresistance. The use of antiferromagnetic materials (i.e., exchange bias) allows for a wider magnetic field range where the two ferromagnetic layers remain antiparallel. In these systems, the magnetization of one ferromagnetic layer is pinned, through the exchange coupling, with an adjacent antiferromagnetic layer, while the other magnetization, of the second ferromagnetic layer, is free to rotate with the applied magnetic field. These structures are the so-called “spin-valve”. This has allowed an increase in the performance of devices like read heads for hard disk drives and magnetic random-access memories (MRAMs).

When the space layer is an insulating barrier layer, instead of a non-magnetic metal, the multi-layer stacks is called “magnetic tunnel junction” (MTJ). As shown in figure 1.7, the stack is composed by a “free” ferromagnetic layer, a “spacer” oxide layer, a “pinned” ferromagnetic layer (where the direction of magnetization is fixed) and a “pinning” antiferromagnetic layer. Since both layers are enclosed between a word (source) line at the bottom and a read line at the top, these two lines provide the magnetic field needed to control the relative orientation of the free layer.

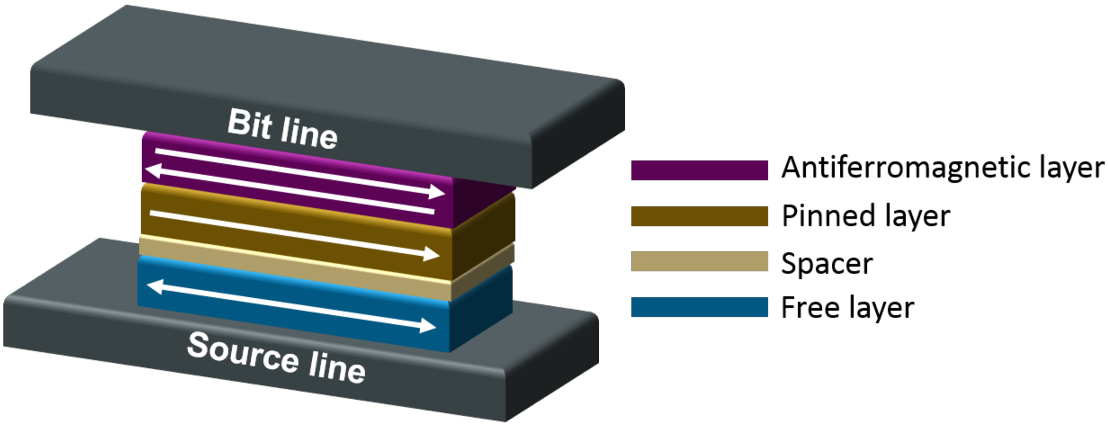

Figure 1.7. Scheme of a spin-valve of a MRAM, adapted from [12].

MRAMs consist of an ordered array of MTJs. The working principle is based on magneto-resistive effects. For a parallel configuration of the free and pinned layer, the electrons that pass through the tunnelling junction encounter lower resistance (0-bit for example), while when both are antiparallel, the high resistance state (1-bit) appears. An external magnetic field can assist the overturning of the free layer to switch from “0” to “1” states. However, sometimes, the magnetic field cannot be applied easily on a single MTJ, and it can affect the nearby memory units, which is a technological limitation.

The discovery of the spin-transfer-torque (STT) effect, where a spin-polarized current passes through a thin ferromagnet, overcame this problem. When the magnetization shows some tilt with respect to the direction of the spins of the electrons, torque is transferred from the current to the magnetization itself and, consequently, magnetization can switch without the need of external magnetic fields. This phenomenon increased the selectivity in the bit flip while reducing the total electric power consumption, during the magnetization reversal process [13]. On the one hand, this helps to produce more effective read-heads, on the other hand, all writing and reading processes are still current-mediated and, as a result, energy dissipation in the form of heat (Joule heating effects) is still present, which affect its efficiency. MRAMs, for example, require currents of the order of 10 mA, STT-RAMs, instead, need currents of about 0.5 mA.

In fact, when the voltage, V, is applied, the current, generated in the connection, will dissipate heat. This phenomenon is known as the Joule effect (eq. 16):

$$\mathrm{P} = \mathrm{VI} = \mathrm{RI}^2 \qquad \text{Eq. 16}$$

The power (P) of heating generated by an electrical conductor is proportional to the product of its resistance (R) and the square of the current (I).

Electromagnets are still the main way to manipulate magnetic elements in memory devices: to apply electrical currents in a solenoid (or coil) to generate the needed magnetic fields to switch the magnetization.

To overcome the energy-efficiency drawback, researchers are examining alternative methods for developing low-power-consumption devices. For example, the use of magneto-electric (ME) materials in ME-RAMs. The advantage is the use of electric voltage, instead of current as for the devices mentioned above, for significant power dissipation reduction. Furthermore, using electric fields to write in ME-RAM provides a benefit in terms of increased bit density. When incorporated in a circuit, magnetoelectric writing does not place a current-drive-based size limit on the access devices (e.g., transistors), enabling a much smaller overall cell area. Last but not the least, in principle, ME-RAMs retains all the benefits of STT-RAMs, i.e., high speed, high endurance, radiation hardness, and a possibility for nonvolatile operation.

1.2 Voltage control of magnetism

One of the strategies to reduce heat dissipation is to replace electric currents by electric fields (E-fields), i.e., manipulation of magnetism using voltage [14]. For this, a tunable, strong, and non-volatile ME coupling is required.

1.2.1 Magnetoelectricity and Multiferroics

With the term magnetoelectricity, we refer to a branch of Condensed Physics Matter in which magnetism and electricity coexist simultaneously. Röntgen discovered the magnetoelectric effect in a dielectric material for the first time in 1888 [15]. By moving a dielectric, a magnetic induction is generated when it is placed in an electric field. A few years later, P. Curie highlighted the possibility of intrinsic ME behaviour of (non-moving) crystal based on symmetric considerations [16]. Seventeen years after Röntgen, the reverse effects were reported: the polarisation of a moving dielectric material in a magnetic field [17], while the term "magnetoelectric" was used for the first time by Debye following the first attempts to experimentally demonstrate the static ME effects [18].

Therefore, the ME coupling effect can be separated into two categories: i) direct ME (DME) effect, i.e., electric response upon magnetic excitation, and ii) converse ME (CME) effect, i.e., magnetic response upon electric excitation. The so-called "multiferroics" (MF_S) materials have been the first candidates to show both effects.

Multiferroic materials are characterized by showing at least two ferroic orders, such as ferromagnetic or ferroelectric [19]. These materials, moreover, could be divided into two "families": single-phase multiferroics (s-MF_S), with intrinsic magnetoelectric coupling [20-22], and composite multiferroics (c-MF_S), where none of the counterparts has an intrinsic magnetoelectric coupling but each has one of the ferroic orders, where is understood as any type of ferroic ordering, including ferroelectric, ferromagnetic, antiferromagnetic and ferrimagnetic [19].

- **s-MF_S**: materials which possess two or more ferroic orders, for example, antiferromagnetic, ferroelectric and/or ferroelastic, which are mutually and intrinsically coupled. Depending on the field applied, magnetic or electric, these materials will suffer an internal electric polarization change (DME effect), or their magnetic response will be altered (CME effect).

$$\Delta \mathrm{P} = \alpha \Delta \mathrm{H}_{\mathrm{applied}} \quad \text{or} \quad \Delta \mathrm{E} = \alpha_{\mathrm{E}}\, \Delta \mathrm{H}_{\mathrm{applied}} \qquad \text{Eq. 17}$$

$$\Delta \mathrm{H}_{\mathrm{applied}} = \alpha_{-1} \Delta \mathrm{E} \qquad \text{Eq. 18}$$

Where P is the electrical polarization, E is the electric field, H is the applied magnetic field α_E is the DME coefficient and $\alpha_{-1}$is the CME coefficient. Single-phase multiferroics are further classified into two types: Type-I and Type-II. These two classes are mainly related to their different physical mechanism of electric polarization [23].

However, the restrictive use of these materials is because these multiferroic compounds exhibit low Curie temperatures (under room temperature), and a high inherent ME coupling (especially above room temperature) has not yet been found in single-phase compounds, except for the bismuth ferrite and rare-earth manganates materials [24-26].

- **c-MF$_S$:** are defined as compounds in which electric, magnetic and piezo-order states coexist within the material; however, unlike single-phase composites, these materials are distinguished by the fact that the order phases are physically separated from each other within the material itself [19]. In contrast to the s-MF$_S$, in most of these materials the coupling is usually mediated by elastic strain interactions [26]:

$$\mathrm{DME} = \frac{\mathrm{Magnetic}}{\mathrm{Elastic}} \times \frac{\mathrm{Elastic}}{\mathrm{Electric}} \qquad \mathrm{Eq.\,19}$$

$$\mathrm{CME} = \frac{\mathrm{Electric}}{\mathrm{Elastic}} \times \frac{\mathrm{Elastic}}{\mathrm{Magnetic}} \qquad \mathrm{Eq.\,20}$$

As voltage is applied to the piezoelectric part, it deforms and such induced strain is transmitted to the ferromagnetic material, in which magnetic changes can occur due to the inverse magnetostriction effect. In this case, although the coupling is achieved extrinsically through strain, strong ME couplings can be achieved readily at room temperature. The magnetic changes obtained are typically volatile, however, as they vanish after strain removal.

1.2.2 Converse magnetoelectric (ME) effect

The efficiency with which a material can convert electrical energy into magnetic energy is regulated by the converse ME coupling coefficient and is thus a crucial parameter for device considerations. In ME heterostructures, the ME phenomenology can be classified in: Intrinsic ME [27-30]; Charge accumulation (i.e., direct field effects) [31-39]; FM/piezoelectric heterostructure (i.e., extrinsic multiferroics) [40-44], and redox/ion migration [45-49]. The cause of these phenomena is complex and, usually, two or more effects may occur at the same time [50]. In the following sub-paragraph, each effect is briefly described.

1.2.2.1 Intrinsic ME coupling

In 2015, Wang and co-authors [51] reported useful criteria for evaluating the potential of using single-phase multiferroic materials, namely: i) combination of FM and FE properties; ii) high FM and FE transition temperatures -the temperature should preferably be much higher than room temperature (RT)-, and iii) at high temperature, a strong ME coupling should occur. In addition to these three criteria, the ability to control these materials using low external electric or magnetic fields would be an added value. Materials that combine antiferromagnetic or antiferroelectric order parameters can also be included in this group. Researchers have been attracted to $BiFeO_3$, $TbMnO_3$ [52,53], $HoMnO_3$ [54,55], and CuO [56], but none of these materials fulfil all requirements, in particular some of them have FM and FE ordering at temperatures much lower than RT.

Bismuth ferrite ($BiFeO_3$, BFO) is the most well-known single-phase multiferroic material. Due to its high Néel temperature (T_N, around 673 K) and high FE Curie temperature (T_C, around 1043 K, in which it loses its spontaneous electric polarization), ferroelectric, piezoelectric, and antiferromagnetic order parameters are stable in this material at RT [28]. BFO has a G-type antiferromagnetic spin structure in bulk form and, above T_N, BFO loses its antiferromagnetic properties. These properties are complex because the spins, in the crystal structure, follow a spin spiral structure with a zero net magnetic moment [57]. In thin-film form, instead, it shows weak ferromagnetism from the antiferromagnetic spin canting, resulting from the suppression of its spiral spin structures [58]. However, a large ferroelectric polarization, $\sim 60\ \mu C/cm^2$, has been demonstrated in BFO epitaxial thin films [59,60]. Moreover, it has been reported an important magnetic moment change with a modest value of the electrical polarization, a good value of dielectric constant, thus showing ferroelectric and ferromagnetism in the same phase [61].

1.2.2.2 Charge accumulation (i.e., direct field effects)

As reported by Hu et al., charge-mediated ME effects in magnetic/dielectric heterostructures might imply the following processes: i) establishment of the electric field (E) across the dielectric capacitor; ii) E-modulation of the interfacial magnetic anisotropy of the magnet; iii) processional magnetization switching [50]. Ohno et. al, in 2000 [31], published one of the first works where it was demonstrated that it was possible to isothermally tune the Curie temperature of (In, Mn)As thin films with voltage. Some years later, in 2003, in the presence of a small external field, researchers from the same group were able to electrically switch and demagnetize thin films of similar composition [32]. Important work was published in 2007 by Weisheit et al. who reported charge-mediated ME effects in metals and not only in semiconductors [62]. Upon voltage application, the coercivity in ultrathin metallic ferromagnet could be tuned with voltage, due to an effect of charge accumulation in the ferromagnet, which causes a change in the magnetic anisotropy energy (MAE). The thickness also plays an important role. The electric field in metals is confined at the surface of the material, within the so-called Thomas-Fermi screening length (< 1 nm) [63, 64]. The interfacial nature of this phenomenon in metallic films is related to the electric screening length of metals, typically of a few unit cells [65]. For this reason, the materials studied are typically in the form of ultra-thin films, to enlarge the surface-to-volume ratio. Perpendicular magnetic anisotropy (PMA) is very appealing for applications since it allows for a larger magnetic density packaging [35]. In several works, it was demonstrated change on PMA upon voltage application [36,66-73]. Domain wall motion has also been studied systematically under E-field actuation [74]. Lu et al. [75] demonstrated that, under voltage application, domain wall propagation velocity could be either increased or reduced with voltage and they also showed that the nucleation and propagation of domains became altered, in agreement with previous work from Herrera et al. [76].

1.2.2.3 Voltage-driven ion migration mechanism

Electric field-induced oxygen motion in magnetic materials, or magneto-ionics [46, 48], was first observed in ferromagnet/solid-electrolyte heterostructures. It involves three dynamical processes: i) establishment of the electric field across the solid electrolyte; ii) electric field-induced migration of charged defects (either the oxygen vacancies [45-47,49] or H^+ [48]) to the interface between the magnetic material, typically Co or Fe, and the solid electrolyte; iii) interfacial redox reaction: the solid electrolyte serves as an ion reservoir and depending on the voltage polarity, accept or donates oxygen ions. [50]. Depending on the papers, the main groups that work on this topic, usually, used the term “redox” instead of the magneto-ionic control of magnetism [77,78]. Others, on the other hand, distinguish between the two effects because the redox process involves, when reversibility is possible, an oxidation-reduction reaction of a starting metallic, or metal oxide, material leads to changes in the oxidation state of the metal (or oxidize metal). Therefore, it requires oxygen from the surrounding (i.e., oxidative liquid media) and mainly affects the magnetic material surface [79-82]. Nowadays, the term indicates the voltage-driven ionic motion (i.e., ion diffusion) in magnetic materials. Sometimes, in the oxide-containing systems, the material itself can include the source of structural oxygen. Specifically, the whole system consists of an oxide layer, or heterostructure, which includes an oxide counterpart that has the function of an oxygen acceptor or oxygen donor. This mechanism has indeed revolutionized VCM because it may allow a voltage-driven modulation of magnetic properties such as coercivity, exchange bias field or magnetic anisotropy [47,83,84]. As mentioned before, one of the main problems is the very slow processes. Room-temperature ionic motion involves times between 10^1-10^3 s that, in terms of frequency rate, is 10^{-1}-10^{-3} Hz, as reported by Bauer and co-authors in ultra-thin Co layers, by voltage-driven oxygen migration from GdO_x, to switch the magnetic state, such as the magnetic anisotropy easy axis from in-plane to out-of-plane and vice versa [46]. Afterwards, different groups demonstrated that the domain wall motion could be tuned with an electric field, in magnetic films and nanowires, using AlO_x or GdO_x gating [74, 85-88]. Navarro-Senent et al. [89] recently reviewed the general mechanisms responsible for voltage control of magnetism and its future application. In 2019 [90], Tan and co-authors, using a small gate voltage and H^+ pumping in all-solid state heterostructures, have demonstrated reversible and non-destructive toggling of magnetic anisotropy at room temperature. They may avoid the problem of magnetic changes being followed by chemical and structural changes in the target ferromagnet, which is sometimes an irreversible process. The employment of these systems, among other things, enables for magneto-ionic switching rates of the order of 100ms, as a result, it has potential for applications such as neuromorphic computing.

1.2.2.4 Strain-mediated mechanism

In FM/FE heterostructures, strain-mediated effects imply three processes: i) creation of a piezoelectric electric field, ii) generation of strains on the piezoelectric's surface, and iii) strain-driven magnetization switching in the ferromagnet [50]. The voltage control of magnetic parameters, such as magnetic anisotropy, coercivity or even phase transition has been very successful in strain mediated composite multiferroics [91]. From the seventies, with the first studies [92], huge efforts have been made on the study of magnetoelectric effects in bulk [93]. The coupling depends heavily on the number of structural defects, any residual stresses and clamping effects. It was demonstrated, furthermore, the intrinsic dependence of the magnetic properties of a 10 nm thick body-centered cubic iron grown on a (100) $BaTiO_3$ (BTO) substrate [94]. BTO is a FE material with several structural transitions [95] during cooling, from high temperature, a $BaTiO_3$ crystal goes through a cubic to tetragonal transition at 393 K, then a transition to the monoclinic structure at 278 K, and finally to the rhombohedral structure at 183 K. These changes in structural configuration can reflect on a thin layer of iron grown on top, such as a change of the in-plane coercivity [96]. Notwithstanding numerous promising results [95,96], strain-mediated ME effects are governed by the interface between both FM/FE materials, determining the strength of the coupling. A crucial role is also played by the nature of the FE material. Indeed, most of the FE substrates are oxide-based. Partial oxidation of the interface is inevitable when depositing metals on top [97], it worsens the interface efficiency and, subsequently, the ME coupling [98,99]. In addition, if the FM/FE multilayer thin film is growing onto a substrate the achievable strain is limited. The mechanical clamping effect with the substrate limits the strength of the induced ME effect. While, if the FM thin film is directly grown onto a piezoelectric substrate, it is necessary to take into account its thickness. The E-field is inversely proportional to the thickness of the insulator, hence, to achieve a reasonable electric field, high voltages must be used. Moreover, many of the substrates used are also ferroelectric, besides being piezoelectric that contributes to potential charge accumulation at the interface, giving rise to the so-called charge-mediated ME effect. Therefore, because all FE materials are piezoelectric too, the combined effect is likely to occur, entangling each contribution [100-103]. In this thesis, a condenser-like configuration was used, described in Chapter 2 in detail.

1.3 Why FeAl/PMN-PT heterostructures?

The choice of the magnetic and dielectric materials, the thickness of the thin film, the crystal orientation and the operation mode of the electric field plays an important role in voltage control of magnetism. From a technological viewpoint, the solid-state system configuration requires a reproducible, strong and tunable ME effect. One of the mechanisms, with the largest possible voltage-driven modulation of the magnetic properties, is given from the strain-mediated converse magnetoelectric effects in magnetostrictive-piezoelectric hybrids materials (artificial multiferroics). Namely, FM/FE (with strong piezoelectric properties) heterostructures are typically used. Concerning the magnetostriction material, FeAl is a suitable candidate who shows strong magnetostriction, namely the deformation degree of a body in response to a change in its direction of magnetization through the application of a magnetic field [104] (for actuators and sensor a large magnetostrictive coefficient, λ, is required), soft ferromagnetism and a low cost [105]. As a FE material, a single crystal of lead magnesium niobate-lead titanate (PMN-PT), with ultra-high piezoelectric behaviour, is used in our work [100, 106].

1.3.1 FeAl alloys as ferromagnetic materials

As mentioned before, FeAl alloys are interesting FM materials due to their high magnetostrictive constant [107]. In addition, they have a very rich magnetic phase diagram. For these reasons, FeAl alloys have attracted considerable interest from researchers over the years. The ordered Fe_3Al ($D0_3$) and FeAl phases were first discovered by Bradley and Jay in Fe-rich and Fe-Al alloys in 1932 [108]. Thereafter, several different phase diagrams for these alloys were proposed [109-114], shown in figure 1.8. The alloys are paramagnetic, at RT, with this amount of Al, but they evolve towards a FM state as structural disorder increase. The Fe-rich alloys have an ordered B2 type structure in which the Fe atoms occupy the α sites, while the Al atoms and the remaining Fe atoms occupy the β sites at random (see figure 1.9). Hernando et al. demonstrated, in a ball-milled Fe-40 at. % Al alloy, that a significant contribution to the magnetization of these materials stems from changes in the lattice parameter caused by the order (paramagnetic-B2)-disorder (ferromagnetic-A2) transition, as shown in figure 1.9 [115,116]. Menéndez and co-authors [117] in 2008 reported on the correlation between structural (lattice cell parameter, atomic intermixing, etc.), magnetic and mechanical (microhardness) properties indicate that the induced ferromagnetism is mainly controlled by both cell expansion and atomic intermixing at low-stress-range processing, and, at high-stress regime, lattice expansion is the main cause of the ferromagnetic response.

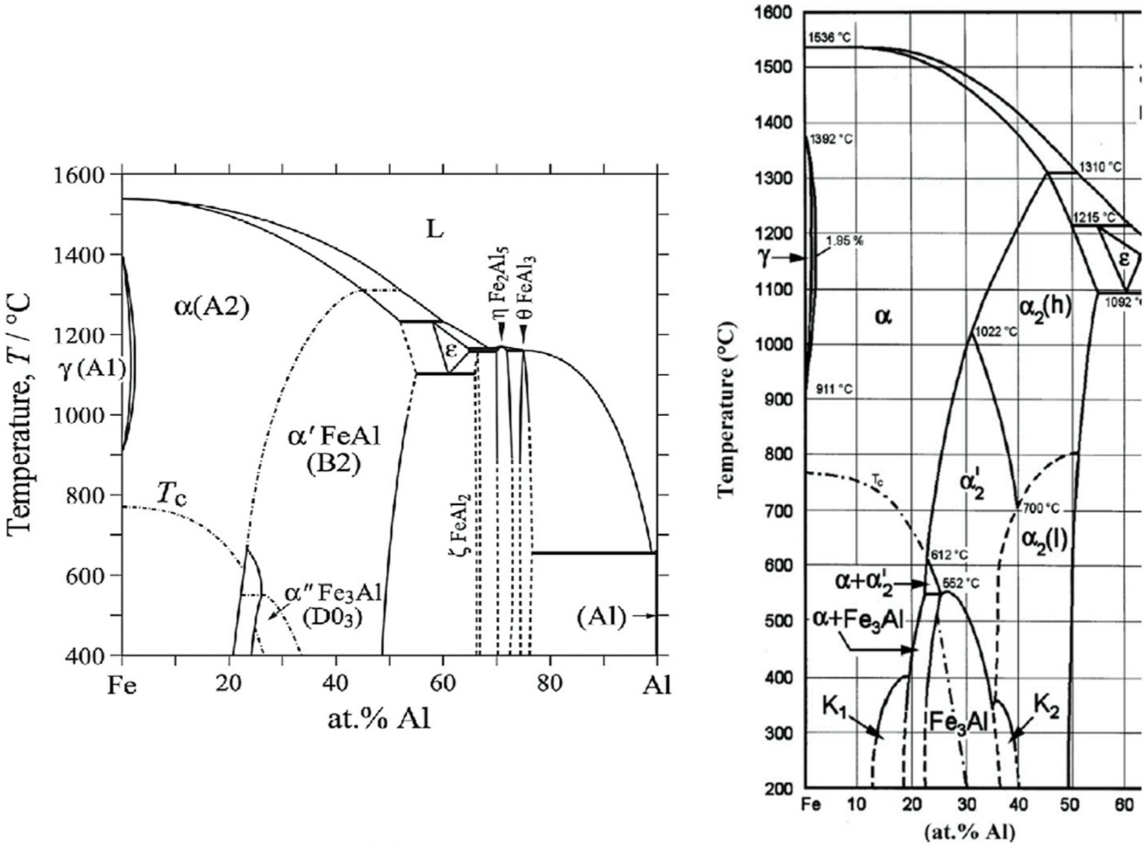

(a) **(b)**

Figure 1.8. Fe-Al binary diagram (a) [112]; Fe-rich part of Fe-Al system according to Kubaschewski [118].

Furthermore, if the aluminum quantity increases further, the magnetic moment decreases more rapidly and becomes zero for alloys with x ≥ 0.32 as reported by Taylor and Jones in 1958 [109] and readapted by Menéndez in his PhD thesis [119] (see figure 1.9). Nonetheless, at room temperature, atomically ordered $Fe_{1-x}Al_x$ alloys with x > 0.32 can become FM, after being disordered, i.e., atomically intermixed [109].

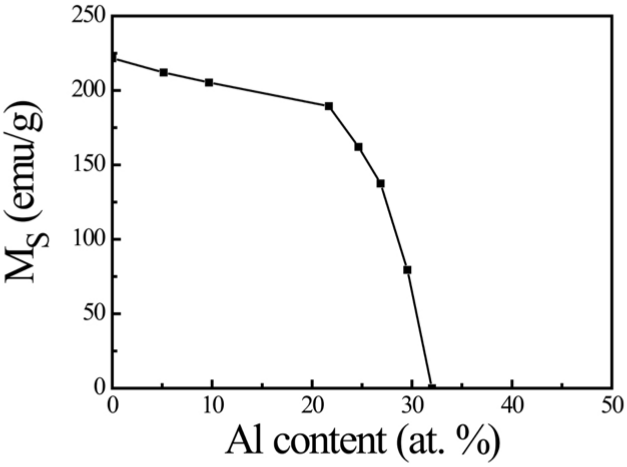

Figure 1.9. Dependence of the saturation magnetization, M_S, respect to the aluminum content, for $Fe_{1-x}Al_x$ system [119] adapted from [109].

Moreover, some studies report the temperature dependence of the magnetostriction and the magnetoelastic coupling in FeAl alloy with different amounts of Al. Clark et al. [120] have demonstrated a significant difference between RT measurements and other magnetostriction measurements for the higher Al concentration alloy, i. e. 16.6 %, 21.5% and 26.3 % of Al. Changes in magnetostriction with temperature are small for Fe-Al alloy having the disordered bcc phase (A2, figure 1,10 a) structure, with 19 at. % of Al. The alloy with the ordered D03 structure (figure 1.10 c), on the other hand, shows an anomalous decrease in magnetostriction in λ_{100} when reducing temperature.

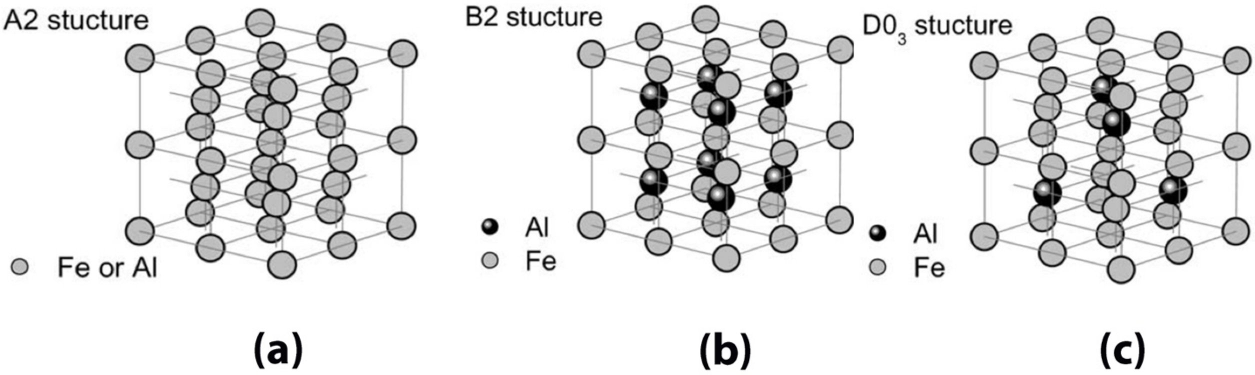

Figure 1.10. Different type of Fe-Al structure: (a) A2; (b) B2 and (c) $D0_3$ [121].

Recently, Mehmood et al. [105] have reported an interesting study about the magnetostriction in $Fe_{100-x}Al_x$ polycrystalline system, were $x = 15, 19, 25$. A fundamental issue to increase the magnetostriction in these materials is the phase stabilization of the disordered bcc structure, achieved by applying different heat treatments. Moreover, the results obtained show that the lattice constant is independent of the Al substitution in this concentration range. Furthermore, the high magnetostriction value (λ_{100}) for the 25 at. % Al makes it a valid candidate to engineering multiferroic FM/FE heterostructure.

1.3.2. Lead magnesium niobate- lead titanate (PMN-PT) as ferroelectric material

Lead-based piezoelectric materials are widely used materials due to their strong piezoelectric behavior. The pure lead titanate, $PbTiO_3$, structure, shown in figure 1.11, is not used as a piezoelectric, but this can either be mixed to obtain materials with excellent piezoelectric properties in the form of a solid solution. The $PbTiO_3$ belongs to the perovskite family with a chemical structure ABO_3. At room temperature it is ferroelectric with tetragonal $C_{4v}^1 - P4mm$ space group. Besides, it undergoes a first-order phase transition at 220 K into cubic $O_4^1 - Pm3m$. Nelmes et al. suggested that this phase transition exhibits mixed displacive and order-disorder character [122].

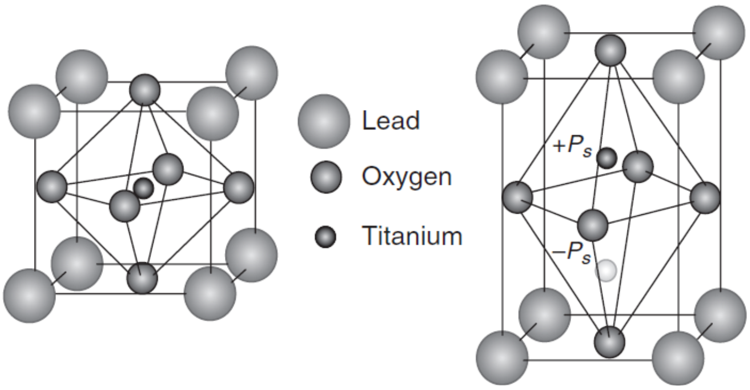

Figure 1.11. The perovskite crystal structure of $PbTiO_3$ (left); shift of titanium in the tetragonal phase resulting in a net polarization along [001] (*c*-axis) in the tetragonal phase (right) [123].

A solid solution with typical chemical structure $Pb(B'_{1/3}B''_{2/3})O_3$ or $Pb(C'_{1/2}C''_{1/2})O_3$, and ferroelectrics like $PbTiO_3$ are known as “relaxor-ferroelectrics” materials. Adding relaxor induces an increase of the permittivity, electromechanical coupling and piezoelectric coefficient especially for the compositions close to the morphotropic phase boundaries (MPB). The most used relaxor are $Pb(Zn_{1/3}Nb_{2/3})O_3$ known as PZT, or $Pb(Mg_{1/3}Nb_{2/3})O_3$, PMN, shown in figure 1.12. PMN was first synthesized by Smolenskii and Agranovskaya in 1958, in the late 1960s, the research of relaxor materials began with studies on PMN’s single crystal. For PMN the highest symmetry phase is cubic with $\mathrm{Pm3m}$ space symmetry and lattice constant a = 4.04 Å. It was demonstrated that the PMN undergoes a diffuse phase transition with a temperature range between -3 to -15 °C [124, 125].

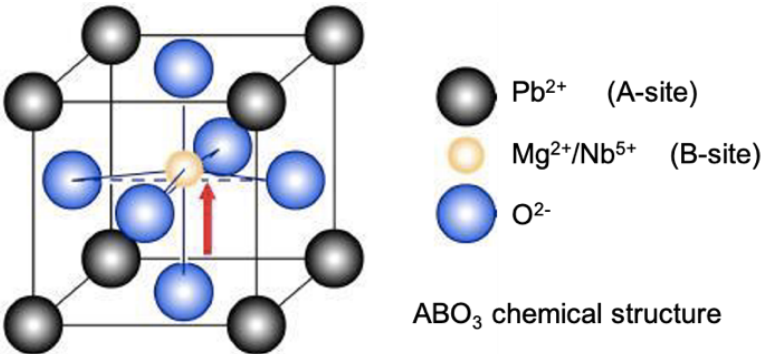

Figure 1.12. Representation of the chemical structure of the PMN perovskite unit cell.

As shown in figure 1.12, in the crystal structure, Pb^{2+}, occupies the corner (A-site), while Mg^{2+} or Nb^{5+} occupy the B-site, but it does not exist an idealized perovskite lattice-like figure 1.11, since the two ions are distributed at random. Moreover, the crystallography, the phase transitions and the other physical properties are affected by the B-site cation order. The frustration of local polarization, which prevents long-range ferroelectric order from developing completely, is a characteristic of the relaxor state. While rhombohedral is the local symmetry of the polar domains, PMN's macroscopic symmetry remains cubic below maximum permittivity temperature [126].

In the literature, there are different phase diagrams reported for PMN-PT solid solution, like figure 1.13, where the composition range of the MPB changes a little bit [127]. For example, Ghasemifard et al. have reported that the range is between $0.27 < \mathrm{x} < 0.34$. The MPB is a frontier between the rhombohedral (pseudo-cubic) and tetragonal phases. The rhombohedral phase is characterized by being the relaxor side with $R3m$ space group, while the tetragonal one is the FE side with space group $\mathrm{P4mm}$ [128]. Additionally, the monoclinic phase can be divided into two areas: (i) a phase with a space group Cm $(\mathrm{M_A type})$ located between $0.27 < \mathrm{x} < 0.30$, and (ii) a phase with a space group Pm $(\mathrm{M_C\ type})$ stable in the composition range $0.31 < \mathrm{x} < 0.34$ [129]. It has been demonstrated that a single crystal of PMN-PT with composition near the MPB exhibit a very high piezoelectric coefficient $(\mathrm{d_{33}} > 2500\,\mathrm{pC/N})$, extremely large piezoelectric strains (> 1.7%) and a high electromechanical coupling factor $(\mathrm{k_{33}} > 92\%)$ [128]. Another important parameter, to consider, is the so-called transverse piezoelectric coefficient d_{31}. For the PMN-PT, with PT composition close to the MPB, $\mathrm{d_{31}} \approx -1750\ \mathrm{pC/N}$. When an electric field is applied along z (i. e., in our case along [110] direction for the continuous thin film and along [011] for the patterned sample), this property allows for deformation in x and y, resulting in a change of the magnetic properties of the FM films deposited on top.

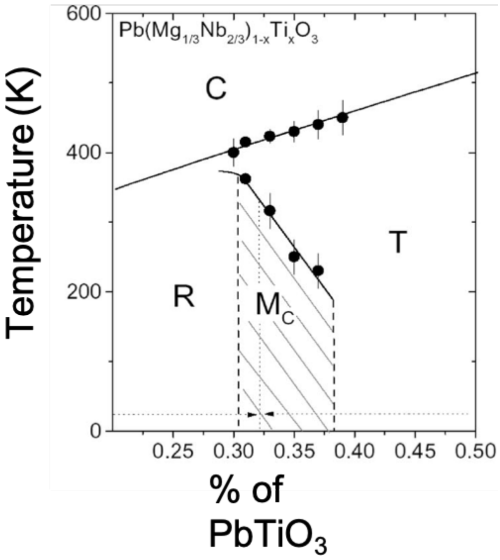

Figure 1.13. Phase diagram of PMN-PT solid solution. R, T, C and M means rhombohedral, tetragonal, cubic, and monoclinic regions respectively (diagonally shade area), modified from [127-130].

An interesting study done by Yin and co-authors [131], showed how the quantity of PT influences the material's properties as a relaxor or FE. They have reported that a relaxor like behavior is shown when the amount of PT is low (i.e., 24%). Whereas a typical ferroelectric material behavior is observed if the PT is approximately 35%. Subsequently, in 2002 Zhao and co-authors [132] published a paper where they proved that the composition, close to the MPB, influences the dielectric and piezoelectric performance. This publication showed that not only the composition influences the dielectric and piezoelectric properties but also the crystal orientation and the poling field [133-135].

In PMN-PT single and polycrystalline samples, a broad range of properties was measured. The peculiar response in this crystal has been attributed to a statistical inhomogeneity in the distribution of the Mg^{2+} and Nb^{5+} ions in the ABO_3, perovskite structure B-sites. This leads to a distribution of micro-volumes, having different Curie temperatures, within the samples. There is thus a Curie temperature range on cooling from high temperature rather than a single Curie point, and within this Curie range, the crystal exhibits an intimate combination of paraelectric and ferroelectric regions [136,137].

References

1. M. Getzlaff, *Fundamentals of Magnetism*, Springer-Verlag Berlin Heidelberg (2008)
2. B. D. Cullity, C. D. Graham, *Introduction to magnetic materials,* IEEE/Wiley, New Jersey (2009)
3. K. H. J. Buschow, F. R. de Boer, *Physics of Magnetism and Magnetic Materials*, Kluwer Academic / Plenum Publishers, New York (2003)
4. J. M. D. Coey, *Magnetism and magnetic materials,* Cambridge University Press, New York (2014)
5. N. Izyumskaya, Y. -I. Alivov, S. -J. Cho, H. Morkoç, H. Lee, Y. -S. Kang, Crit. Rev. Solid State, **32**, 111 (2007)
6. L. E. Cross, *Mater. Chem. Phys.*, **43**, 108 (1996)
7. N. A. Hill, *J. Phys. Chem. B*, **104**, 6694 (2000)
8. S. Khizroev, M. Kryder, Y. Ikeda, K. Rubin, P. Arnett, M. Best, D. A. Thompson, Recording *heads with trackwidths suitable for 100 Gbit/in2 density*, *IEEE Trans. Magn*. **35**, 2544 (1999)
9. https://www.hardwaresecrets.com/how-perpendicular-recording-works/2/
10. H. Ebert; A. Vernes; J. Banhart, "*Magnetoresistance, Anisotropic*" in "*Encyclopedia of Materials: Science and Technology"* (2nd edition), Elsevier (*2001*)
11. M. N. Baibich, J. M. Broto, A. Fert, F. Nguyen Van Dau, F. Petroff, P. Eitenne, G. Creuzet, A. Friederich and J. Chazelas *Phys. Rev. Lett.* **61**, 21 (1988)
12. A. Quintana Puebla, *PhD Thesis,* Universitat Autonoma de Barcelona, Spain (2018)
13. S. Bhatti, R. Sbiaa, A. Hirohata, H. Ohno, S. Fukami, S. N. Piramanayagam, *Mater. Today* **20**, 530 (2017)
14. B. Dieny, R. C. Sousa, J. Hérault, C. Papusoi, G. Prenat, U. Ebels, D. Houssameddine, B. Rodmacq, S. Auffret and L. D. Buda-Prejbeanu, J. Nanothecnol. **7**, 591 (2010)
15. W. C. Röntgen, *Ann. Phys.*, **35**, 264 (1888)
16. P. Curie, *J. Physique,* **3**, 393 (1894)

17. H. A. Wilson, *Phil. Trans. R. Soc. A*, **204** 129 (1905)
18. P. Debye, *Z. Phys.*, **36**, 300 (1926)
19. M. M. Vopson, *Crit. Rev. Solid State Mater. Sci.* **0**, 1, (2014)
20. W. Eerenstein, N. D. Mathur, and J. F. Scott, *Nature* **442**, 759 (2006)
21. G. Catalan and J. F. Scott, *Adv. Mater.* **21**, 2463 (2009)
22. N. Izyumskaya, Y. Aliyov, and H. Morkoç, *Crit. Rev. Solid State Mater. Sci.* **34**, 89 (2009)
23. D. Khomskii, Physics **2**, 20, (2009)
24. A.M. Kadomtseva, S. S. Krotov, Yu. F. Popov, G. P. Vorob'ev, Low *Temp. Phys.*, **32**, 709 (2006)
25. S. Valencia, A. Crassous, L. Bocher, V. Garcia, X. Moya, R. O. Cherifi, C. Deranlot, K. Bouzehouane, S. Fusil, A. Zobelli, A. Gloter, N. D. Mathur, A. Gaupp, R. Abrudan, F. Radu, A. arthélémy, M. Bibes, *Nature Materials*, **10**, 753 (2011)
26. C. A. F. Vaz, J. Hoffman, C. H. Ahn, R. Ramesh, *Adv. Mat.*, **22**, 2900 (2010)
27. H. Modarresi, *PhD Thesis,* Aerenberg Doctoral School, Leuven (2019)
28. J. Wua, Z. Fan, D. Xiao, J. Zhu, J. Wang, *Prog. Mater. Sci.*, **84**, 335 (2016)
29. S.-W. Cheong, M. Mostovoy, *Nat. Mat.*, **6**, 13 (2007)
30. Y. Wang, J. Li, D. Viehland, *Mat. Today*, **17**, 6 (2014)
31. H. Ohno, D. Chiba, F. Matsukura, T. Omiya, E. Abe, T. Dietl, Y. Ohno, and K. Ohtani, *Nature* **408**, 944 (2000)
32. D. Chiba, M. Yamanouchi, F. Matsukura, and H. Ohno, *Science* **301**, 943 (2003)
33. D. Chiba, M. Sawicki, Y. Nishitani, Y. Nakatani, F. Matsukura, and H. Ohno, *Nature* **455**, 515 (2008)
34. Y. Yamada, K. Ueno, T. Fukumura, H. T. Yuan, H. Shimotani, Y. Iwasa, L. Gu, S. Tsukimoto, Y. Ikuhara, and M. Kawasaki, *Science* **332**, 1065 (2011)
35. T. Maruyama, Y. Shiota, T. Nozaki, K. Ohta, N. Toda, M. Mizuguchi, A. A. Tulapurkar, T. Shinjo, M. Shiraishi, S. Mizukami, Y. Ando, and Y. Suzuki, *Nat. Nanotechnol*. **4**, 158 (2009)
36. M. Endo, S. Kanai, S. Ikeda, F. Matsukura, and H. Ohno, *Appl. Phys. Lett*. **96**, 212503 (2010)

37. F. A. Cuellar, Y. H. Liu, J. Salafranca, N. Nemes, E. Iborra, G. Sanchez-Santolino, M. Varela, M. G. Hernandez, J. W. Freeland, M. Zhernenkov, M. R. Fitzsimmons, S. Okamoto, S. J. Pennycook, M. Bibes, A. Barth.l.my, S. G. E. te Velthuis, Z. Sefrioui, C. Leon, and J. Santamaria, *Nat. Commun*. **5**, 4215 (2014)

38. H. J. A. Molegraaf, J. Hoffman, C. A. F. Vaz, S. Gariglio, D. van der Marel, C. H. Ahn, and J.-M. Triscone, *Adv. Mater*. **21**, 3470 (2009)

39. D. Chiba, S. Fukami, K. Shimamura, N. Ishiwata, K. Kobayashi, and T. Ono, *Nat. Mater*. **10**, 853 (2011

40. J.-M. Hu, C.-G. Duan, C.-W. Nan, and L.-Q. Chen, *NPJ Comput. Mater*. **3**, 18 (2017)

41. J.-M. Hu, L.-Q. Chen, and C.-W. *Nan, Adv. Mater*. **28**, 15 (2016)

42. P. B. Meisenheimer, S. Novakov, N. M. Vu, and J. T. Heron, *J. Appl. Phys*. **123**, 240901 (2018)

43. C. Song, B. Cui, F. Li, X. Zhou, and F. Pan, *Prog. Mater. Sci*. **87**, 33 (2017)

44. A. Molinari, H. Hahn, and R. Kruk, *Adv. Mater*. **31**, 1806662 (2019)

45. C. Bi, Y. Liu, T. Newhouse-Illige, M. Xu, M. Rosales, J. W. Freeland, O. Mryasov, S. Zhang, S. G. E. te Velthuis, and W. G. Wang, *Phys. Rev. Lett*. **113**, 267202 (2014)

46. U. Bauer, L. Yao, A. J. Tan, P. Agrawal, S. Emori, H. L. Tuller, S. van Dijken, and G. S. D. Beach, *Nat. Mater*. **14**, 174 (2014)

47. D. A. Gilbert, A. J. Grutter, E. Arenholz, K. Liu, B. J. Kirby, J. A. Borchers, and B. B. Maranville, *Nat. Commun*. **7**, 12264 (2016)

48. A. J. Tan, M. Huang, C. O. Avci, F. Büttner, M. Mann, W. Hu, C. Mazzoli, S. Wilkins, H. L. Tuller, and G. S. D. Beach, *Nat. Mater*. **18**, 35 (2019)

49. H.-B. Li, N. Lu, Q. Zhang, Y. Wang, D. Feng, T. Chen, S. Yang, Z. Duan, Z. Li, Y. Shi, W. Wang, W.-H. Wang, K. Jin, H. Liu, J. Ma, L. Gu, C. Nan, and P. Yu, *Nat. Commun*. **8**, 2156 (2017)

50. J.-M. Hu and C. W. Nan, *APL Mater.*, **7**, 080905 (2019)

51. J. Wang, Z. Fu, R. Peng, M. Liu, S. Sun, H. Huang, L. Li, R. J. Knize, and Y. Lu, *Mater. Horiz.,* **2**, 232 (2015)
52. T. Kimura, T. Goto, H. Shintani, K. Ishizaka, T. Arima and Y. Tokura, *Nature*, **426**, 55 (2003)
53. S.-W. Cheong and M. Mostovoy, *Nature Mater*., **6**, 13 (2007)
54. T. Lottermosera and M. Fiebig, *Phys. Rev. B*, **70**, 220407 (2004)
55. I. A. Sergienko, C. Sen and E. Dagotto, *Phys. Rev. Lett*., **97**, 227204 (2006)
56. T. Kimura, Y. Sekio, H. Nakamura and T. Siegrist, *Nature Mater*., **7**, 291 (2008)
57. F. Huang, Z. Wang, X. Lu, J. Zhang, K. Min, W. Lin, R. Ti, T. Xu, J. He, C. Yue, and J. Zhu, *Scientific reports*, **3**, 2907 (2013)
58. H. Béa, M. Bibes, S. Petit, J. Kreisel, and A. Barthélémy, *Philos. Mag. Lett.*, **87**, 165 (2007)
59. M. K. Singh, H. M. Jang, S. Ryu, M.H. Jo, *Appl. Phys. Lett.*, **88**, 042907 (2006)
60. J. Wang, J. B. Neaton, H. Zheng, V. Nagarajan, S. B. Ogale, B. D. Viehland, V. Vaithyanathan, D. G. Schlom, U. V. Waghmare, N. A. Spaldin, K. M. Rabe, M. Wuttig1, R. Ramesh, *Science*, **299**, 1719 (2003)
61. K. Singh, R. K. Kotnala, M. Singh, *Appl. Phys. Lett*., **93**, 212902 (2008)
62. M. Weisheit, S. Fähler, A. Marty, Y. Souche, C. Poinsignon, D. Givord, *Science* **315**, 349 (2007)
63. I. V. Ovchinnikov and K. L.Wang, *Phys. Rev. B* **79**, 020402(R) (2009)
64. M. Zhernenkov, M. R. Fitzsimmons, J. Chlistunoff, J. Majewski, I. Tudosa, and E. E. Fullerton, *Phys. Rev. B,* **82**, 024420 (2010)
65. C.-G. Duan, J. P. Velev, R. F. Sabirianov, Z. Zhu, J. Chu, S. S. Jaswal, E.Y. Tsymbal, *Phys. Rev. Lett.,* **101**, 137201 (2008)
66. K. Nakamura, R. Shimabukuro, Y. Fujiwara, T. Akiyama, T. Ito, *Phys. Rev. Lett*. **102**, 187201 (2009)
67. W.-G. Wang, M. Li, S. Hageman, C. L. Chien, *Nat. Mater.,* **11**, 64 (2011)
68. A. Rajanikanth, T. Hauet, F. Montaigne, S. Mangin, S. Andrieu, *Appl. Phys. Lett.,* **103**, 062402 (2013)

69. S.-S. Ha, N.-H. Kim, S. Lee, C.-Y. You, Y. Shiota, T. Maruyama, T. Nozaki, Y. Suzuki, *Appl. Phys. Lett.,* **96**, 142512 (2010)
70. F. Bonell, S. Murakami, Y. Shiota, T. Nozaki, T. Shinjo, Y. Suzuki, *Appl. Phys. Lett.* **98**, 232510 (2011)
71. T. Nozaki, Y. Shiota, M. Shiraishi,1 T. Shinjo, Y. Suzuki, *Appl. Phys. Lett.* **96**, 022506 (2010)
72. Y. Kikuchi, T. Seki, M. Kohda, J. Nitta, K. Takanashi, *Phys. D Appl. Phys*. **46**, 285002 (2013)
73. Y. Hibino, T. Koyama, A. Obinata, T. Hirai, S. Ota, K. Miwa, S. Ono, F. Matsukura, H. Ohno, D. Chiba, *Appl. Phys. Lett*., **109**, 082403 (2016)
74. A. Bernand-Mantel, L. Herrera-Diez, L. Ranno, S. Pizzini, J. Vogel, D. Givord, S. Auffret, O. Boulle, I. M. Miron, G. Gaudin, *Appl. Phys. Lett*., **102**, 122406 (2013)
75. Y. T. Liu, G. Agnus, S. Ono, L. Ranno, A. Bernand-Mantel, R. Soucaille, J.-P. Adam, J. Langer, B. Ocker, D. Ravelosona, L. Herrera Diez, *J. Appl. Phys*., **120**, 023901 (2016)
76. L. Herrera Diez, A. Bernand-Mantel, L. Vila, P. Warin, A. Marty, S. Ono, D. Givord, L. Ranno, *Appl. Phys. Lett.,* **104**, 082413 (2014)
77. K. Duscheka, M. Uhlemanna, H. Schlörba, K. Nielscha, K. Leistner, *Electrochem. Commun*., **72**, 153 (2016)
78. J.F. Monteiroa, Yu. A. Ivanovaa, A.V. Kovalevskya, D.K. Ivanoua, J.R. Fradea, *Electrochim. Acta* **193**, 284 (2016)
79. N. Di, J. Kubal, Z. Zeng, J. Greeley,2 F. Maroun, P. Allongue, *Appl. Phys. Lett.* **106**, 122405 (2015)
80. L. Reichel, S. Oswald, S. Fahler, L. Schultz, K. Leistner, *J. Appl. Phys.,* **113**, 143904 (2013)
81. K. Duschek, D. Pohl, S. Fähler, K. Nielsch, K. Leistner, *APL Mater.,* **4**, 032301 (2016)
82. K. Leistner, N. Langea, J. Hänischa, S. Oswalda, F. Scheibac, S. Fähler, H. Schlörba, L. Schultz, *Electrochim. Acta,* **81**, 330 (2012)
83. R. Mishra, D. Kumar, H. Yang, *Phys. Rev. Appl*., **11**, 054065 (2019)
84. A. Quintana, E. Menéndez, M. O. Liedke, M. Butterling, A. Wagner, V. Sireus, P. Toruella, S. Estradé, F. Peirò, J. Dendooven, C. Detavernier, P. D. Murray, D. A. Gilbert, K. Liu, E. Pellicer, J. Nogues, J. Sort, *ACS Nano*, **12**, 10291 (2018)

85. A. Schellekens, A. van den Brink, J. Franken, H. Swagten, and B. Koopmans, *Nat. Commun.*, **3**, 847 (2012)

86. U. Bauer, S. Emori, and G. S. D. Beach, *Nat. Nanotechnol*, **8**, 411 (2013)

87. D. Chiba, M. Kawaguchi, S. Fukami, N. Ishiwata, K. Shimamura, K. Kobayashi, and T. Ono, *Nat. Commun.*, **3**, 888 (2012)

88. U. Bauer, S. Emori, and G. S. D. Beach, *Appl. Phys. Lett.,* **100**, 192408 (2012)

89. C. Navarro-Senent, A. Quintana, E. Menèndez, E. Pellicer, J. Sort, *Appl. Phys. Lett*. **113**, 152901 (2018)

90. A. J. Tan, M. Huang, C. O. Avci, F. Büttner, M. Mann, W. Hu, C. Mazzoli, S. Wilkins, H. L. Tuller and G. S. D. Beach, *Nat. Mater.*, **18**, 35 (2019)

91. J. P. Velev, S. S. Jaswal, E. Y. Tsymbal, *Phil. Trans. R. Soc. A* **369**, 3069–3097 (2011)

92. J. Suchtelen, Philips *Res. Repts*. **27**, 28–37 (1972)

93. J. Ma, J. Hu, Z. Li, C.-W. Nan, *Adv. Mater.* **23**, 1062–1087 (2011)

94. S. Sahoo, S. Polisetty, C.-G.Duan, S. S. Jaswal, E. Y. Tsymbal, C. Binek *Phys. Rev. B,* **76**, 092108 (2007)

95. H. F. Kar and P. Vousden, *Philos. Mag.*, **40**, 1019 (1949)

96. R. O. Cherifi, V. Ivanovskaya, L. C. Phillips, A. Zobelli, I. C. Infante, E. Jacquet, V. Garcia, S. Fusil, P. R. Briddon, N. Guiblin, A. Mougin, A. A. Ünal, F. Kronast, S. Valencia, B. Dkhil, A. Barthélémy, M. Bibes, *Nat. Mater.,* **13**, 345 (2014)

97. T. J. Regan, H. Ohldag, C. Stamm, F. Nolting, J. Lüning, and J. Stöhral. R. L. White *Phys. Rev. B.* **64**, 214422 (2001)

98. S. Couet, M. Bisht, M. Trekels, M. Menghini, C. Petermann, M. J. Van Bael, J.-P Locquet, R. Rüffer, A. Vantomme, K. Temst, *Adv. Funct. Mater.,* **24**, 71 (2013)

99. M. Bisht, S. Couet, V. Lazenka, H. Modarresi, R. Rüffer, J.-P. Locquet, M. J. Van Bael, A. Vantomme, K. Temst, *Adv. Mater. Interfaces,* **3**, 1500433 (2015)

100. T. Nan, Z. Zhou, Mi. Liu, X. Yang, Y. Gao, B. A. Assaf, H. Lin, S. Velu, X. Wang, H. Luo, J. Chen, S. Akhtar, E. Hu, R. Rajiv, K. Krishnan, S. Sreedhar, D. Heiman, B. M. Howe, G. J. Brown, N. X. Sun, *Sci. Rep.,* **4**, 3688 (2014)

101. L. Shu, Z. Li, J. Ma, Y. Gao, L. Gu, Y. Shen, Y. Lin, C. W. Nan, *Appl. Phys. Lett.,* **100**, 022405 (2012).
102. J.-M. Hu, C.-W. Nan, and L.-Q. Chen, *Phys. Rev. B,* **83**, 134408 (2011)
103. J. Heidler, M. Fechner, R. V. Chopdekar, C. Piamonteze, J. Dreiser, C. A. Jenkins, E. Arenholz, S. Rusponi, H. Brune, N. A. Spaldin, and F. Nolting, *Phys. Rev., B*, **94**, 014401 (2016)
104. M. R. J. Gibbs, Modern trends in magnetostriction study and application, *Kluwer Academic Publishers: London,* pp 1-12, (2001)
105. Mehmood, N., Turtelli, R. S., Grössinger, R. & Kriegisch, M. Magnetostriction of polycrystalline Fe100-xAlx (x= 15,19,25). J. Magn. Magn. Mater. 322, 1609 (2010)
106. M. Liu, O. Obi, J. Lou, Y, Chen, Z. Cai, S, Stoute, M. Espanol, M. Lew, X, Situ, K. S, Ziemer, V. G. Harris and N. Sun, *Adv. Funct. Mater*., **19**, 1826 (2009)
107. R. Grössinger, R. Sato Turtelli, N. Mehmood, IOP Conf. Ser.: Mater. Sci. Eng., **60**, 012002 (2013)
108. A. J. Bradley, A. H. Jay, *Proc. R. Soc. Lond. A*, **136**, 210 (1932)
109. A. Taylor, R. M. Jones, *J. Phys. Chem. Sol.*, **6**, 16 (1958)
110. Lawley, A., & Cahn, R. W. *J. Phys. Chem. Sol.*, **20**, 204 (1961)
111. J. E. Epperson, J. E. Spruiell, *J. Phys. Chem. Sol.,* **30**, 1721 (1969)
112. H. Okamoto, P. A. Beck, *Met. Trans.*, **2**, 569 (1971)
113. K. Oki, M. Hasaka, T. Eguchi, *J. J. Appl. Phys.,* **12**, 1522 (1973)
114. S. M. Allen. J. W. Cahn, *Acta Met*. **23**, 1017 (1975)
115. A. Hernando, X. Amils, J. Nogués, S. Suriñach, M. D. Baró, M. R. Ibarra, *Phys. Rev. B*, **58**, 18 (1998)
116. X. Amils, J. Nogues, S. Suriñach, J. S. Muñoz, M. D. Barò, *J. Met. Nanocrys. Mater.*, **312**, 531 (1999)
117. E. Menèndez, J. Sort, M. O. Liedke, J. Fassbender, S. Suriñach, M. D. Baró, J. Nogués, *New J. Phys.*, **10**, 103030 (2008)

118. O. Kubaschewski, *Iron—binary phase diagrams*, Springer-Verlag Berlin Heidelberg, 5-9 (1982)
119. E. Menèndez, *PhD Thesis,* Universitat Autònoma de Barcelona, Spain (2008)
120. A. E. Clark, J. B. Restoff, M. W.-Fogle, D. Wu, T. A. Lograsso, *J. Appl Phys*., **103**, 07B310 (2008)
121. I. S. Golovin, H. Neuhäuser, A. Rivière, A. Strahl, *Intermet.,* **12**, 125 (2004)
122. R. J. Nelmes, R. O. Piltz, W. F Kuhs, Z Tun, R. Restori, *Ferroelectrics,* **108**, 165 (1990)
123. J. J. Fitzgerald, S. Prasad, J. Huang, J. S. Shore, *J. Am. Chem. Soc.*, **122**, 2556 (2000)
124. K. Babooram, H. Tailor, Z.-G. Ye, *Ceram. Internat*., **30,** 1411 (2004)
125. Z.-G. Ye, B. Noheda, M. Dong, D. Cox, G. Shirane, *Phys. Rev*., **64**, 184114 (2001)
126. S. Kamba, E. Buixaderas, J. Petzelt, J. Fousek, J. Nosek, P. Bridenbaugh, *J. Appl. Phys*., **93**, 2 (2003)
127. A. Safari, E. K. Akdogan, *Piezoelectric and Acoustic materials for transducer application*, chapter 4, pp 73, Springer (2008)
128. M. Ghasemifard, S. M. Hosseni, Gh. H. Khorrami, *Ceram. Int.,* **35**, 2899 (2009)
129. A. K. Sing, D. Pandey, *Phys. Rev. B,* **67**, 064102 (2003)
130. B. Noheda, D. E. Cox, G. Shirane, J. Gao, Z.-G. Ye, *Phys. Rev. B,* **66**, 054104 (2002)
131. Z-W. Yin, H-S. Luo, P-C. Wang, G-S. Xu, *Ferroelectrics*, **229**, 207 (1999)
132. X. Zhao, B. Fang, H. Cao, Y. Guo, H. Luo, *Mater. Sci. Eng. B*, **96**, 254 (2002)
133. S.-E. Eagle Park, W. Hackenbergerb, *Curr. Opin. Solid. S.T. M.*, **6,** 11 (2002)
134. J. Penga, H. Luob, T. Heb, H. Xub, D. Linb, *Mat. Let.*, **59**, 640 (2005)
135. Z-G. Ye, *MRS Bulletin,* **34**, 277 (2009)
136. L. E. Cross, S. J. Jang and R. E. Newnham, S. Nomura, K. Uchino, *Ferroelectr.* **23**, 187 (1980)
137. S. Nomura, K. Uchino, *Ferroelectr.* **41**, 117 (1982)

2

Experimental methods

2. Experimental methods

In this chapter, the experimental procedures that have been used to engineer the $Fe_{75}Al_{25}$/PMN-32PT heterostructures are described. Subsequently, the main experimental techniques used for the structural, morphological, electric, magnetic and magnetoelectric characterization are also described.

2.1. Sample preparation

2.1.1. Sputtering

The sputtering technique is used to grow thin films on given substrates by physical vapour deposition [1]. A gaseous plasma, usually Ar plasma, is used to extract material from the target -source materials- ejected in a form of neutral particles, either individual atoms, molecules, or clusters. When these neutral particles are extracted, they move in a straight line until they come into contact with other particles or a nearby surface. By placing the substrate in the path of these ejected particles, they deposit on its top and the substrate ends up coated with a thin film of the source materials [2].

The sputtering system consists of a chamber containing the targets' discs placed in chimneys at the bottom and the substrate to be covered at the top, as shown in a schematic representation in figure 2.1.

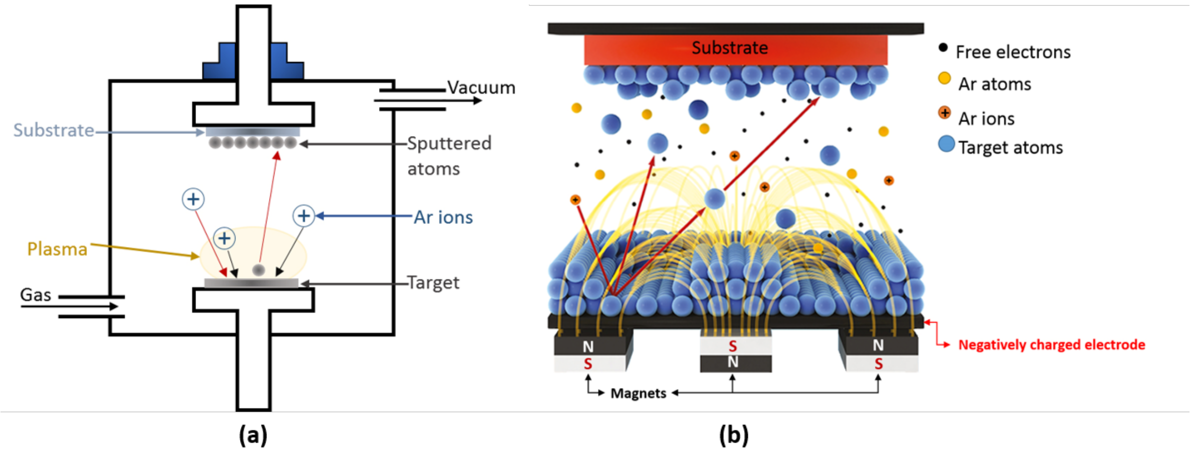
Vacuum
Substrate
Sputtered atoms
Ar ions
Plasma
Target
Gas
(a)
Substrate
Free electrons
Ar atoms
Ar ions
Target atoms
Negatively charged electrode
N
S
S
N
N
S
Magnets
(b)

Figure 2.1. Schematic drawing of a sputtering system. (a) Illustration of the magnetron sputtering process (b) modified from [3].

At first, a high vacuum, with a base pressure down to 10^{-7} Torr, is set in a chamber which is then slightly filled with Ar up to a pressure high enough to allow for plasma ignition (3×10^{-2} Torr). When the current source, connected to the target, is switched on, ever-present “free-electrons” are immediately accelerated and, at some point, some will approach the outer shell-electrons of neutral Ar atoms. Due to electron repulsion, the incoming ones will drive these shell-electrons off the gas atoms creating Ar^+ cations. At this point, the Ar^+ ions are accelerated towards the cathode, striking the target surface and realizing the material, and generating more electrons, by energy transfer (see figure 2.2).

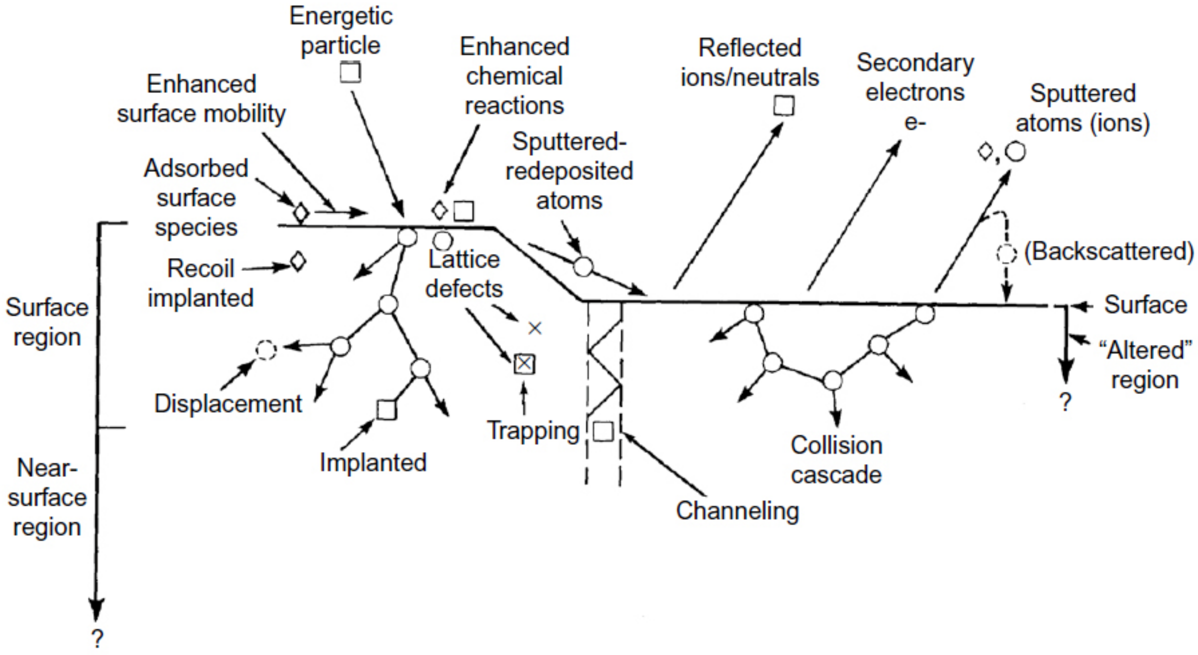
Energetic particle
Enhanced surface mobility
Enhanced chemical reactions
Reflected ions/neutrals
Secondary electrons e-
Sputtered atoms (ions)
Adsorbed surface species
Sputtered-redeposited atoms
(Backscattered)
Recoil implanted
Lattice defects
Surface
Surface region
"Altered" region
?
Displacement
Trapping
Implanted
Collision cascade
Channeling
Near-surface region
?

Figure 2.2. Representation of bombardment effects on a target surface [1].

While free electrons find their way back into the outer electron-shells of the ions, the additional free electrons feed the formation of Ar^+ and the continuation of the plasma, see figure 2.1(a). Due to the conservation of energy, when these electrons return to a ground state, the resulting neutral gas atom has gained energy that needs to be released in the form of a photon. This is the origin of the glowing, the colour of which depends on the chamber pressure. When the plasma is created, the targets’ chimneys can be opened to allow the deposition process.

A further step in this technique is the so-called magnetron sputtering [4], see figure 2.1 (b). While in simple sputtering (figure 2.1 a) only an electric field is applied, in magnetron sputtering an additional magnetic field is arranged behind the cathode plate.

Magnetrons take advantage of the fact that a magnetic field, configured parallel to the target surface, can restrict secondary electron movement near to it. The magnets are arranged in such a way that one pole is placed at the target's central axis, and a ring of magnets around the target's outer edge form the second pole. Trapping the electrons in this way greatly increases the probability an ionizing electron atom collision occurring. The increased efficiency of ionization of a magnetron contributes to dense plasma in the target area. This, in turn, leads to increased ion bombardment of the target, giving higher sputtering rates and, therefore, higher deposition rates at the substrate.

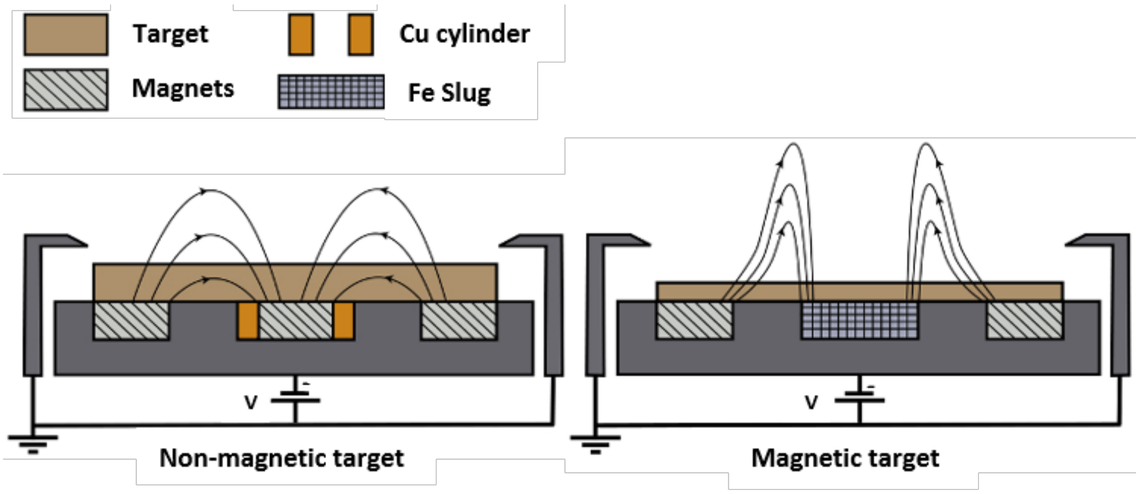

Figure 2.3. Magnetic field distribution when using a magnetic and a non-magnetic target [1].

In magnetron sputtering, both the direct current DC and the high-frequency alternating field RF may be used as power supplies to produce and maintain the plasma. In the DC case, the electrons are accelerated away from the negatively charged cathode; while in the RF operation mode, the electrons oscillate rather than following a linear trajectory.

Ferromagnetic materials (e.g., Fe, Ni, Co) have high magnetic permeabilities, which might trap the flux of the magnet set, and hence reduce the effectiveness of the magnetron sputtering set. To reduce this effect and allow the magnetic field to penetrate, the central magnet of the gun is replaced by an iron slug when working with ferromagnetic materials, see figure 2.3.

2.1.1.1. Sputtering ratio

The ratio of each sputtering process, and therefore part of the properties of the resulting alloy film, depends on three main factors: i) *the intensity of its plasma*, determined by the used target; ii) *the chamber pressure* during the process; iii) *the quantity* and *type of current* provided. Not determined by the rate but still of great importance is the substrate onto which the sputtered particles are to be deposited. These four concepts are briefly discussed in the following lines. Although it will not be tackled any deeper, it is important to notice that the amount of time the system is working will determine the thickness of the film.

i. **TARGET**: depending mainly on the metallic bond strength of each substance, the materials can be sputtered in a very wide range of times under the same conditions. This fact is expressed by the sputtering yield: *S*.

$$S = \frac{\text{ejected atoms or molecules}}{\text{incident ions}} \qquad \text{Eq. 2.1}$$

ii. **PRESSURE**: the driving force of the whole process is the plasma and its quality. Very low pressures lead to a reduction on the amount of Ar atoms available to be ionized, and, consequently, to a decrease of the deposition rate. At very low pressure, the plasma is not even sustained; however, under very high pressure, the sputtered atoms need to go through considerably more collision events before reaching the substrate, also reduces the deposition rate. At the same time, too many collisions also prevent ionization and yet, the plasma could be arched. Therefore, there exists a pressure range where the deposition rate is optimized, which slightly depends on the target-substrate configuration.

iii. **ENERGY SOURCE AND TRANSFERRED POWER**: the theoretical differences between DC and RF power sources have already been discussed and just a couple of technical consequences are still to be pointed out. The main advantage of RF is that it may also be used to sputter insulating materials, such as alumina Al_2O_3. In addition, by oscillating electrons, the sputtering rate is about twice as high that of the DC sputtering in the same chamber pressure. However, it needs twice as much power as the DC sources to achieve a similar deposition rate. These facts need to be regarded to when formulating the experiments.

iv. **SUBSTRATE:** its composition and the roughness of the surface onto which the material is deposited may have a great impact on the properties and characteristics of the resulting product.

2.1.1.2. Experimental details

50-nm thick $Fe_{75}Al_{25}$ (at. %) films was grown by co-sputtering at room temperature on [110]-oriented PMN-32PT single crystals using an AJA International, Inc. magnetron sputtering system. Depositions was carried out a rate of around 0.6 Å/s. The $Fe_{75}Al_{25}$ films were grown on 0.5-mm thick and 3 x 4 mm^2 rectangular-shaped [110]-oriented PMN-32PT substrates.

Regarding the patterned heterostructure, before the whole lithography process, a 10 nm thick Cu films were grown by sputtering at room temperature on 0.25 mm-thick and 1 x 1 cm^2 square-shaped [011]-oriented PMN-32PT using the AJA International, Inc. magnetron sputtering system, as a bottom contact. Deposition was carried out a rate of around 5 Å/s. Subsequently, before the photoresist removal process, 50-nm thick $Fe_{75}Al_{25}$ (at. %) motifs (e.g., dots, triangles, donuts, and squares) was grown by co-sputtering at room temperature on (10 nm thick Cu)/[011]-oriented PMN-32PT single crystals using an AJA International, Inc. magnetron sputtering system. Deposition was carried out a rate of around 0.6 Å/s.

2.1.2 UV Photolithography

UV photolithography has been used to fabricate FeAl patterned microstructures. As the name indicates, the crux of UV lithography centers around the properties and attributes of ultraviolet light. The overall concept of UV lithography is quite straightforward: UV light is shined through a mask onto a wafer covered with a photoresist. The photomask is the desired pattern that can be transferred onto a surface by means of UV light. The mask creates a sort of shadow between the light and the surface. Less light passes through sections blocked by the mask, as represented in figure 2.4. Masks can be created in several different ways, but one of the most common methods is the fabrication of a silicon shadow mask.

The overall process of UV lithography can be described with the following steps:

i. **SURFACE PREPARATION:** All surface contaminants (e. g. dust, lint, bacteria…) must be removed. This constitutes an important, and delicate part of the lithography process. To remove such particles, the surface is treated with several different chemicals. The surface is then primed with some different chemicals to aid the subsequent resist adhesion. Sample cleaning with…

ii. **RESIST COATING:** After the surface is cleaned and primed, the photoresist is applied by spin coating. The surface is spun rapidly while being coated with the photoresist. The photoresist bonds uniformly to the surface, with the excess flying off during spinning. A coating solvent is then used to dissolve the buildup along the edge of the surface.

iii. **PRE-BAKE:** This is a simple process of heating the surface in a conventional oven, or heated plate. The purpose of the pre-bake is to evaporate the excess coating solvent and to compact and harden the photoresist.

iv. **MASK ALIGNMENT:** The mask must be aligned correctly in reference to the surface. This procedure is accomplished either by hand using marks on the mask and the surface, or by using an automatic pattern recognition device. The most common ways to place the mask in reference to the surface are a) Contact, where the mask is in contact with the surface during the exposure; b) Proximity, where the mask is close to the surface but not in contact; c) Projection, where the mask is not close to the surface and the light passing through it is subject to imaging optics.

v. **EXPOSURE:** In this step, the entire system (photoresist, substrate and mask) is subjected to UV light by a UV source. The UV source consists of a lamp and filter, such as a Hg-lamp with an i-line notch filter that gives a typical wavelength of 365 nm.

vi. **DEVELOPMENT:** During the development stage, chemicals are applied to the surface causing either a negative- or positive- photoresist reaction. In the negative photoresist reaction, all molecules in the resist that are subjected to the most UV rays are bonded strongly together in long chains (polymerization). After the subsequent development process, the non-polymerized section of the resist decomposes and only the polymerized resist remains. In the positive resist case, a fraction of the resist is chemically altered to decompose when exposed to UV light; therefore, after the development, only the section not exposed to the UV light remains.

vii. **POST-BAKE:** This step is used to stabilize and harden the photoresist. It also removes any trace of development chemicals.

viii. **PHOTORESIST REMOVAL/PROCESSING:** At the end, to remove the excess photoresist, a simple solvent is used. If the photoresist is applied on top or at the bottom of the desired surface, two different ways to remove it can be used: a) **Etch-back**, where the photoresist is applied over the top the layer that is wanted to be patterned and the unwanted material is etched away; b) **Lift-off**, where a layer is deposited over the top of the photoresist. Then, when the resist is removed, the unwanted layer is also removed.

In figure 2.4, a schematic illustration of the lithography processes is shown.

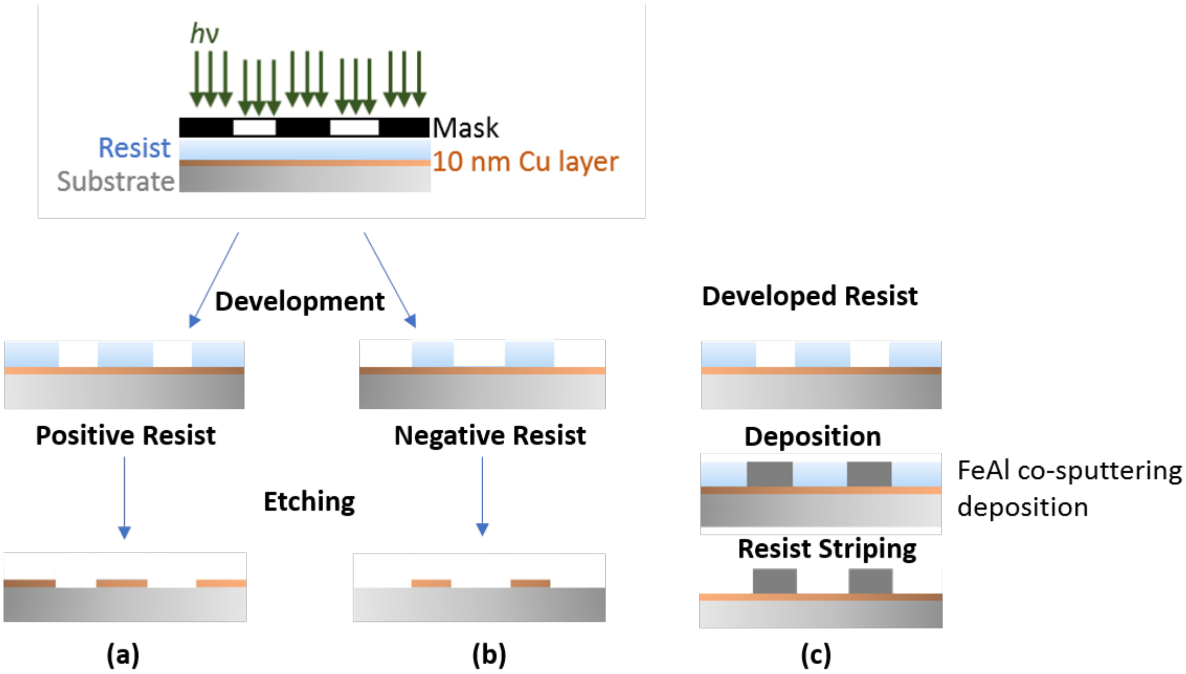
hv
Mask
Resist
Substrate
10 nm Cu layer
Development
Developed Resist
Positive Resist
Negative Resist
Etching
Deposition
FeAl co-sputtering deposition
Resist Striping
(a)
(b)
(c)

Figure 2.4. Illustration scheme of the basic lithography processes. Positive and negative resist with both etching processes is illustrated in panels (a) and (b). In our sample, the liftoff method (c) was used. Adapted from reference [5]. The Cu layer is deposited as the bottom electrode to have a homogeneous current distribution.

2.1.2.1 Experimental details

The photolithography steps were:

I. Dehydrating in a hot plate at 1000 °C for 10 minutes
II. Spin coating in AZ5214, reaching a final thickness of around 1.4 μm
III. Soft baking in a hot plate at 90 °C for 1.5 minutes
IV. Optical lithography with a UV lamp (λ= 365 nm): exposure time around 15 s
V. Post-exposure soft baking in a hot plate at 90 °C for 1 minute

Resist development in AZ 726 MIF (2.38 % TMAH- tetramethylammonium hydroxide- in H_2O with surfactants added for fast and homogeneous substrate wetting): 30 s in a developer, plus rinse in deionized H_2O.

After all, the resist liftoff is followed by:

I. Acetone immersion for 10 minutes
II. Rinse in isopropyl alcohol (IPA) for 10 minutes
III. Drying by blowing N_2

In contrast to what is typically done, the acetone immersion is carried out in a static condition (not in an ultrasonic bath) due to the fragility of the substrate and the possibility of film detachment.

2.2. Structural and morphological techniques

2.2.1. X-ray diffraction

X-ray diffraction (XRD) is a non-destructive analytical methodology which can provide information about the crystallographic structure of natural and manufactured materials. It was first developed in 1911 by von Laue, Friedrich and Knipping using rock salt [6]. One year later, W. L. Bragg confirmed that crystal diffraction is associated with a set of evenly spaced sheets typically running though centers of the atoms of the crystal lattice, see figure 2.5 [7]. To obtain a constructive interference in X-ray diffraction, the phase shift should be proportional to 2π or that the difference in the length of the path for rays reflected from successive planes should be equal to an integer number of wavelengths (fig 2.5).

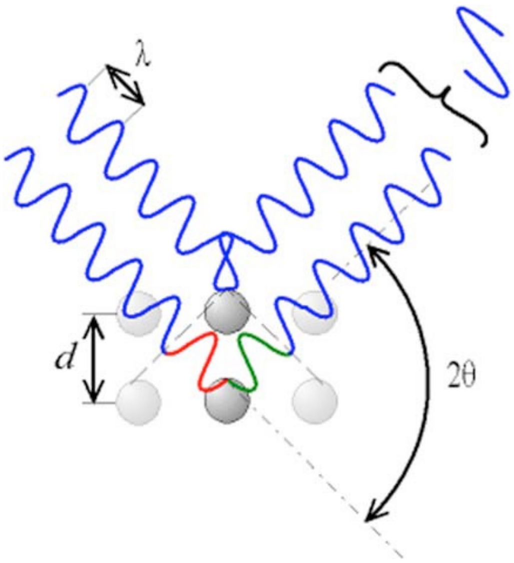

Figure 2.5. Schematic representation of Bragg diffraction [7].

Hence, a maximum diffracted intensity of the crystallographic planes corresponding to the interplanar distance *d* will appear in the diffraction pattern if, for a certain wavelength *λ* of the X-ray radiation and certain incident angle *θ*, the Bragg's law is obeyed, which is given by:

$$n\lambda = 2d\sin\theta \qquad \text{Eq 2.2 [7]}$$

where n is an integer representing the order of diffraction [9-11].

In the Bragg's law, it is assumed that the crystal is ideal -i.e., without structural defects- and the incident beam is perfectly monochromatic and collimated. These conditions are never fulfilled completely. Moreover, usually, materials are found to be composed of several grains, with different orientation and with a certain number of defects. Each of these grains is called a *crystallite* and, from an XRD viewpoint, it is the average of the coherently diffracting domain size. The size of these crystallites and the microstrains present in them can also be obtained from the XRD pattern since both effects contribute to the width of the diffraction peaks [12,13]. Usually, to evaluate this effect, it is considered that the peaks can be fitted using a pseudo-Voigt function, which is a linear combination of a Gaussian and Lorentzian -or Cauchy- profile [14,15]. With this formalism, the crystallite size (<D>) can be deduced from the Cauchy's contribution to the integral width of the diffraction peak, β_C, as follows:

$$< \mathrm{D} >= \mathrm{K}\frac{\lambda}{\beta_{\mathrm{C}}\cos\theta} \qquad \text{Eq 2.3}$$

with θ corresponds to the angular position of the peaks, λ the wavelength and K is a constant which depends on the crystallite shape [12], but generally is close to unity. As mentioned, the crystallite size, <D>, represents the average of the coherent diffraction domain. The above equation is commonly known as the Scherrer's formula [12]. Analogously, microstrains can be determined from the Gaussian's contribution to the integral peak width, β_G, using the expression:

$$\mathrm{microstrain} = < \mathrm{e} > = \frac{\beta_{\mathrm{G}}}{4\tan\theta} \qquad \text{Eq 2.4}$$

where <e> represents the upper limit of microstrains. However, it is more frequent to use the mean-square root of microstrain, $<\varepsilon^2>^{1/2}$ (rms strain), which is related to <e> as follows: $<e>=1.25<\varepsilon^2>^{1/2}$. [13].

When a sample, composed of several phases, is analyzed by XRD, each phase produces its own diffraction pattern. The relative intensity of the several peaks in the pattern depends on the relative concentration of the different phases. The phase identification can be carried out by comparison with Powder Diffraction Files databases such as PCPDFWIN, FindIt or the X'Pert HighScore program [16].

2.2.1.1 Modes of XRD

2.2.1.1.1. Bragg-Brentano

The sample, placed in the center of a flat goniometer, rotates with an angular velocity of θ/Δ*t*. The X-ray detector moves around the circumference of the goniometer with an angular velocity of 2θ/Δt and counts the number of photons per second. Since the detector has to follow the diffracted radiation, when the sample rotates θ, the detector has to rotate 2θ, since the diffracted beam has deviated 2θ with respect to the incident beam. Therefore, this Bragg-Brentano geometry is also known as “θ-2θ” scanning since the X-ray source and detector are coupled. After diffracting, and before entering the detector, the X-ray beam passes through a slit in order to keep the X-rays diffracted by the sample collimated. The width of this slit determines the maximum intensity in the detector. These different parts of the diffractometer are illustrated in Figure 2.6.

.

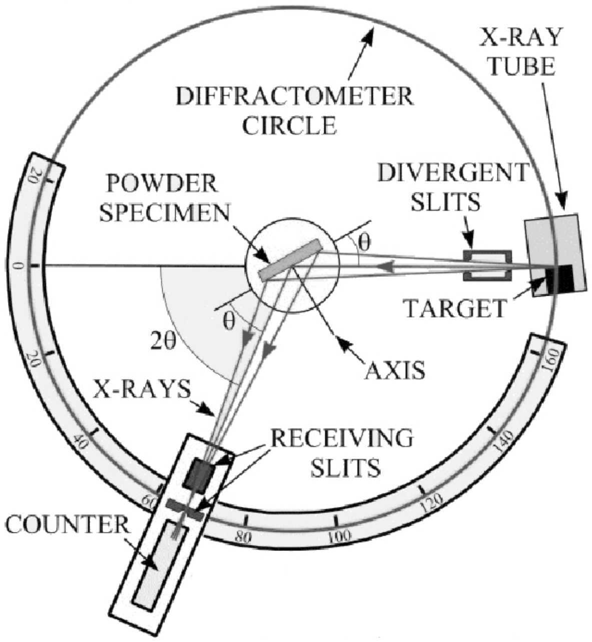

Figure 2.6: Schematic picture of an X-ray diffractometer in Bragg-Brentano configuration (Modified from Cullity-1956) [13].

Note that diffraction of a crystallographic plane (hkl) will only occur when this plane is parallel to the sample surface. Hence, the crystallographic texture (i.e., preferred orientation of the crystallites) will have a very strong influence on the intensities of the diffraction peaks in the resulting pattern

2.2.1.1.2. Grazing Incidence

XRD measurements of "thin" (1-1000 nm) films, using conventional θ/2θ scanning methods, generally produce a weak signal from the film and an intense signal from the substrate. One of the ways to avoid intense signal from the substrate, and get a stronger signal from the film itself, is to perform a 2θ scan with a fixed grazing angle of incidence. This is popularly known as grazing (or glancing) incidence X-ray diffraction (GIXRD). The fixed angle is generally chosen to be slightly above the critical angle for total reflection of the film material (e.g., 1°). Note that, in this case, the sample remains fixed (at a certain angle of the incoming radiation) and the 2θ scans are obtained by the movement of the detector. In contrast to θ/2θ measurements, atomic planes which are not parallel to the surface are probed. Regarding the X-ray generation and beam collimation, a similar scheme as in the Bragg-Brentano configuration is utilized [17].

2.2.1.2. Experimental details

The XRD patterns were recorded by means of a *Philips X'Pert* diffractometer with a PIXcel^{1D} detector in Bragg-Brentano geometry using Cu Kα radiation (note that both wavelengths $\lambda(K_{\alpha1})$ = 1.5406 Å and $\lambda(K_{\alpha2})$ = 1.5444 Å have been used in an intensity proportion of $I(K_{\alpha2})/I(K_{\alpha1})$ =0.5). The experiments have been carried out at the Servei de Difracció of the Universitat Autònoma de Barcelona.

Glancing incidence XRD (GIXRD), with an incidence angle of 1°, and reciprocal space maps around (001) and (1-10) reflection of the PMN-32PT using Cu Kα radiation, were performed using a Materials Research Diffractometer (MRD) from Malvern PANalytical company, equipped with a PIXcel1D detector from the Catalan Institute of Nanoscience and Nanotechnology. All diffraction patterns were recorded using a step-scan mode. This means that the sample and/or the detector rotate in steps instead of in a continuous way. The step size (between 32-65º and 66-100º) and the dwell time (≈500 s) at each step have been selected to have well-defined XRD peaks with a sufficient signal-to-noise ratio to properly fit the patterns.

2.2.2. Scanning electron microscopy (SEM)

In a scanning electron microscopy (SEM), when an electron beam arrives at the surface of a sample, some electrons can penetrate it. The depth of this penetration directly depends on the atomic number of the constituents of the specimen and the energy of the impinging electrons. The electrons lose their kinetic energy as they go deeper into the sample. In the zone of penetration, a certain number of interactions between the electrons of the beam and the atoms of the sample take place. And, therefore, in this zone, several kinds of signals are emitted (see figure 2.7).

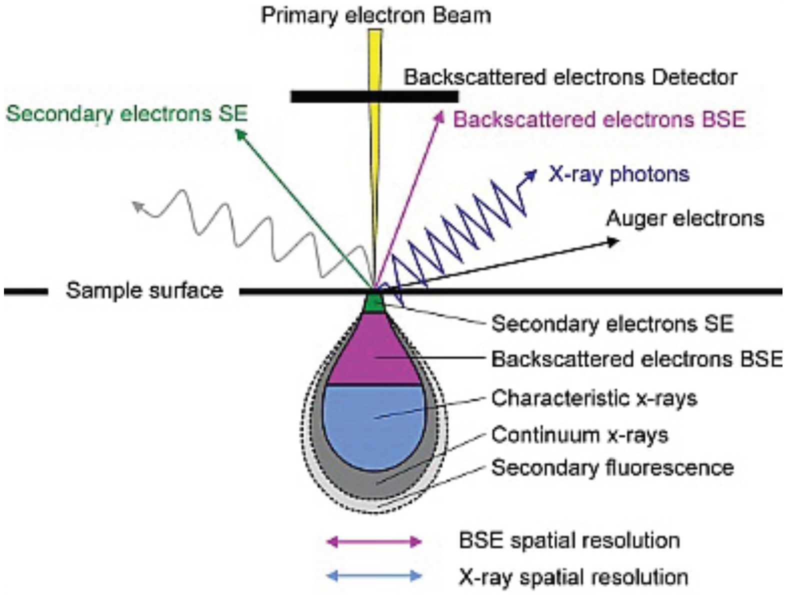
Primary electron Beam
Backscattered electrons Detector
Secondary electrons SE
Backscattered electrons BSE
X-ray photons
Auger electrons
Sample surface
Secondary electrons SE
Backscattered electrons BSE
Characteristic x-rays
Continuum x-rays
Secondary fluorescence
BSE spatial resolution
X-ray spatial resolution

Figure 2.7. Types of electrons and radiation generated after the interaction between the primary beam and the sample [18].

Auger Electrons: when an incident beam electron may eject a certain atom's electron, an electron vacancy is created. So, another electron from an external shell will fill the "hole", resulting in a certain amount of energy that can be passed to another electron. When this electron leaves the sample, it is called Auger electron. Such electrons usually have low energy values and only those generated at the very top surface (depth range of 0.5 to 2 nm) can escape thus providing information on this top surface. The power of this type of electrons, however, is characteristic of the atom that emits them. Therefore, these electrons provide specimen's compositional information and allow for the so-called Auger spectroscopy.

Secondary electrons: these electrons are the product of the impacts between high-energy electrons and the sample atoms. If the incident electron's energy is sufficiently large, the electrons in the sample may have sufficient energy to be expelled. These are so-called secondary electrons that have 0-50 eV energy range. The secondary electrons provide information on the sample density and the topography of the surface. All information from secondary electrons, however, is limited to a penetration depth of 10 nm.

Backscattered electrons: these electrons originate when the incident beam electrons hit the sample but cannot penetrate it and are, therefore, reflected back. Their energy, thus, depends heavily on the primary incident beam's energy. The information they give also depends on the atomic number of the elements, on the surface and, also, on its topography. For example, the image's brightness will depend on the specimen's atomic number as a large number of backscattered electrons will be produced for higher atomic numbers.

X-rays: Energy Dispersive X-ray analyses (EDX): when an incident electron enters a sample atom which induces the emission of another electron, the resulting "hole" is immediately filled by a third electron that was initially located in a more external electronic shell. Therefore, some energy is released in the X-ray frequency range. The resulting spectrum is therefore often used to make compositional analysis of the material. Typically, this method is denoted as "energy dispersive X-ray analysis" (EDX). If certain regions of the sample are scanned by choosing the part of X-ray spectra corresponding to one of the elements in the sample, the distribution of this element on the surface can be obtained. This technique is commonly known as *X-ray mapping*. The regions with higher densities of an element will appear brighter in the image, while the lack of the element will result in a dark area [**19-21**].

In a scanning electron microscope, the main components are filaments, system of electromagnetic lenses and diaphragms, sample chamber, scanning generator system and detector. When the filament (e.g., tungsten wire) is heated, it produces a beam of electrons in the range of 1 and 30 kV, which is intensified by applying a voltage between the cathode and the anode. Because electrons have a net charge, they can be deviated by applying magnetic fields and can, therefore, significantly reduce the beam size by using an *electromagnetic lens* device. In addition, with several metallic *diaphragms*, the beam can be further refined and homogenized. Furthermore, the electromagnetic lenses often help to speed up the electrons and thus affect the sharpness of the resulting image. In the *sample chamber*, one can find: the operator, with mechanical mechanisms to shift the sample along with the three spatial directions and several detectors for the different types of radiation emanating from the sample (x-rays, secondary electrons, backscattered electrons, etc.). There are two electromagnetic spirals, situated along the x - y directions between the electromagnetic lenses that generate oscillating magnetic fields to systematically scan the specimen. They enable precise monitoring of the frequency of the scan. Nowadays, the new SEMs apparatus use a field-emission guns. To remove the electron by tunneling effect a very high electric field is applied to the cathode. Some sources are covered by a low working function material such as zirconium oxide (which emits electrons by Schottky effect). The use of the FEGs greatly improves spatial resolution.

2.2.2.1. Experimental details

The morphology characterization of the 50 nm-thick $Fe_{75}Al_{25}$ (at. %)/[110]-oriented PMN-32PT thin film, and lithographed samples of 50 nm thick $Fe_{75}Al_{25}$ (at. %) motif/Cu/[011]-oriented PMN-32PT, were carried out by means of a JEOL JSM 6300 scanning electron microscope using secondary electrons in a FEI Magellan 400L microscope operated at 20 kV, at the Servei de Microscòpia of the Universitat Autònoma de Barcelona

2.2.3. Transmission electron microscopy (TEM)

In a conventional transmission electron microscope (TEM), a thin specimen is irradiated with an electron beam of uniform current density. If the penetration depth of the electron is larger than the thickness of the sample, the electrons can go through it. The transmitted electrons are then focused onto a fluorescence screen.

TEM exploits three different interactions of electron beam - specimen: i) *unscattered electrons*: the incident electrons are transmitted through the thin specimen without any interaction inside it. The beam of these electrons is called transmitted; the areas of the specimen that are thicker will have fewer transmitted unscattered electrons and will appear darker, while the thinner areas will have more transmitted and thus will appear lighter; ii) *elastically scattered electrons*: a fraction of the incident electrons are scattered -deflected from their original path- by atoms in the specimen in elastic fashion (without loss of energy). Elastically scattered electrons are the major source in TEM imaging and diffraction patterns; iii) *inelastically scattered electrons*: are the incident electrons that interact with specimen atoms in an inelastic fashion, losing energy during the interaction.

In scanning transmission electron microscopy (STEM) is possible use those signal that cannot be spatially correlated in TEM, namely, secondary electrons, scattered beam electrons, characteristic X-rays and electron energy loss. Like TEM, STEM requires very thin samples and looks primarily at beam electrons transmitted by the sample. The EELS (electron energy loss spectroscopy) signal, together with X-ray signal, constitute Analytical Electron Microscopy (AEM) [22].

In electron microscopy techniques, electrons are emitted from the electron gun and illuminate the specimen through a two or three-stage condenser lens system. The objective lens provides the formation of either the image or diffraction pattern of the specimen. The electron intensity distribution behind the specimen is magnified with a three or four-stage lens system and viewed on a fluorescent screen. The image can be recorded by direct exposure of a photographic emulsion or an image plate or digitally by a CCD camera. In Figure 2.8 a schematic diagram illustrating the main components of a TEM is presented.

The *electron gun* is the first and basic part of this microscope and is the source of electrons. It is usually a V-shaped filament made of LaB_6 or W (wolfram/ tungsten) that is wreathed with Wehnelt electrode (Wehnelt Cap) shaping the beam electrostatically, i.e., reducing the crossover of the diameter of the beam optimizing its brightness. The electrons are released from a small area of the filament (point source) due to the negative potential of the electrode. A point source is critical because it emits -with similar energy- monochromatic electrons. The conventional electron guns and field emission guns (FEG) are the two common types of electrons guns. A positive electrical potential is applied to the anode in traditional electron guns, and the filament -cathode- is heated before electrons are released. The electrons are accelerated by the positive potential down the column, and because of the negative potential of the cap, all electrons are repelled toward the optic axis. There is a set of electrons in the space between the filament tip and Cap. Those electrons at the bottom of the space charge -nearest to the anode- can exit the gun area through the small hole (< 1 mm) in the Wehnelt Cap and then move down the column to be later used in imaging. A field emission weapon is a strongly pointed tungsten tip placed at several kilovolts of negative potential compared to a nearby electrode, resulting in a very high potential gradient on the tungsten tip surface. The potential energy of an electron as a function of distance from the metal surface has a sharp peak -from the work function-and then it drops off quickly, due to electron charge travelling through the area under the action of the electric field.

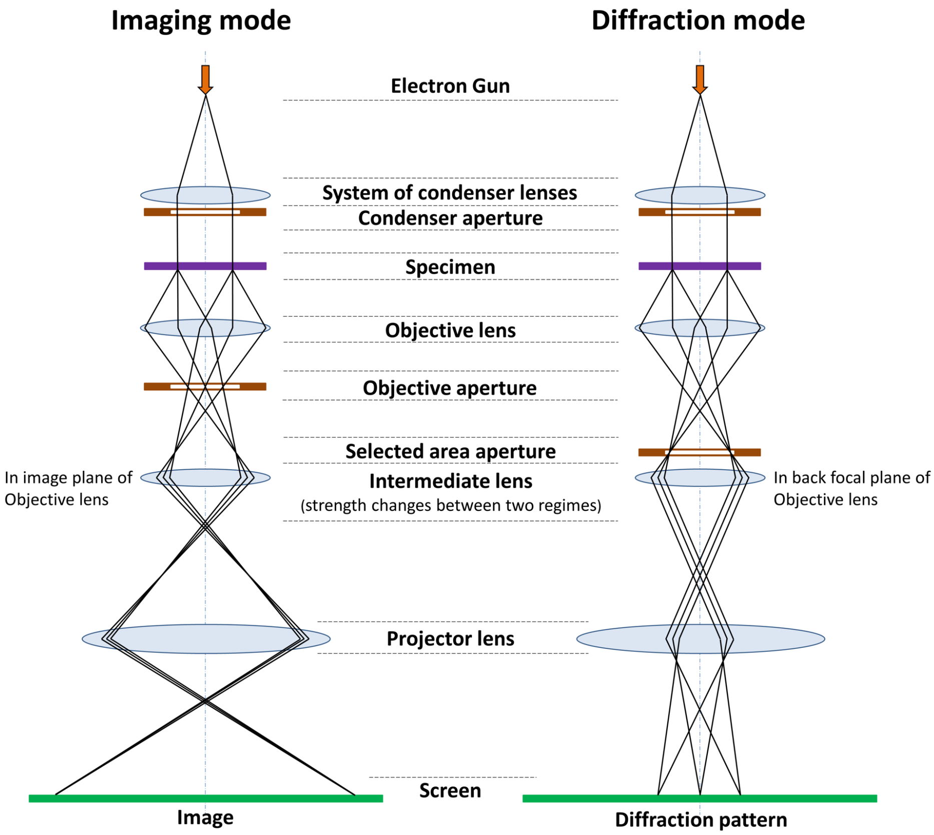
Imaging mode
Diffraction mode
Electron Gun
System of condenser lenses
Condenser aperture
Specimen
Objective lens
Objective aperture
Selected area aperture
Intermediate lens
(strength changes between two regimes)
In image plane of Objective lens
In back focal plane of Objective lens
Projector lens
Screen
Image
Diffraction pattern

Figure 2.8. Schematic diagram illustrating the main components of a TEM, imaging mode (left), diffraction mode (right). [23].

Since electrons are quantum particles and their locations have a distribution of probability, a certain number of electrons nominally on the metal surface will be at some distance from the surface so that they can reduce their energy by moving further away from the surface. This transport-via-delocalization is called *tunnelling* and is the basis for the field emission effect. FEGs (field emission guns) produce much higher source brightness than in conventional guns -electron current > 1000 times-, better monochromatically, but require a very good vacuum (≈10^{-7} Pa).

The *condenser system*: under the electron gun there are two or more condenser lens. Together, they de-magnify the beam emitted by the gun and control its diameter as it hits the specimen. An aperture is present between the condenser lens -the condenser aperture- which can be used to control the convergence angle. The condenser control can be thought of as control of brightness, but it actually allows a wide range of control over the sample area. The first condenser lens, often labelled spot size, sets the demagnification of the gun crossover. The second lens provides control of the convergence angle of the beam leaving the condenser assembly [24,25].

The *specimen chamber*: This chamber is situated below the condenser. The sample must be kept in the exact position within the objective lens but also it should be able to move several millimeters and be rotated by wide angles.

The *objective and intermediate lens*: the function of the objective lens is to form the first intermediate pattern of image and diffraction, which is expanded and projected on the viewing screen by subsequent projector lenses. It is based on the target's plane in the image mode. In the diffraction mode (see figure 2.8 right), on the other side, the intermediate lens is centered on the objective's back focal plane and the diffraction pattern is projected onto the viewing screen. An essential feature of the objective device is the opening holder, which enables one of three or four small apertures to be placed in the back focal plane column. The resolution is controlled by its diameter so that a large aperture is needed for higher resolution. The objective opening can also be used to control the image contrast.

The *projector system*: as mentioned above, the objective lens -with a magnification of 50-100 times- produces the first image. This is further improved by a combination of intermediate and projector lenses and is eventually projected onto the fluorescent camera. Some specialized microscopes have an energy filter below the specimen which can be tuned to allow the passage of only elastically scattered electrons. For example, this is of particular interest in high-resolution electron microscopy (HRTEM) as inelastic scattering degrades image quality or quantitative analysis of intensities of diffraction patterns [24,25].

Other components: there are different electromagnetic deflection coils in a TEM placed at strategic points. They are required to make minor adjustments to the alignment of the previously mechanically well-aligned electromagnetic lens. Further, coils permit small fields to be imposed to correct for the effect of astigmatism in the condenser, objective and projector system. Other important components are the detector for recording all different types of signals. Usually, photographs have been taken by an analogue camera in the past. Nowadays, CCD cameras are used in electron microscopy to capture images and diffraction. In addition, by combining the output from such a camera with a computer that has image processing software and microscope lens control, some alignment procedures can now be performed quickly and automatically [24].

2.2.3.1 *Imaging* and *diffraction* mode

Imaging mode: appropriately sized objective lens openings (figure 2.9) are placed in the back focal plane of the objective lens to operate in imaging mode. Diffracted beams can thus be deliberately excluded and only the central beam can pass through. The image that was created is called the bright field image; alternatively, by excluding all beams, a dark field image is formed, except for a specific diffracted beam of interest. The objective aperture, sitting below the specimen, is designed to improve the contrast of the images as it removes dispersed electrons which tend to minimize contrast. It is important to change the objective lens (focus knob) to create a clear image of the specimen [26].

Diffraction mode: the fixation points drop below the specimen to the focal plane when conducting diffraction imaging. So, the cross-over of the beam must occur in the back focal plane for diffraction imaging. When this happens, the focus will be on objective aperture, if left in place. Often, in diffraction mode, it is necessary to isolate a local region so that only this region produces a diffraction pattern. This is achieved by introducing an aperture into the column. When the selected area diffraction aperture is used to limit the area, which is used for obtaining a diffraction pattern, this is called selected area diffraction (SAD) see figure 2.10 [26].

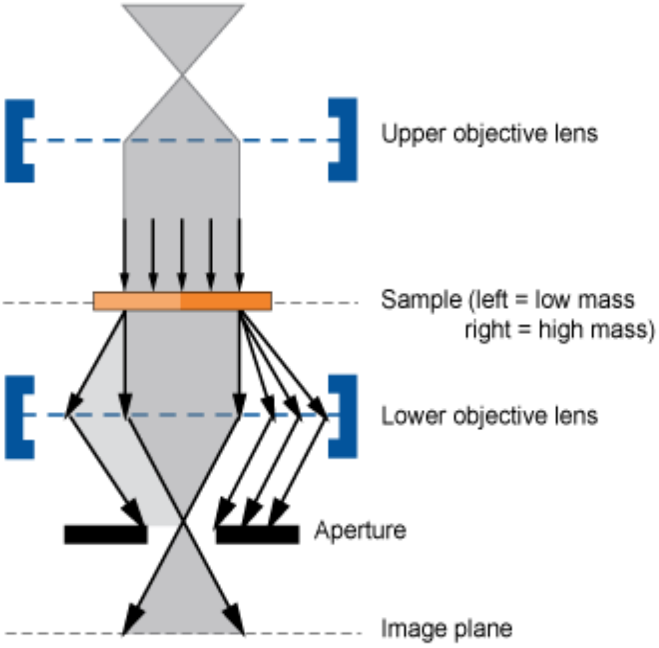

Figure 2.9. Schematic diagram illustrating the TEM settings [26].

However, there are two dark-field imaging modes: i) *DF1*: where an objective aperture is introduced and moved so that excludes the unscattered beam but allows some signal to pass through from a specific area of interest in the diffraction pattern, for example, a specific intensity spot; ii) *DF2*: where the beam is tilted so that the unscattered beam path is blocked by the objective aperture. In this way, a particular intensity spot in a diffraction pattern can be centered as the new “main beam”. The dark field image will be produced only from those electrons being diffracted along this axis. The image is then focused on the sample plane [26].

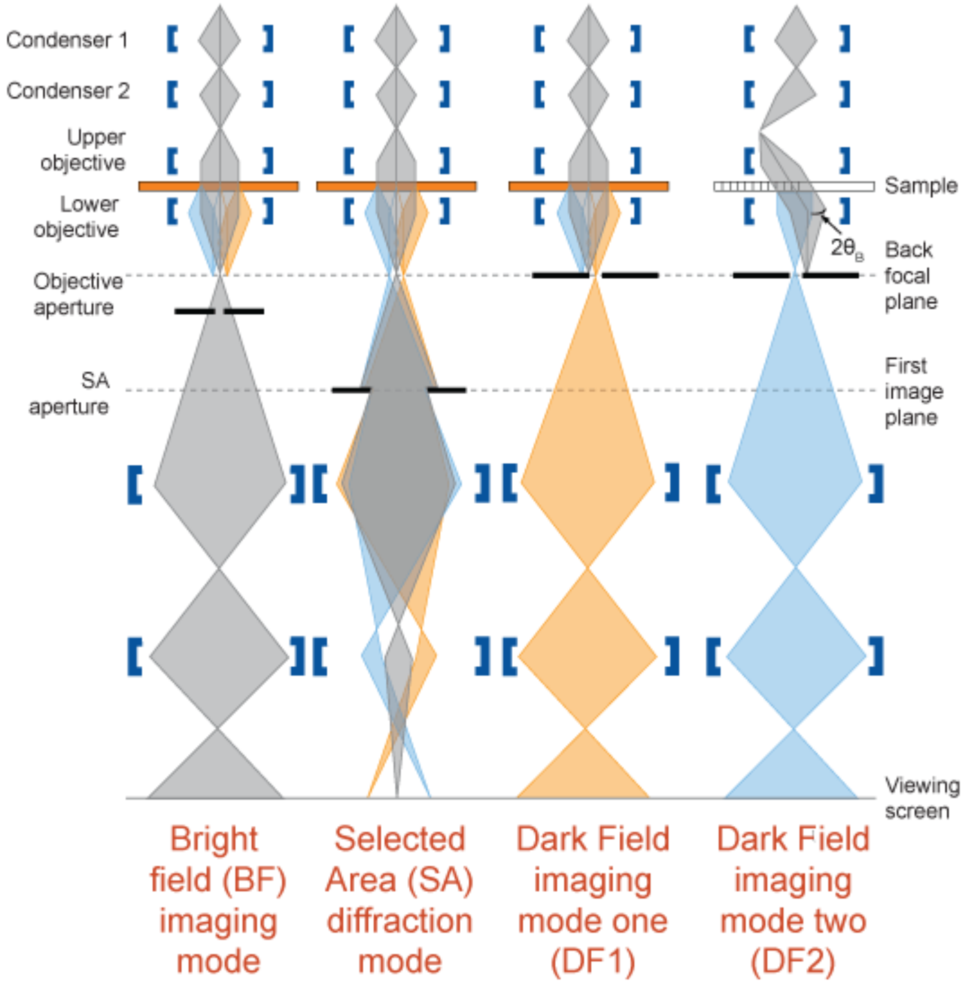
Condenser 1
Condenser 2
Upper objective
Lower objective
Objective aperture
SA aperture
Sample
2θ_B
Back focal plane
First image plane
Viewing screen
Bright field (BF) imaging mode
Selected Area (SA) diffraction mode
Dark Field imaging mode one (DF1)
Dark Field imaging mode two (DF2)

Figure 2.10. The beam paths for the different imaging modes [26].

2.2.3.2 STEM

In a STEM mode (scanning transmission electron microscopy), the electron beam is focused at one point in the sample, which is scanned by the shift coils. Some detectors collected the signal, and each of them is specific to detecting a particular type of signal. Depending on the analysis type, it can have the bright field detector, or the dark field signal detector using the ADF, annular dark field, and HAADF, high angle annular dark field. Both techniques have a specific detector, the only difference is the angle at which the electrons are detected. There is a direct proportionality between atomic number, Z, and the angle at which electrons are detected (greater angle means greater sensibility to Z number), the HAADF is in fact a powerful technique for investigating the different phases present in a sample.

2.2.3.3 Experimental details

To investigate the inner parts of the as-grown samples, cross-section lamellae were prepared by focused ion beam and placed onto a Cu TEM grid. To characterize the cross-section from structural and compositional viewpoints, TEM, energy dispersive X-ray (EDX) analysis, and high-angle annular dark-field scanning transmission electron microscopy (HAADF STEM) were performed using a TECNAI F20 HRTEM/STEM microscope operated at 200 kV.

2.2.4. Atomic force microscopy

The atomic force microscopy (AFM) basic operational theory is based on the accurate identification of interaction forces acting between a sharp probe tip and a sample surface at close distances. For example, in contact mode (described later), the probe tip is moved over the sample surface to perform imaging while the contact force, F, is kept constant through feedback loops. The interaction force F or the associated physical quantity can be calculated in order to perform spectroscopy as a function of specific experimental parameters such as tip-sample distance *d* and bias voltage *V*.

The most important components of an AFM device, adapted from [27], are shown in figure 2.11.

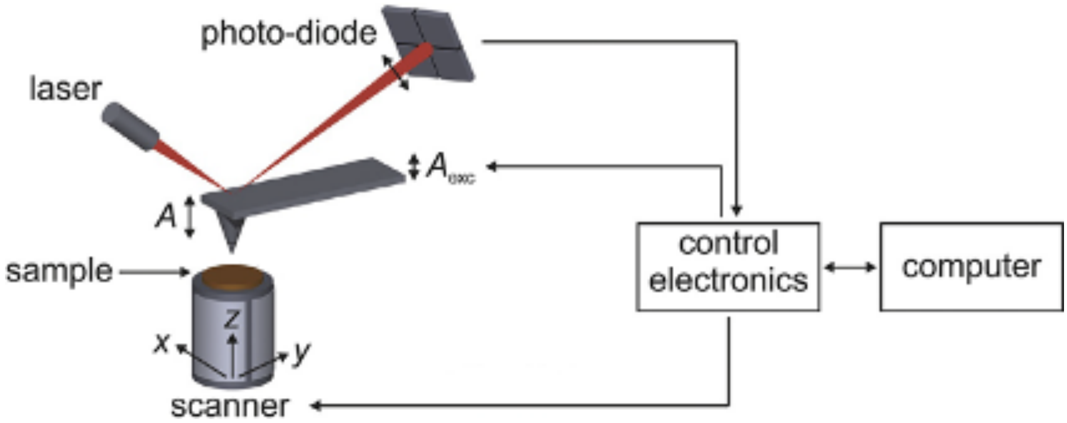

Figure 2.11. Schematic drawing of typical AFM configuration. A laser deflection device that tracks the movement of the reflected beam on a position-sensitive photodiode is shown. For dynamic AFM operation, the cantilever base is excited with an amplitude A_{exc}, resulting in an oscillation of the probe tip with amplitude *A* [27, 28].

The main AFM components (Fig. 2.11) can be described as: *i)* A *scanner*, to position the sample with picometer-scale accuracy in three dimensions (x, y, z) with respect to the probe tip; *ii)* A *force sensing element* and the detection scheme associated with it; *iii)* *Control electronics and a computer* for (a) control scanners and other components; (b) recording, displaying and saving data and (c) operating feedback loops.

Scanners commonly used in AFM configurations are made of piezoelectric materials in different geometries that elongate/contract with applied voltage. While using flexure stages employing piezoelectric elements usually allows positioning in the lateral x, y directions, a single piezoelectric tube-shaped scanner -with five isolated electrodes- enables tip-sample positioning in the lateral x, y as well as vertical z directions. All scanners, made of piezoelectric elements, are subject to non-linearities, including hysteresis and creep, which are somewhat alleviated using software and/or hardware-based correction schemes. In an AFM, the force-sensing element typically consists of a micro-fabricated cantilever (Si, SiO_2, or Si_3N_4, with a length of several hundred micrometers) with an integrated, sharp tip. In response to the force interaction F between the tip and the sample, the cantilever functions as a spring (spring constants k varying from ~ 0.01 to ~ 100 Nm^{-1}). The force sensor deflections are observed through three primary approaches: *i)* with a laser beam, the force sensor is deflected and deposited on a photodiode; *ii)* using an interferometer brought into proximity of the force sensor; *iii)* electrically, using a piezoresistive cantilever or a piezoelectric tuning fork.

The commonly three distinct operating modes in an AFM are shown in figure 2.12 and, subsequently, each mode is briefly described.

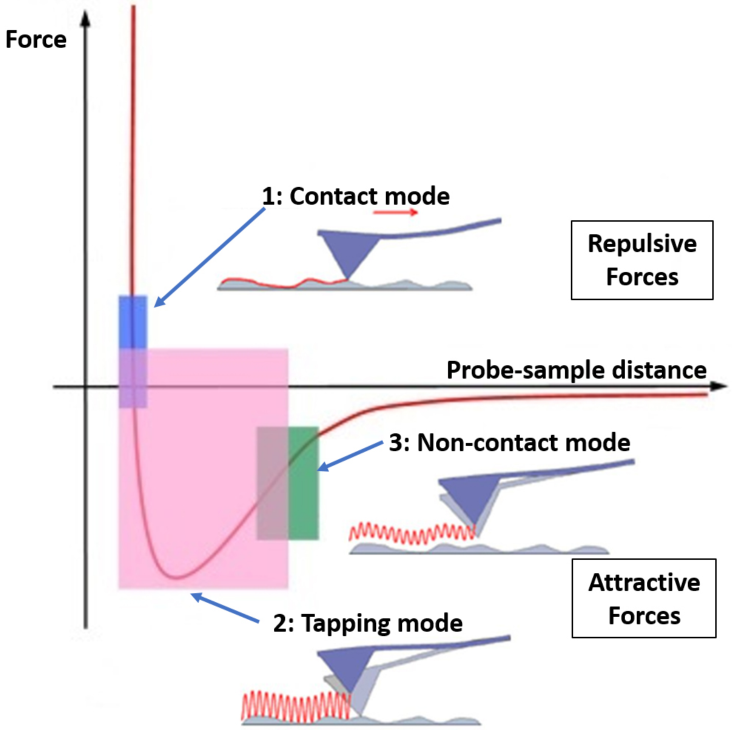

Figure 2.12. The three-operating mode in a modern AFM: 1) *contact mode*: blue area, 2) *tapping mode*: pink area; 3) *non-contact mode*: green area, modified from [29, 30].

Depending on the type of sample and on the nature of tip-surface interaction, three operating modes can be used [28]:

i. **Contact mode**: this is the simplest and the most common way to operate. At the end of a cantilever (<1 Nm^{-1}, usually) a probe tip is located. The tip is first brought into proximity of the sample surface, with the tip eventually "snapping" in contact with the surface at the moment when the gradient of the tip-sample interaction overcomes the low spring constant of the force sensor. The repulsive interaction force acting between the tip and the sample is then tracked by detecting the related force sensor deflection and is held constant at a fixed value-usually in the order of a few nano-Newton- through a feedback loop as the tip is raster-scanned across the surface. The acquisition of topographical maps, with nanometer-scale resolution, is done by tracking and recording the vertical position of the force sensor base with respect to the surface leads. In addition, recording the twisting of the cantilever during scanning due to the torque, caused by the lateral forces acting on the tip apex allows for quantitative friction measurements, with the possibility of studying its dependence on different physical parameters for the nanometer-scale contact geometry performed by the tip apex and the sample surface. Despite their operational simplicity, AFM contact mode experiments have certain disadvantages: an intrinsically low signal-to-noise ratio compared to "dynamic" modes that track modulated signals; the lateral forces and repulsive interactions can damage the tip apex and the sample surface during scanning.

ii. **Tapping mode**: with this mode one introduces a "dynamic" operation, which involves the force sensor deliberately excited at or near its resonance frequency f_0 with excitation amplitude A_{exc}. As the tip is brought near the sample surface, the characteristic of the surface causes the oscillation frequency, amplitude and phase to change in response to the strength of the tip-sample interaction. The force sensor is operated at a fixed frequency, in this mode, and changes in its amplitude A (usually in the order of several to tens of nm) and phase φ are monitored as a function of the tip-sample position. The topographical maps, with nanometer resolution, is given by the variation in amplitude ΔA, and thus the interaction of the tip-sample force, that keeps constant during raster scanning, without the adverse effect of permanent repulsive contact and lateral forces that causing tip and sample damage. Therefore, image tapping mode is often used to characterize soft biological materials, as well as other samples, mostly in air or liquids. As shown in figure 2.12 (pink area), the relatively large amplitudes, used during the measurements, cause the tip to cover both attractive and repulsive parts of the tip-sample interaction. This causes the apex to "tap" the surface periodically during operation or, in other words, to form intermittent tip-sample contact. The resulting data includes information on the sample surface's nanomechanical properties. Because of its reliance on changes in amplitude as a feedback parameter, AFM tapping mode is referred to as AFM (AM-AFM) “amplitude modulation”.

iii. **Non-contact mode**: A fundamental “weakness” of both AFM contact and tapping mode includes the creation of a finite contact area during operation between the tip apex and the sample surface. During the experiment, the tip, that is atomically sharp at the beginning, becomes blunt, resulting, in most cases, in the inability to achieve atomic resolution by AFM contact and tapping mode. The dynamic operating mode of "non-contact" AFM (NC-AFM) was implemented to achieve atomic resolution imaging. For NC-AFM, the resonance frequency f_0 is initially oscillated and brought close to the sample surface. Unlike tapping mode, the amplitude of oscillation is kept constant at low values (ranging from ~1 Å to a few nanometers) so that the interaction can be limited to the attractive regime, therefore, the tip maintains its atomically resolved shape during the experiment. In recent years, it has been demonstrated that this mode can give impressive results at the atomic-scale characterization of insulating metal oxide surface, the visualization of the adsorbent intramolecular structure and the discrimination in the order of chemical bonds.

2.2.4.1 Experimental details

An atomic force microscope (AFM) MFP-3D was used to characterize the local characteristics of the samples, patterned ones, (Asylum Research, an Oxford Instruments company, USA). The tips utilized were $PtIr_5$ coated conductive tips from the Nanosensor model EFM (PPP-EFM), with the force constant of 2.8 N/m. All samples were examined in a sealed chamber under ambient laboratory, at the Institut Català de Nanociència i Nanotecnologia.

2.3 Magnetic characterization techniques

2.3.1 Vibrating sample magnetometry (VSM)

In the presence of a static and uniform magnetic field H, the principle of a vibrating sample magnetometer (VSM) is to determine the electromotive force produced by a ferromagnetic sample while it vibrates sinusoidally, typically by the piezoelectric material. In Faraday's law, the induced electromotive force in a spiral, V_{fem}, is proportional to the temporal variation of the magnetic flux, ϕ, which passes through it.

$$\mathrm{V_{fem}} = -\frac{\mathrm{d\phi}}{\mathrm{dt}} \qquad \mathrm{Eq.\,2.5}$$

where Φ is the magnetic flux and t is the time [31,32].

Linear attenuator-based components are used in VSMs which were originally obtained by changing audio speakers. This approach was dropped due to the interference created by the in-phase magnetic noise, as the magnetic flux varies sinusoidally through a nearby pickup coil. Assuming a solenoid to be consisting of N turns for a constant cross-section, A, the magnetic induction inside the coil, B, can be expressed as follows:

$$\mathrm{B} = \frac{\phi}{\mathrm{NA}} \qquad \mathrm{Eq.\,2.6}$$

Therefore,

$$\mathrm{V_{fem}} = -\mathrm{NA}\,\frac{\mathrm{dB}}{\mathrm{dt}} \qquad \mathrm{Eq.\,2.7}$$

As the sample is vibrating, it is possible to express the magnetic moment while $m(t) = m_0 \cdot \sin(ft)$, where m_0 is the moment amplitude and f is the frequency. As $B = \mu_0(H + M)$, $M = m/V$ (B is the magnetic induction, M the magnetization, V the sample volume, μ_0 the free space permeability and H the magnetic field), dB/dt can be obtained as follows:

$$\frac{\mathrm{dB}}{\mathrm{dt}} = \left(\frac{\mu_0 \mathrm{m_0 f}}{\mathrm{V}}\right)\cos(\mathrm{ft}) \qquad \mathrm{Eq.\,2.8}$$

Thus, the amplitude of the induced voltage is proportional to the amplitude of the sample's magnetic moment:

$$V_{fem} \propto f m_0 G(z) \quad \text{Eq. 2.9}$$

where G(z) is a function that determines V_{fem}'s dependency on the sample position in the holder relative to the coils and, therefore, depends on the configuration of the coils.

The VSM basically calculates the difference in magnetic induction between one region of space with the sample and another without the sample, thus allowing calculation of the magnetic moment, m, and obtaining the hysteresis loops of the material when different magnetic fields are applied. A schematic diagram of different component of VSM is shown in figure 2.13.

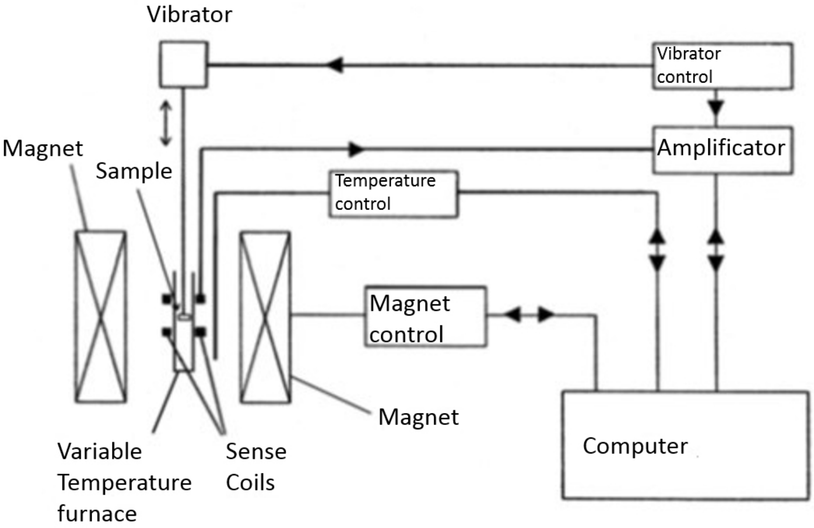

Figure 2.13. Schematic diagram of the different components of the VSM.

For the VSM measurements, a *Micro-Sense (LOT-Quantum Design)* VSM, located at the *Gnm³* group, with a maximum applied magnetic field of 2T generated by an electromagnet, was used. For more details about the measure conditions, sample positioning and applied electric field, see the 2.5 section: *Magnetoelectric characterization*.

2.3.2. Magneto-optical Kerr effect (MOKE)

The magneto-optical Kerr effect (MOKE) originates from a net rotation and elliptical polarization of linearly polarized incident light when it is reflected at the surface of a magnetized sample [33]. The change in the polarization state of an incident electromagnetic wave (e.g., laser) occurs because of the interaction between the laser's electrical and magnetic fields and the spin of the electrons in the material. The magnitude of this change in polarization is proportional to the magnetization of the sample. Linearly polarized light can be depicted as a combination of equal amounts of right and left circularly polarized light. Right and left circularly polarized light effectively have different indices of refraction in magnetized media as they are absorbed and emitted differentially depending on the direction and strength of the magnetization of the sample [34]. The reflected light is then the sum of unequal proportions of right and left circularly polarized light; that is, the reflected light is now elliptically polarized with its axis of polarization rotated by an amount θ_k, called the 'Kerr angle'. For homogeneous ferromagnetic materials, the magneto-optical effects can be considered to be linear with magnetization [35]. Therefore, by measuring the rotation or ellipticity changes as a function of the field one can probe the magnetic hysteresis curve. When used on materials with a large absorption coefficient the technique is very surface sensitive. The Kerr signal stems only from about twice the penetration depth of the employed light, which is typically about 15-30 nm for metals in the visible wavelength range. This makes the technique very surface sensitive. In reflection mode, MOKE measurements can be performed in three different optical and magnetic geometries [36], depending on the relative orientation of the magnetization M with respect to the light incidence plane: polar, longitudinal, and transverse Kerr effect. These three geometries are depicted in figure 2.14.

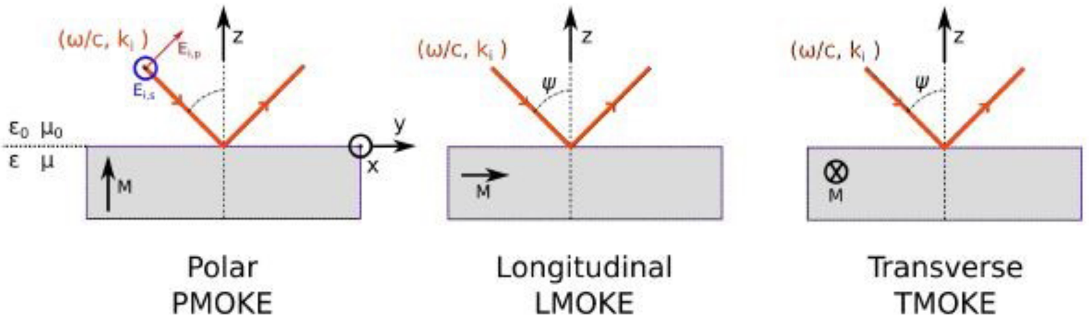

Figure 2.14. Three geometries of MOKE [37].

Since the MOKE technique seldom yields an absolute value for the sample magnetization, the corresponding hysteresis loops are typically normalized to unity at saturation or given in arbitrary units. The apparatus is combined with two optical systems, one for MOKE measurements and the other for sample imaging. A plane polarized (i.e., linearly polarized) laser beam is extended and then centered on the sample surface to a diffraction-limited spot. Then the reflected cone is collimated and analyzed for its polarization. In addition to this magneto-optical ray path, the halogen lamp, focusing lens, collimating and the charging-coupled device (CCD) camera form a traditional optical microscope, figure 2.15 [38,39]. The sample surface can then be seen through the optical microscope, while the laser spot is passed over the surface until it is centered on top of the working zone.

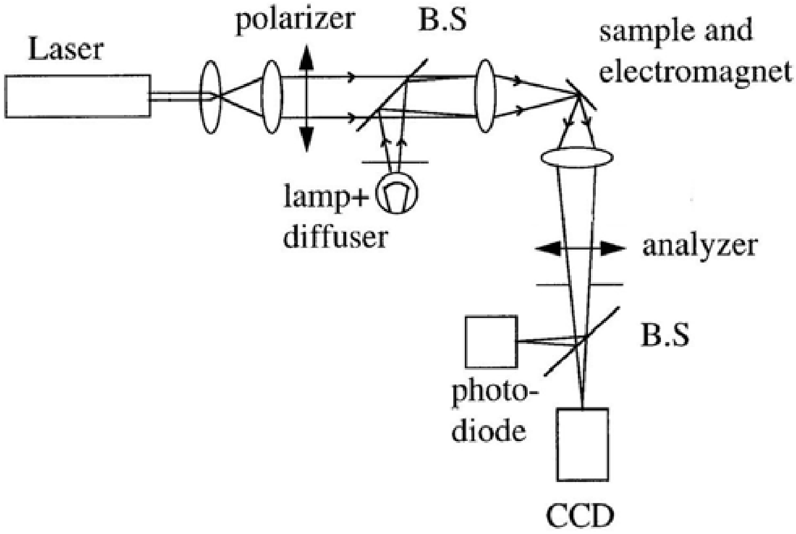
Laser
polarizer
B.S
sample and electromagnet
lamp+ diffuser
analyzer
B.S
photo-diode
CCD

Figure 2.15. A schematic illustration of a MOKE setup, where *B.S.* is a beam splitter [38,39].

For the MOKE measurements, *Durham Magneto-Optics* apparatus at the Institut Català de - Nanociència i Nanotecnologia was used. The minimum size of the red laser spot, with $\lambda \sim 650\ \mathrm{nm}$, is around $3\mu\mathrm{m}$. For more details about the measure condition (i.e., longitudinal, transversal, and polar configuration), sample positioning and applied electric field used, see the 2.5 section: *Magnetoelectric characterization*.

2.3.3. Magnetic force microscopy

Magnetic force microscopy (MFM) is a secondary image mode derived from the intermittent contact mode (Tapping Mode) of an AFM that maps magnetic force gradients above the sample surface. This is achieved by a two-pass method (figure 2.16), commonly known as the patented LiftMode (or “nap”) name [40,41]. This mode separately measures topography and magnetic force gradients by using the topographical information obtained during the first pass to track the probe tip at a constant height above the sample surface during the second pass.

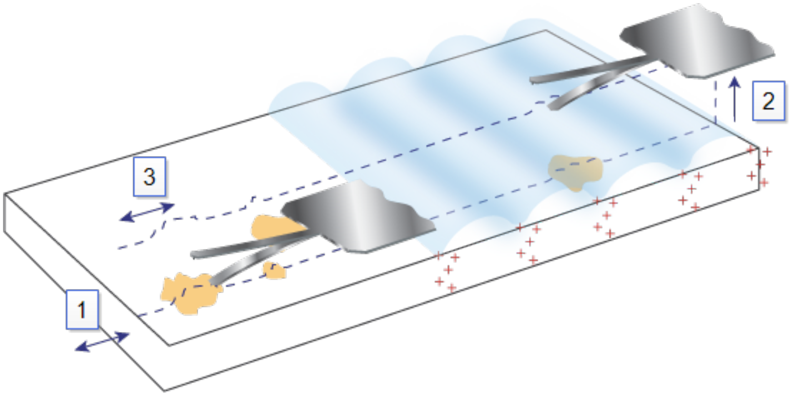

Figure 2.16. LiftMode: 1: first trace/retrace, the cantilever tracks a surface topography; 2: the cantilever ascends to Lift scan height; 3: the last trace/retrace, a cantilever profiles topography while responding to magnetic influences [41].

The MFM probe tip is coated with a ferromagnetic thin film. While scanning, it is the magnetic field’s dependence on tip-sample separation that induces changes in the phase, which constitutes the feedback signal [25].

2.3.3.1. Experimental details

For this characterization the tip used was a Nanosensor PPP-LC-MFMR (Point Probe Plus Magnetic Force Microscopy- Low Coercivity- Reflex Coating) with coercivity of approximately 7.5 Oe and remanence magnetization around 225 emu/cm^3.

2.4 Electric characterization

2.4.1 Ferroelectric hysteresis measurements (Polarization-Field loops)

Some materials with spontaneous polarization exhibit ferroelectricity and is reversible through the application of an electric field. The term “ferroelectricity” is analogous to ferromagnetism, namely a material possesses a permanent magnetic moment, notwithstanding most ferroelectric materials do not contain iron. Ferroelectric material can be defined that has a nonlinear relationship with polarization, P, and applied electric field, E. This relationship is provided by a hysteresis loop (as shown in chapter 1), which can be observed experimentally using the Sawyer – Tower circuit method [42,43]. Nowadays, the measurements of the I-V characteristic are used. These provide an abrupt current peak where the ferroelectric switching -between P^+ and P^- in the coercive field- occurs and enables the extrinsic ferroelectric effects to be easily disclosed. The charge is then obtained by integrating the current over time. If a parallel-plate capacitor, with known geometry (area, A, and thickness, t) is used, it is possible to obtain the polarization and electric field, following these equations:

$$\mathrm{P} = \frac{\int \mathrm{I}\,(\mathrm{t})\mathrm{dt}}{\mathrm{A}} \qquad \text{Eq. 2.10}$$

And:

$$\mathrm{E} = \frac{\mathrm{V}}{\mathrm{t}} \qquad \text{Eq. 2.11}$$

We should emphasize that the measured charge value obtained by integrating the current through the circuit in an ideal ferroelectric does not correspond to the material's polarization, but to the electrical displacement (D). For these materials, the electric displacement field is defined as:

$$\mathrm{D} \equiv \varepsilon_0 \chi \mathrm{E} \qquad \text{Eq. 2.12}$$

Where χ is the electric susceptibility.

So, to obtain P from these measurements, the $\varepsilon_0 E$ should be subtracted from the equation. For the ferroelectrics though, a high χ is expected, therefore, $\varepsilon = \varepsilon_0 (1+ \chi) \approx \varepsilon_0 \chi$, and consequently $\varepsilon_r = \chi$, implying $P \approx D$. In literature, this simplification is commonly used to make the description and comparison of the data easier.

2.4.1.1. Experimental details

The ferroelectric polarization versus applied voltage (i.e., electric field) loop was collected by grounding one of the electrodes (silver paste) while biasing the other (Fe-Al+silver paste) using the static hysteresis standard mode of the TFAnalyser2000 (Aixacct) with an integration time of 1 ms and a relaxation time of 1 s. With this protocol, the displacive current flowing through the circuit (I) was measured and the polarization was obtained from the integrated current in time and normalized by the area (A): $P = \frac{1}{A}\int Idt + C$. The constant C is selected to obtain a loop where the polarization values at maximum negative and positive applied voltage are equal. The convention used for the sign is the standard one; namely, the positive applied voltage corresponds to applying, to the PMN-PT, electric field pointing toward the grounded electrode.

2.4.2 Piezoresponse force microscopy

The piezoresponse force microscopy (PFM) technique is based on the strong coupling between polarization and mechanical displacement, for probing piezo-and ferroelectric properties at the nanoscale. This technique was first demonstrated in 1992 by Gűthner and Dransfeld using a ferroelectric polymer film [44]. The coupling can be achieved by applying a strongly positioned electrical field to the material and measuring, with picometer accuracy, the resulting surface displacements.

The tip used is a conductive, often metal-coated, AFM tip, that is brought into contact with the sample surface, functioning as a sharp top electrode. The other sample’s side is connected to a grounded bottom electrode. The tip voltage follows this equation:

$$V_{tip} = V_{dc} + V_{ac} \cdot \cos(\omega t) \qquad \text{Eq. 2.13}$$

where ω is the chosen modulation frequency and V_{dc} is an optional dc offset (figure 2.17). If the sample is piezoelectric the sample surface deforms mechanically in response to the voltage applied, owing to the converse piezoelectric effect [45]. The surface displacement is detected via the cantilever movement monitored by AFM optical beam deflection, assuming the tip displacement is equal to the surface displacement.

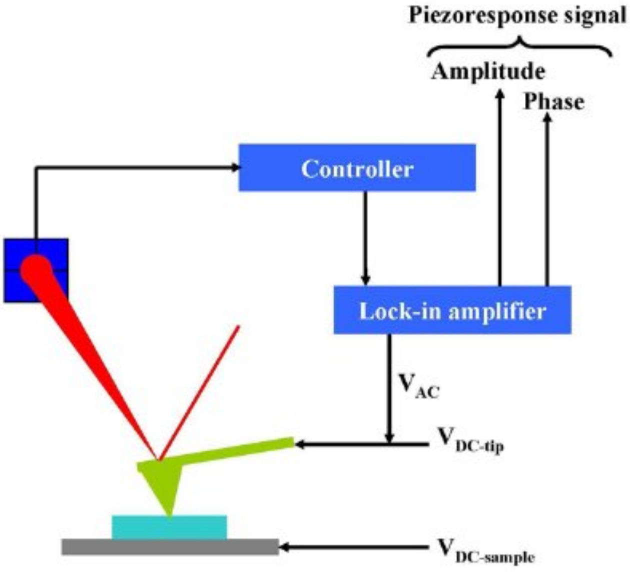

Figure 2.17. A schematic PFMs arrangement. When both ac and dc voltages are applied, to the metallized tip, the mechanical displacement is measured via conventional AFM method [46].

The piezoresponse is formally defined as the first harmonic component of tip oscillation:

$$A \cdot \cos(\omega t + \varphi) \qquad \text{Def. 2.1}$$

where A is the amplitude oscillation, given in length units, and φ is the phase difference between the excitation signal and the deformation resulting. With the lock-in amplifier (LIA, see figure 2.17) the A and φ are demodulated from the piezoresponse, providing information on the magnitude and the orientation of the displacement surface, respectively. The LIA components can also output the signal as a mixture of various components; by using a vector representation, the phase reference can be adjusted, and the X maximized [47]. The out-of-plane and in-plane components of the piezoresponse can be measured by the so-called vector PFM [48]. This is done by carrying out parallel measurements known as vertical PFM (VPFM) and lateral PFM (LPFM), as shown in figure 2.18 [45].

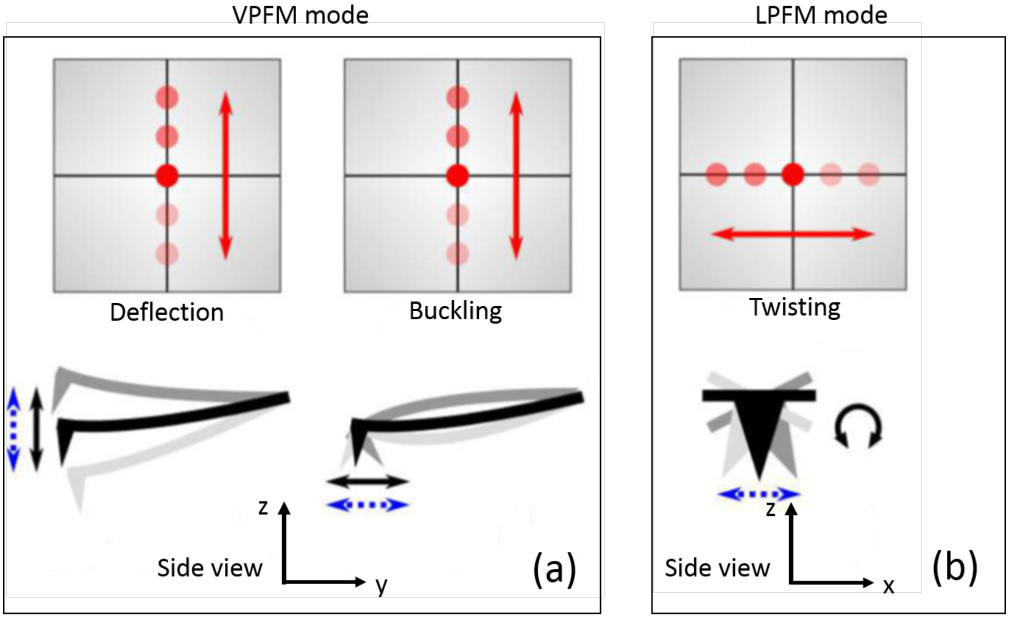

Figure 2.18. Cantilever motion in PFM. Flexural deflection and bucking for vertical PFM (a); lateral twisting for lateral PFM (b). The laser spot position, indicated in the upper part of the figure, represents changes on the position-sensitive detector (PSD). The double black arrows represent the cantilever motion and the dashed blue arrows the motion of the sample surface acting of the cantilever. Modified from [45].

The flexural deflection is due to an out-of-plane piezoresponse -displacement in the *z* direction- but the bucking is caused by an in-plane piezoresponse, parallel to the cantilever axis (in this case, the displacement is in *y* direction). The lateral twisting is caused by an in-plane piezoresponse perpendicular to the cantilever axis, with displacement in the *x* direction. The LPFM depends on the angle of the cantilever in the plane of the sample surface with respect to the in-plane piezoresponse orientation. In order to distinguish the different contributions, it is often necessary to perform the measurements at different cantilever angles.

2.4.2.1. Experimental details

The dual amplitude resonance tracking (DART) mode was used for PFM imaging. In DART mode, the sample is excited by an ac voltage at the tip's contact resonance frequency. The inverse piezoresponse signal of the sample, which causes a few picometers (pm) displacement oscillation, is naturally increased by the contact resonance frequency's quality factor Q. For these measurements, the tips used was an PPP-EFM Nanosensor, $PtIr_5$ coated.

2.5 Magnetoelectric characterization

In this paragraph, the magnetoelectric characterization will be explained in some detail. A "homemade" setup was used to apply the electric field. Electric field was applied out-of-plane while magnetic field was mainly applied in-plane, although sometimes also perpendicular-to-film directions, for P-MOKE measurements.

2.5.1 Magnetoelectric characterization of the thin film with vibrating sample magnetometry (VSM)

In a perpendicular holder, the thin film sample is fixed with a silver paste as a bottom electrode. For a top electrode a drop of silver paint is also used, as shown in figure 2.19 (a and b).

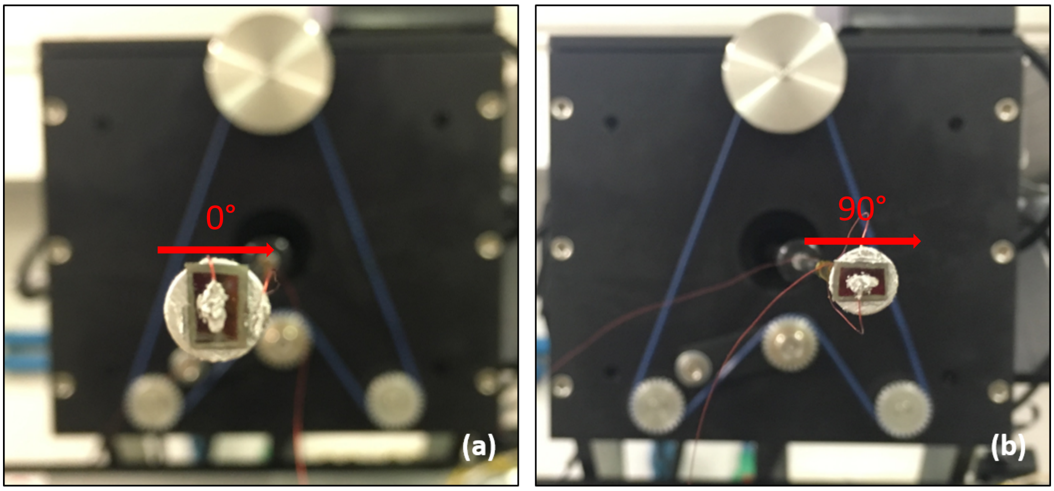

Figure 2.19. Sample in the VSM setup. As shown, the same sample was measured in two directions called "0" (a) and "90" (b) degree. It means that the magnetic field is applied in two orthogonal in-plane directions. Electric field is applied perpendicular to the film.

The magnetic and magnetoelectric properties were measured using the VSM setup, while the voltage is *in situ* applied out-of-plane using a power supply. As shown in figure 2.20, the top electrode consists of silver paint and the $Fe_{75}Al_{25}$ layer itself. The bottom electrode is made from silver paint to apply the electric field across the ferromagnetic-ferroelectric heterostructure [49]. The silver paste, used as a bottom electrode, has also the function to stick the sample to the non-conducting VSM holder.

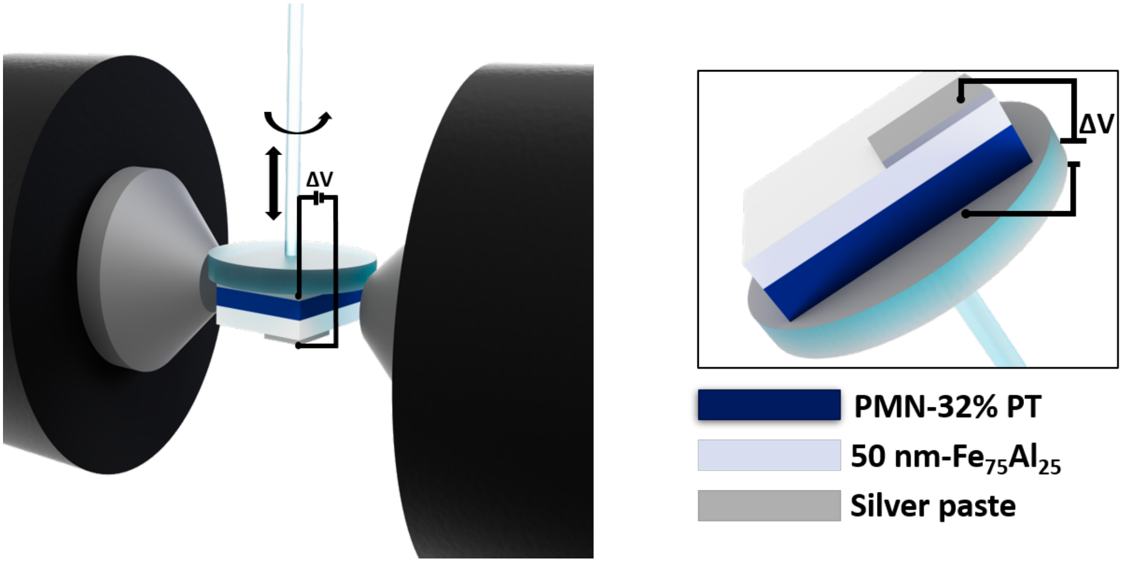

Figure 2.20. Schematic representation of the measurement's setup. The perpendicular holder allows rotating the sample to measure in two configurations 0 and 90 degrees. The multiferroic heterostructure is represented on the right.

The electric protocol was performed so that for first the hysteresis loops are recorded following the ascending branch of the ferroelectric loop. To be sure to achieve better control of the sample state, before each point of the protocol, the piezoelectric is always brought to ferroelectric saturation (-6 kV/cm). For each configuration (i. e. 0 and 90 degrees) I recorded 32 hysteresis loops starting for the ascending branch (A), as mentioned before, (e.g., –6 kV·cm^{-1}, –6 kV·cm^{-1}/ –4 kV·cm^{-1}, …, –6 kV·cm^{-1}/ 0 kV·cm$^{-1,}$ –6 kV·cm^{-1}/ 0 kV·cm^{-1}/ 0.5 kV·cm^{-1}, …, –6 kV·cm^{-1}/ 0 kV·cm^{-1}/ 6 kV·cm^{-1}). Then, the protocol was reversed -from positive to negative saturation- to collect the last 11 hysteresis loops corresponding to the descending branch (D) of the ferroelectric loop, specifically, –6 kV·cm^{-1}/ 0 kV·cm^{-1}/ 6 kV·cm^{-1}/ 4 kV·cm^{-1}, …, –6 kV·cm^{-1}/ 0 kV·cm^{-1}/ 6 kV·cm^{-1}/ 0 kV·cm^{-1}, –6 kV·cm^{-1}/ 0 kV·cm^{-1}/ 6 kV·cm^{-1}/ 0 kV·cm^{-1}/ –0.5 kV·cm^{-1}, …,–6 kV·cm^{-1}/ 0 kV·cm^{-1}/ 6 kV·cm^{-1}/ 0 kV·cm^{-1}/ –6 kV·cm^{-1}.

2.5.2 Magnetoelectric characterization of the lithographed sample with magneto-optical Kerr effect (MOKE)

2.5.2.1 Longitudinal and transverse MOKE

To perform the MOKE characterization, a non-conducting glass holder was used. As bottom electrode, and to stick the sample, silver paste is used, as shown in figure 2.21, the wires were connected to have an out-of-plane electrical poling.

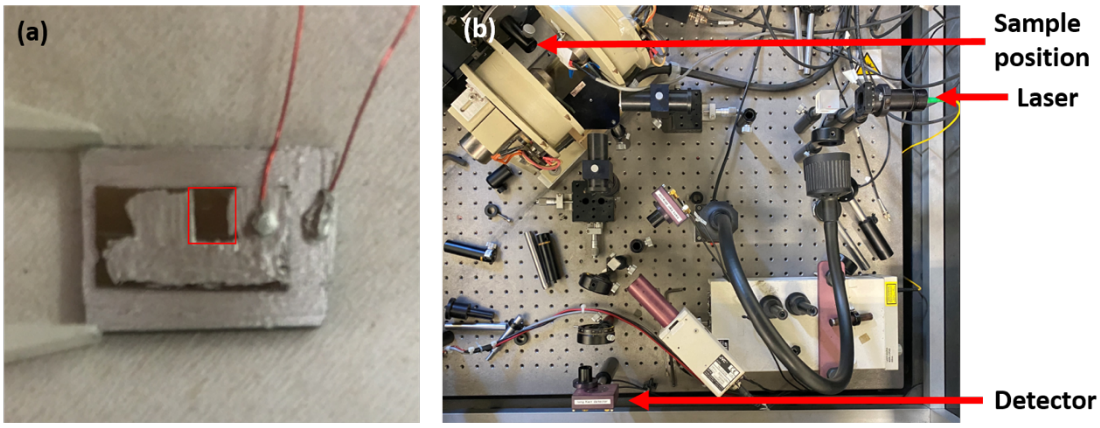

Figure 2.21. Lithographed sample (a) and the configuration setup (b). The red square represents the measured area.

The silver paste, used as a bottom electrode, was also used to cover the empty areas (i.e., not containing the square, dots, triangle, and “doughnuts” patterned motifs) of the sample, to be sure to have a homogeneous current distribution (see figure 2.22).

The protocol used, for each orientation, was the same used for the thin film in the VSM characterization. The voltage was applied *in situ* out-of-plane using a power supply; the piezoelectric was always brought to ferroelectric saturation (-8 kVcm^{-1}) before and after the hysteresis loops were recorded following the ascending branch of the ferroelectric loop. Later the protocol was reversed, from positive to negative saturation, to collect the descending branch of the ferroelectric loop. Circular dots with different diameters (i.e., ø ≈ 48 μm, ø ≈ 27 μm and ø ≈ 24 μm) were measured, but the most promising results were obtained for the dots with 24 μm diameter, therefore, we focused on them.

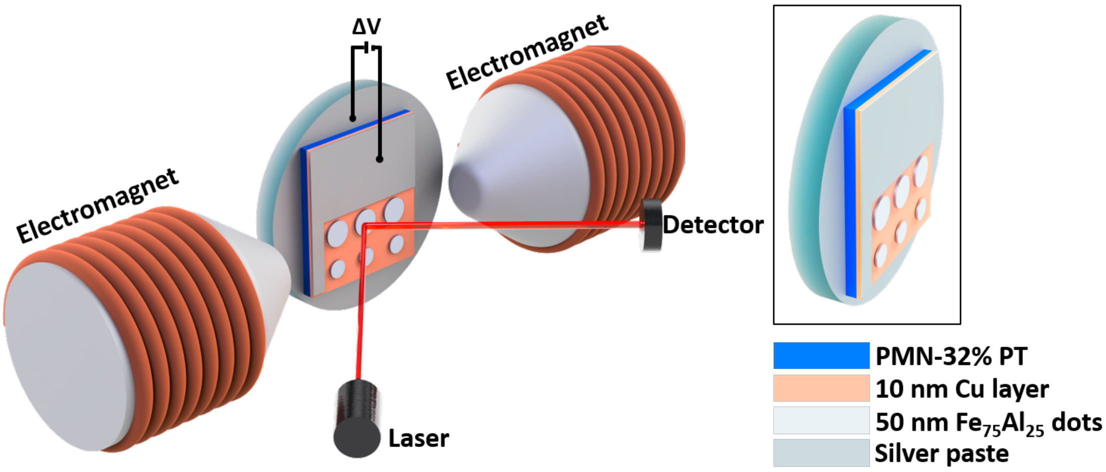
ΔV
Electromagnet
Electromagnet
Detector
Laser
PMN-32% PT
10 nm Cu layer
50 nm $Fe_{75}Al_{25}$ dots
Silver paste

Figure 2.22: Schematic representation of the measurement's setup. Hysteresis loops along two directions (0° and 90°) were recorded for the L-MOKE and T-MOKE configurations, simply rotating the holder. The Cu layer allows a homogeneous current distribution from the bottom electrode.

2.5.2.2 Polar MOKE

For the P-MOKE, the magnetization M is out-of-plane with respect to the light incidence plane; therefore, the configuration was changed, as is shown in figure 2.23.

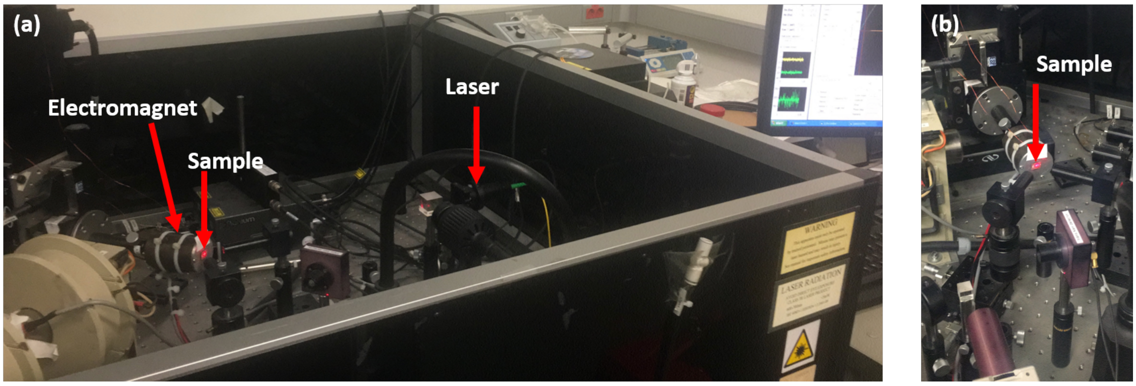
(a)
Electromagnet
Sample
Laser
(b)
Sample

Figure 2.23. The polar electromagnet setup used (a) and zoom-in of the region containing the sample (b).

In this case, the smallest dots (ø ≈ 24 μm diameter) were measured, modifying the previous protocol. As usual, the piezoelectric was brought to ferroelectric saturation before collecting the first hysteresis loop following the ascending branch, while the voltage was *in situ* applied out-of-plane using Agilent

B2902A power supply. Then the new protocol was reversed to register the hysteresis loop following the descending branch.

The schematic configuration of the P-MOKE setup is represented in figure 2.24.

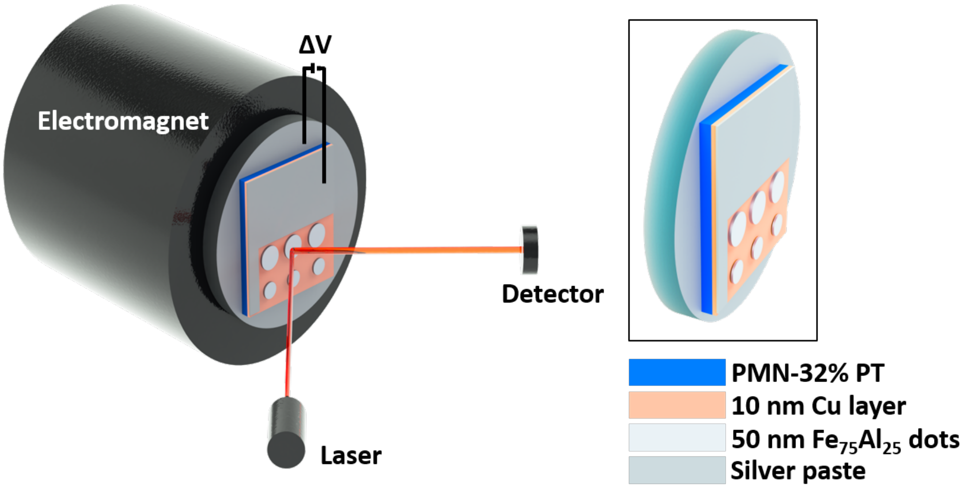
ΔV
Electromagnet
Detector
Laser
PMN-32% PT
10 nm Cu layer
50 nm $Fe_{75}Al_{25}$ dots
Silver paste

Figure 2.24. P-MOKE configuration setup.

A non-conductive carbon tape, commonly used in an SEM holder, was used to fix the sample at the electromagnet. Furthermore, I waited ten minutes between each point recorded because the electromagnet overheats during the measurement, due to the Joule effect; in this way, the influence of temperature could be minimized.

References

1. D. Mattox, *Handbook of Physical Vapor Deposition Processing* (Chapter in Physical Sputtering and Sputter Deposition, Second Edition) William Andrew Publishing. Burlington (2010).
2. AJA International INC, URL http://ajaint.vom/about-aja.html.
3. http://www.pvdtar.get.com/info/thin-film-deposition-20842616.html.
4. S.M. Rossnagel, *Sputter Deposition*. In: W.D, Sproul, K. O. Legg, editors. *Opportunities for Innovation: Advanced Surface Engineering*. Switzerland: Technomic Publishing Co., 1995.
5. J. I. Martín, J. Nogués, K. Liu, J. L. Vicent and I. K. Schuller *J. Magn. Magn. Mater.* **256** 449 (2003).
6. W. Friedrich, P. Knipping and M. Laue. Interferenzerscheinungen bei Röntgenstrahlen. *Annalen Der Physik* **346** 971 (1913).
7. W. H. Bragg, W. L. Bragg, *Proc. R. Soc*. Lond. A **88** 428 (1913).
8. https://www.azom.com/article.aspx?ArticleID=3604.
9. A. E. Ermakov, E. E. Yurchikov and V. A. Barinov *Phys. Met. Metall.* **52** 50 (1981).
10. C. C. Koch, O. B. Cavin, C. G. McKamey and J. O. Scarbrough *Appl. Phys. Lett.* **43** 1017 (1983).
11. C. Suryanarayana *Prog. Mat. Sci.* **46** 1 (2001).
12. H. P. Klug and L. E. Alexander**,** *X-ray diffraction procedures.* New York: Wiley, 1974.
13. B.D. Cullity, *Elements of X-Ray Diffraction*. Addison-Wesley, Upper Saddle River, 1-110 (1956).
14. L. Lutterotti and P. Scardi *J. Appl. Cryst.* **23** 246 (1990).
15. S. Enzo, G. Fagherazzi, A. Benedetti and S. Polizzi *J. Appl. Cryst.* **21** 536 (1988).
16. *PCPDFWIN* JCPDS-ICDD (1997).
17. J. I. Langford and D. Louër *Rep. Prog. Phys.* **59** 131 (1996).
18. U. Santhi, W. K. Ngui, M. Samykano, K. Sudhakar, K. Kadirgama, B. Sangmesh, and M. Asok Raj Kumar, AIP Conference Proceedings **2059**, 020006 (2019).
19. B. C. De Cooman, *Observation techniques in materials science.* Lecture notes Ghent University (2000).
20. G. Lawes, *Scanning Electron Microscopy and X-Ray Microanalysis*, John Wiley & Sons, New York (1987).
21. L. Reimer, *Scanning Electron Microscopy*, Springer Verlag, New York (1985).
22. D. B. Williams and B. C. Carter, *Transmission electron microscopy: A textbook for materials science.* New York: Plenum Press (1996).
23. https://commons.wikimedia.org/wiki/File:Schematic_view_of_imaging_and_diffraction_modes_in_TEM..tif.

24. J. P. Goodhew; J. Humphreys; R. Beanland, *Electron microscopy and analysis.* [ed.] Taylor& Francis. London: s.n. (2001).
25. R. W. Kelsall, I. W. Hamley, and M. Geoghegan, *Nanoscale Science and Technology*, John Wiley & Sons Ltd, 2005.
26. https://myscope.training/legacy/tem/background/concepts/imagegeneration/setup.php,
27. M. Z. Baykara, T. C. Schwendemann, E. I. Altman and U. D. Schwarz *Adv. Mater.* **22** 2838 (2010).
28. M.Z. Baykara, and U.D. Schwarz *Atomic Force Microscopy: Methods and Applications*. In: Lindon, J.C., Tranter, G.E., and Koppenaal, D.W. (eds.) *The Encyclopedia of Spectroscopy and Spectrometry*, 3rd edition. Oxford: Academic Press. (2017).
29. http://perso.univ-lemans.fr/~bardeau/IMMM-PEC/afm/afmintroduction.html.
30. http://slideplayer.com/slide/9702681/31/images/9/Modes+of+operation.+There+are+3+modes+of+AFM+operation+Contact+mode.jpg.
31. J. R. Reitz, F. J. Milford and R. W. Christy *Foundations of electromagnetic theory* Addison-Wesley, New York (1979).
32. S. Chikazumi *Physics of Magnetism.* John Wiley & Sons, Inc., New York (1964).
33. P. N. Argyres, *Phys. Rev.* **97** 334 (1954).
34. S. D. Bader, *J. Magn. Magn. Mater.* **100** 440 (1991).
35. W. Geerts, *PhD Thesis* University of Twente, The Netherlands (1992).
36. A. Hubert and R. Schafer, *Magnetic Domains. The Analysis of Magnetic Microstructures.* Springer, Berlin (1998).
37. T. Haider, *Int. J. of Electromagnetics and Applications*, **7,** 17 (2017).
38. D. A. Allwood, G. Xiong, M. D. Cooke and R. P. Cowburn *J. Phys. D: Appl. Phys.* **36** 2175 (2003).
39. R. P. Cowburn, D. K. Koltsov, A. O. Adeyeye and M. E. Welland, *Appl. Phys. Lett.* **73** 3947 (1998).
40. http://www.veeco.com.
41. http://www.nanophys.kth.se/nanophys/facilities/nfl/afm/icon/brukerhelp/Content/Interleave%20Scanning/Magnetic%20Force%20Microscopy%20(MFM).htm.
42. C. B. Sawyer and C H Tower, *Phys Rev*, **35** 269 (1930).
43. I. Fina, *PhD Thesis* University of Barcelona, Spain (2012).
44. P. Güthner, K. Dransfeld, *Appl. Phys. Lett.* **61** 1137 (1992).
45. D. Denning, J. Guyonnet and B. J. Rodriguez, *Int. Mat. Rev.* **61** 46 (2016).
46. https://www.azonano.com/article.aspx?ArticleID=2682.
47. E. Soergel, *J. Phys. D Appl. Phys*, **44** 464003 (2011).
48. S. V. Kalinin, B. J. Rodriguez, S. Jesse, J. Shin, A. P. Baddorf, P. Gupta, H. Jain, D. B. Williams and A.Gruverman, *Microscopy and Microanalysis,* **12** 206 (2006).

49. E. Menéndez, V. Sireus, A. Quintana, I. Fina, B. Casals, R. Cichelero, M. Kataya, M. Stengel, G. Herranz, G. Catalán, M. D. Baró, S. Suriñach and J. Sort, *Phys. Rev. Appl.* **12** 014041 (2019).

3

Results and discussion

3. Results and Discussion

As mentioned in Chapter 1, one of the main strategies to control magnetism by voltage is to use magnetostrictive-piezoelectric materials, such as ferromagnetic-ferroelectric heterostructures. Indeed, due to its energy efficiency implications, electric control of magnetism has attracted scientific and technical attention in recent years, envisaging ultra-low power dissipation magnetic storage and magneto-electronic devices.

Single crystals of (1-x)$Pb(Mg_{1/3}Nb_{2/3})O_3$–x$PbTiO_3$ (PMN-xPT) with composition around the morphotropic phase boundaries (i.e., x around 35 mol %, described in Chapter 1) are one of the most widely used ferroelectric materials due to their piezoelectric response [1-5].

Furthermore, the low cost of Fe and Al makes their alloys good ferromagnetic materials candidates. In fact, with Al substitution, the magnetostriction constant increases, the maximum value around 100 ppm it is achieved when around 20 at. % of Al is present [6], the system is also oxidation resistant [7], and soft ferromagnetic [8].

Thickness is another parameter to consider. A thickness of 50 nm disables any possible effect arising from charge accumulation. The high resistance to oxidation ensures that the voltage-driven oxygen migration process is minimized, leaving strain as the only mechanism to modulate the magnetoelectric response, which is asymmetric with respect to the sign of the applied voltage, in contrast to the typical strain-induced magnetoelectric effect.

This chapter deals with the main results of this Thesis and their discussion. It will be divided in two parts. The first part is focused on continuous $Fe_{75}Al_{25}$ thin film deposited on [110]-oriented PMN-32PT and its magnetic characterization.

The second one is focused on the growth of $Fe_{75}Al_{25}$ microstructures on top of [011]-oriented PMN-32PT by photolithography. The process of miniaturization leads to new properties, which can be used in spintronic devices.

3.1 Voltage control of magnetism in continuous FeAl/PMN-32PT

Studies on how to disentangle e magnetoelectric effects in complex multiferroic systems, described in chapter 1, have been carried out in engineered FM-FE heterostructures, which comprise a magnetically soft and isotropic 50 nm thick $Fe_{75}Al_{25}$ (at %) thin film grown on top of a [110]-oriented PMN-32PT ferroelectric crystal. In the following paragraph, the morphological, structural, magnetic and magnetoelectrical characterizations will be described.

3.1.1 Heterostructure preparation

50 nm thick $Fe_{75}Al_{25}$ (at. %) films are grown by co-sputtering at room temperature on [110]-oriented PMN-32PT single crystals using an AJA International, Inc. magnetron sputtering system. Depositions are carried out at a rate of around 0.6 Å/s. The $Fe_{75}Al_{25}$ films are grown on 0.5-mm thick and 3×4 mm^2 rectangular-shaped [110]-oriented PMN-32PT substrates, as shown, schematically, in figure 3.1.

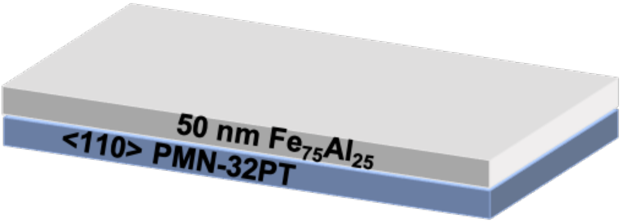

Figure 3.1: Schematic representation of the sample.

3.1.2 Structural and morphological characterization

Structural characterization was carried out by $\theta/2\theta$ XRD, grazing incidence XRD (GIXRD) with an incidence angle of 1° using Cu Kα radiation in a Malvern-PANalytical X'pert Pro materials research diffractometer.

By comparing the $\theta/2\theta$ XRD measurement of the [110]-oriented PMN-32PT crystal and the $Fe_{75}Al_{25}$/ PMN-32PT bilayer, figure 3.2, there is only one peak corresponding to the $Fe_{75}Al_{25}$ film, located at around 44.4°. This is consistent with the (110) reflection of an $Fe_{75}Al_{25}$ phase, evidencing that grows with a strong crystallographic texture.

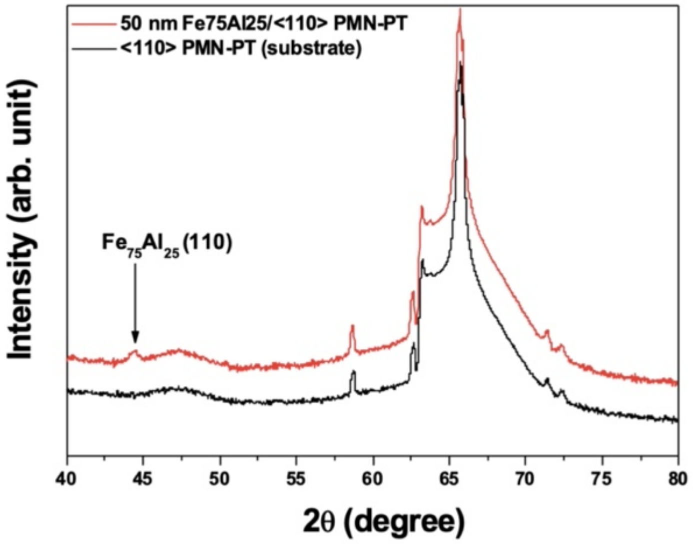

Figure 3.2: $\theta/2\theta$ x-ray diffraction patterns corresponding to a pristine (i.e., as-deposited) 50-nm thick $Fe_{75}Al_{25}$ / [110]-oriented PMN-32PT sample (black line) and a bare [110]-oriented PMN-32PT substrate (red line).

Moreover, the (110) peak, which appears in the GIXRD measurement, evidence that the $Fe_{1-x}Al_x$ layer, shown in figure 3.3, despite being highly textured, does not grow epitaxially.

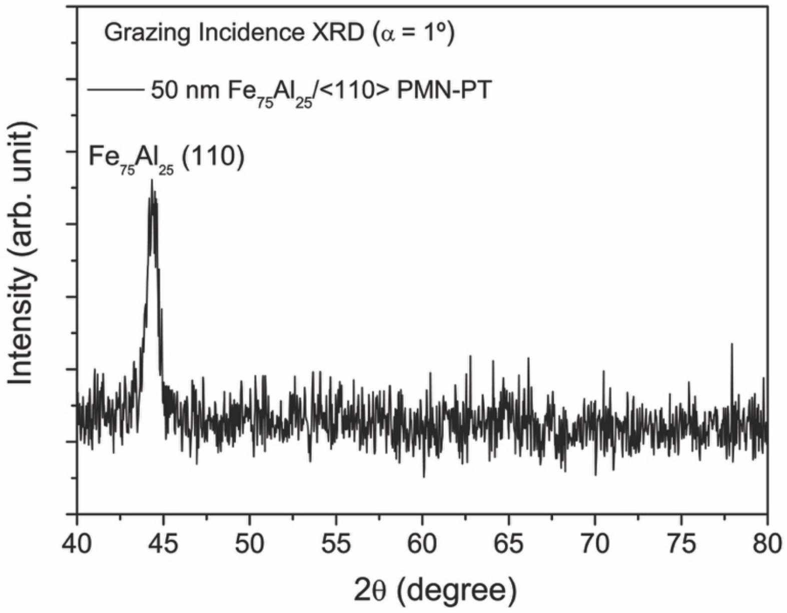

Figure 3.3: Grazing incidence X-ray diffraction (GIXRD) pattern, recorded using an incident angle of 1°, of a pristine (i.e., as-deposited) 50 nm-thick $Fe_{75}Al_{25}$/[110] PMN-32PT sample.

In figure 3.4 is reported the top view SEM images of the sample surface. It indicates that it is granular along the plane of the sample, showing a strong degree of in-plane polycrystallinity.

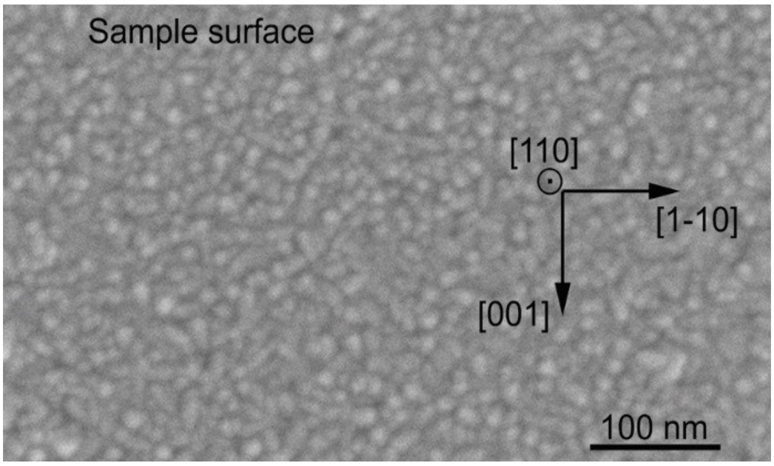

Figure 3.4: Scanning electron microscopy image taken using secondary electrons in a FEI Magellan 400L microscope operates at 20kV of the surface of a 50-nm thick $Fe_{75}Al_{25}$/ [110] PMN-PT sample.

To investigate the inner parts of the as-grown samples, a cross-section lamella was prepared by focused ion beam and placed onto a Cu TEM grid, showed in figure 3.5 (a). The TEM image of a cross section of the heterostructure evidence that the $Fe_{75}Al_{25}$ layer is indeed around 50-nm thick. The TEM images show that an interfacial layer between the substrate and the $Fe_{75}Al_{25}$ layer of about 5 nm is formed.

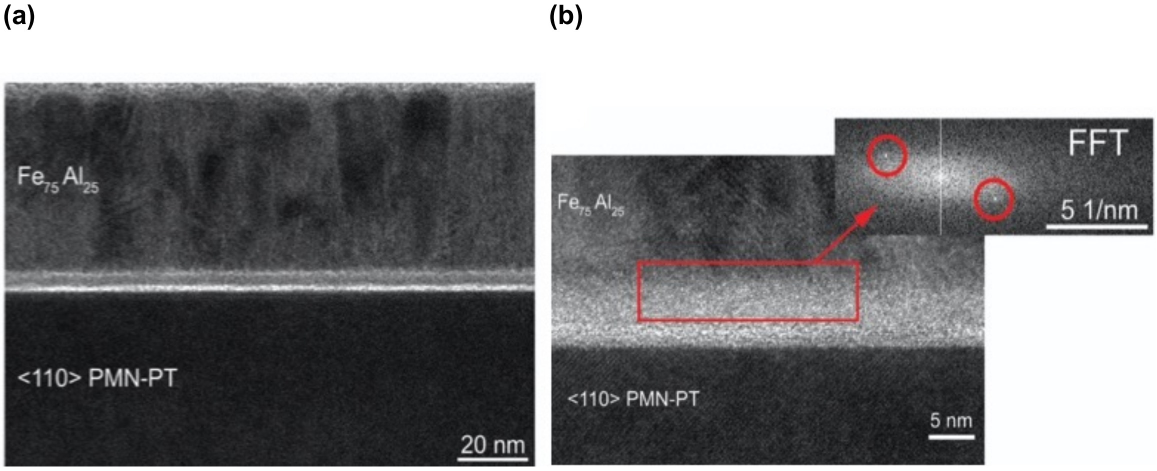

Figure 3.5: (a) Transmission electron microscopy (TEM) image of the cross section along [1–10] of a pristine 50-nm thick $Fe_{75}Al_{25}$ / [110] PMN-32PT sample. (b) High resolution TEM image of the interface layer formed between the $Fe_{75}Al_{25}$ film and the PMN-32PT substrate. The inset shows the FFT of the area marked with a red rectangle.

The composition of the $Fe_{75}Al_{25}$ layer is determined to be $Fe_{75}Al_{25}$ (at. %) by TEM-EDX. As can be seen in the compositional analysis carried out by HAADF STEM [Fig. 3.6], the interfacial layer is rich in O and Al. HRTEM (Fig. 3.5) reveals that this interface layer is partly crystalline. The FFT corresponding to the red rectangle in Fig. 3.5 (b) results in two spots, which correspond to an interplanar distance of 3.47 Å, which is compatible with the (012) planes of rhombohedral Al_2O_3 (00-001-1243), in concordance with the compositional mappings of figure 3.6.

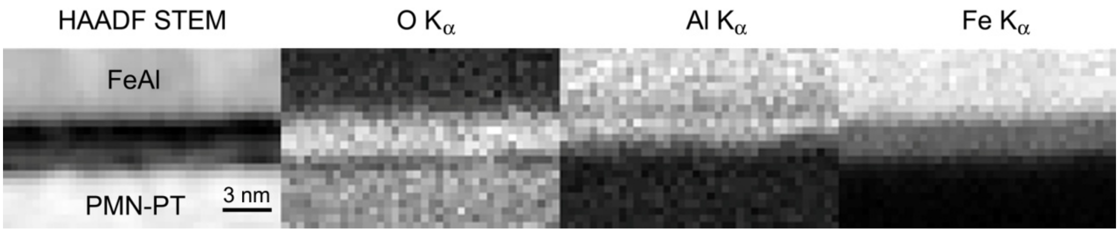

Figure 3.6: High-angle annular dark-field (HAADF) compositional image taken in scanning transmission electron microscopy (STEM) together with the O, Al and Fe elemental mappings (the Kα transition is the one mapped for all three elements).

3.1.3 Ferroelectric characterization

Figure 3.7 shows, in a schematic way, the sample and the main crystallographic directions of the PMN-32PT crystal.

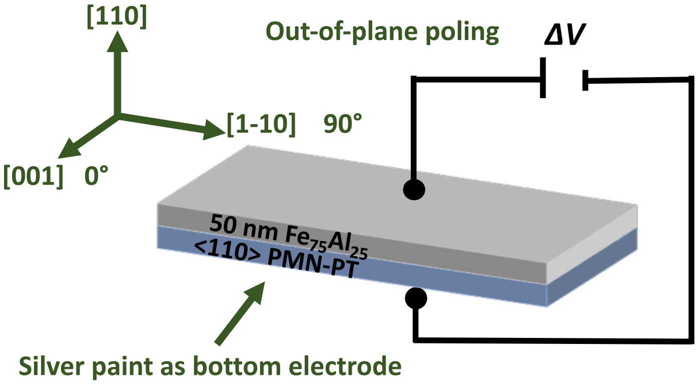
[110]
Out-of-plane poling
ΔV
[1-10] 90°
[001] 0°
50 nm Fe75Al25
<110> PMN-PT
Silver paint as bottom electrode

Figure 3.7: Schematic representation of the out-of-plane poling applied to the samples.

The ferroelectric polarization (P) versus applied voltage (i.e., electric field, E) loop is shown in figure 3.8 (a). The ferroelectric hysteresis loop was measured in quasi-static conditions. Figure 3.8 (b) shows the dependence of the square of the electric polarization (P^2) as a function of electric field.

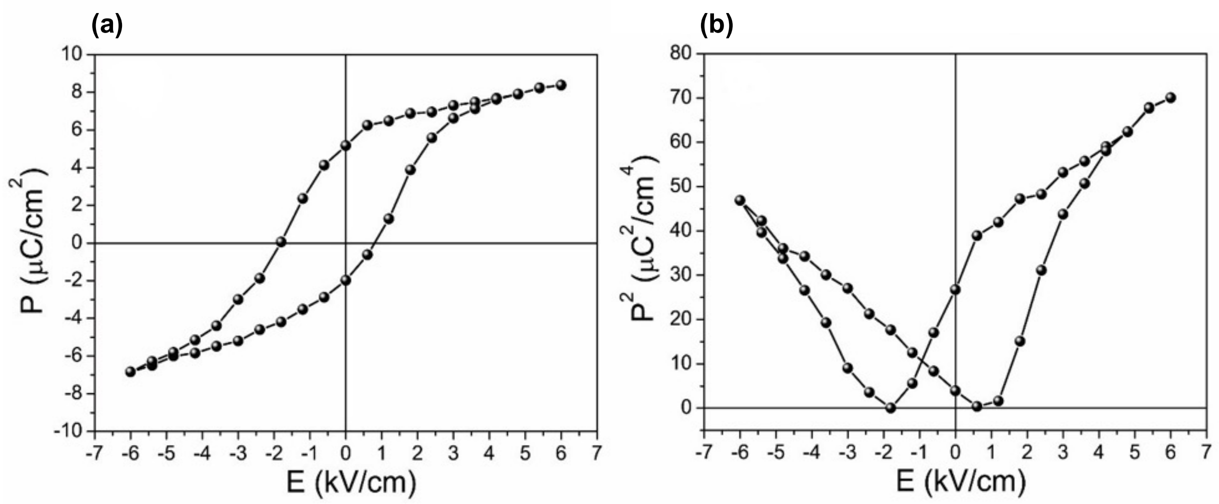

Figure 3.8: (a) Ferroelectric hysteresis loop (electric polarization P vs applied electric field E) of an as-deposited 50-nm thick $Fe_{75}Al_{25}$/ [110] PMN-32PT sample. (b) Square of P (which is proportional to the piezoelectric strain) vs E.

P^2 is proportional to the deformation that the PMN-32PT undergoes when subjected to an electric field due to its piezoelectricity [9]. Interestingly, (110)-cut PMN-32PT single crystals in an out-of-plane poling configuration do not only display anisotropic in-plane piezoelectric coefficients, which results in compressive and tensile stresses along [001] and [1–10] directions, respectively, but also a strong strain response when the fraction of PT is within the region of the morphotropic phase boundary (i.e., is around 35 mol. %) [2, 9–11]. Remarkably, the ferroelectric loop, figure 3.8 (a), is not symmetric. This could be ascribed to the interplay of the following aspects: (i) electrode asymmetry (the bottom electrode is made by silver paste, while the top electrode consists of the $Fe_{75}Al_{25}$ layer and silver paste), which might lead to asymmetric electric fields at the interfaces with the sample; (ii) macroscopic defect gradients [12]; and (iii) difficulty to reach saturation of the electric polarization (i.e., unsaturated loop), meaning that the initial polarity dominates thus, envisaging complex and path-dependent ferroelectric reversal mechanisms [13].

3.1.4 Magnetic characterization

In the absence of an electric field, the sample shows an isotropic in-plane magnetic behavior [figure 3.9 (a-c)] as expected from the high degree of in-plane polycrystallinity in the plane of the sample. This is very convenient to disentangle magnetoelectric effects since they may result in anisotropic changes of magnetic anisotropy as it happens in other heterostructures, such as $Co_{40}Fe_{40}B_{20}$/PMN-*x*PT [14-16].

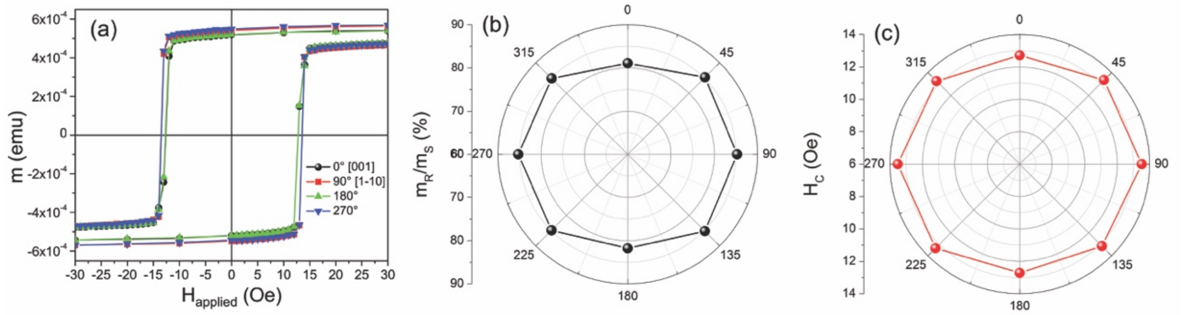

Figure 3.9: In-plane magnetic characterization of as-deposited sample by vibrating sample magnetometry. (a) Hysteresis loops at 0, 90, 180 and 270°. (b) and (c) are the angular dependence of the magnetic moment at remanence normalized by the magnetic moment at saturation (m_R/m_S) and coercivity (H_C), respectively.

3.1.5 Magnetoelectric characterization

The magnetoelectric characterization is carried out by in-plane vibrating sample magnetometry while out-of-plane poling (i.e., the electric field is applied along the [110] direction, which is perpendicular to the sample plane). A larger number of points are recorded close to the ferroelectric coercive field since it is in this region where the largest changes in strain are achieved. Figure 3.10 shows the VSM characterization as a function of the applied voltage while applying the in-plane magnetic field along [001] (i.e., 0° configuration).

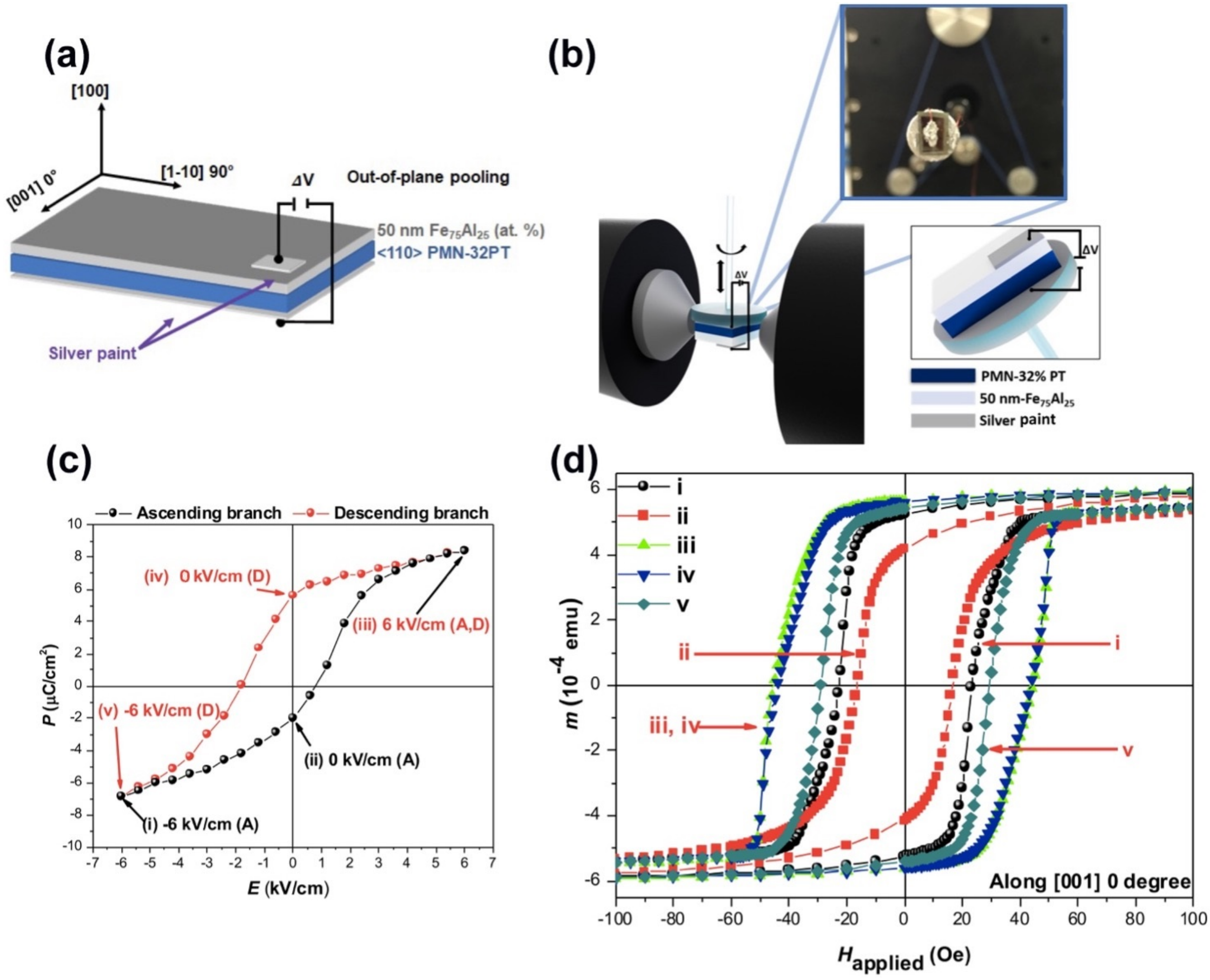

Figure 3.10: (a) Schematic representation of the sample, the main crystallographic directions of the 0.50 mm thick [110] PMN-32PT crystals and the out-of-plane pooling, (b) 0° VSM setup, (c) ferroelectric loop and (d) Hysteresis loops recorded along in-plane direction [001] (0°configuration) at a given applied electric field, applied out-of-plane. The loops shown correspond to the points indicated in the ferroelectric loop in panel (c), e.g., point (iii) in the ferroelectric loop correspond to the green loop (iii) in panel (d). Before registering the magnetic measurements at a given electric field, the piezoelectric is always brought to ferroelectric saturation at -6 kV/cm.

The samples are subjected to the following electric protocol (table 3.1) [17]: First, hysteresis loops are recorded while following the ascending branch (A) of the ferroelectric loop. The piezoelectric is always brought to ferroelectric saturation at −6 kV/cm before applying the indicated measurement voltage to achieve better control of the sample state. Then, the protocol is reversed (i.e., from positive to negative saturation) to apply electric fields corresponding to the descending branch (D) of the ferroelectric loop (shown in figure 3.10(c)).

Saturation before measuring for Ascending branch	**The electric field applied (kV/cm)**
–6 kV/cm	–6 kV/cm
–6 kV/cm	–4 kV/cm
…	…
–6 kV/cm	0 kV/cm
–6 kV/cm	0.5 kV/cm
…	…
–6 kV/cm	6 kV/cm
Saturation before measuring for Descending branch	**The electric field applied (kV/cm)**
–6 kV/cm; 0 kV/cm; 6 kV/cm	4 kV/cm
–6 kV/cm; 0 kV/cm; 6 kV/cm	0 kV/cm
…	…
–6 kV/cm; 0 kV/cm; 6 kV/cm; 0 kV/cm	–0.5 kV/cm
…	
–6 kV/cm; 0 kV/cm; 6 kV/cm; 0 kV/cm	-6 kV/cm

Table 1 The voltage protocols. (Left column) Before each measurements the sample was brought at the ferroelectric saturation, -6 kV/cm for the loops collected following the ascending branch of the ferroelectric loop (figure 3.8) and, -6 kV/cm; 0 kV/cm; 6 kV/cm for the loops collected following the descending branch of the ferroelectric loop; (right column) electric field applied to collect the loops.

For the 0° configuration, although the behavior is asymmetric, the dependences of both the remanence (i.e., squareness, m_R/m_S) and the coercivity (H_C) with the applied electric field along [001] show an important component with a butterfly-like shape (figures 3.11(a) and 3.11(b), respectively), resembling the variation of strain with voltage in a piezoelectric material, figure 3.8 (b).

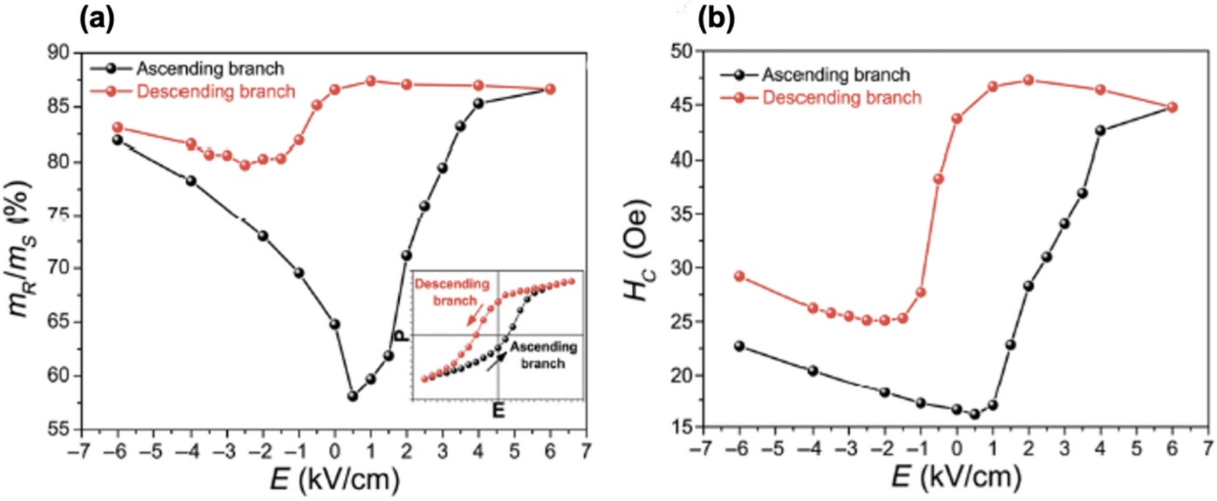

Figure 3.11: (a) Dependences of the magnetic moment at remanence normalized by the magnetic moment at saturation (m_R/m_S) and (b) coercivity (H_C) with the applied electric field, while applying the in-plane magnetic field along [001] . Ascending (A) and descending (D) refer to the branches of the ferroelectric hysteresis loop as sketched in the inset of panel (a).

Subsequently, the holder was rotated in-plane in the VSM to perform the measurements along [1-10] direction. The loops recorded along this direction are shown in figure 3.12.

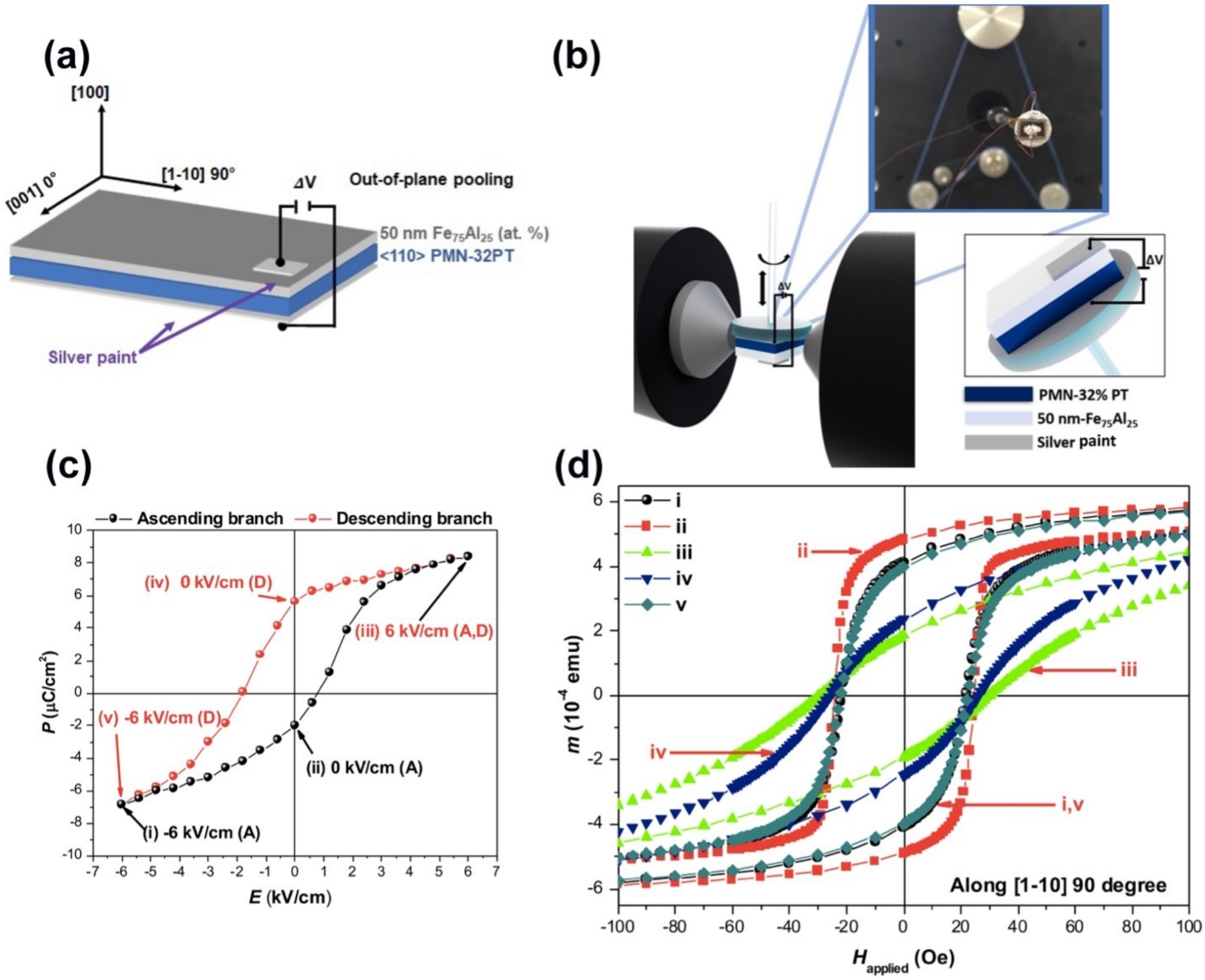

Figure 3.12 (a) Schematic representation of the sample, the main crystallographic directions of the 0.50 mm thick [110] PMN-32PT crystals and the out-of-plane pooling, (b) 90° VSM setup, (c) ferroelectric loop and (d) Hysteresis loops recorded along in-plane direction [1-10] (90°configuration) at a given applied electric field, applied out-of-plane. The loops shown correspond to the points indicated in the ferroelectric loop in panel (c), e.g., point (ii) in the ferroelectric loop correspond to the red loop (ii) in panel (d). Before registering the magnetic measurements at a given electric field, the piezoelectric is always brought to ferroelectric saturation at -6 kV/cm.

A quite different dependence is observed when the magnetization is measured along the [1-10] direction, figure 3.13 (a) and (b). In this case, while the dependence of the magnetic coercivity on the applied electric field is rather weak, that of the squareness (i.e., m_R/m_S) exhibits a looplike shape with an asymmetry with respect to the electric polarity much more pronounced than when magnetization is measured along the [001] direction (see figure 3.11).

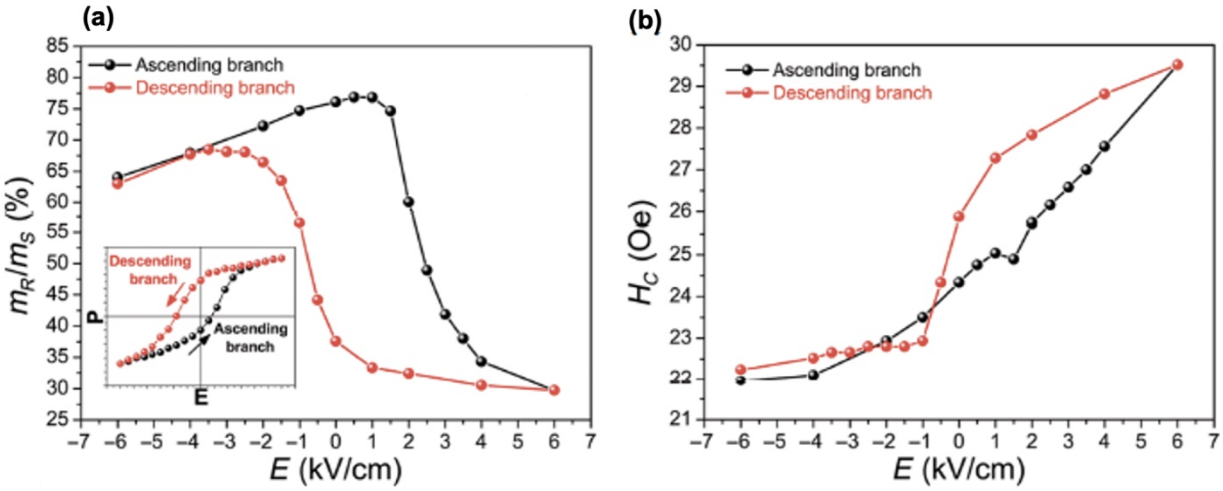

Figure 3.13: (a) Dependences of the magnetic moment at remanence normalized by the magnetic moment at saturation (m_R/m_S) and, (b) coercivity (H_C) with the applied electric field, while applying the in-plane magnetic field along [1-10]. Ascending (A) and descending (D) refer to the branches of the ferroelectric hysteresis loop as sketched in the inset of panel (a).

For the 50 nm thick sample, the maximum relative change in remanence is around 61.4%. The interfacial charge effects are ruled out as the main mechanism governing this reorientation of the magnetic easy axis with voltage. The sample also shows an Al_2O_3-based interfacial layer of around 5 nm in thickness at the interface with the [110]-oriented PMN-32PT. Regarding the role of these Al_2O_3-based interfacial layers in possible charge-mediated effects, 50- nm thick $Fe_{75}Al_{25}$ layers are still too thick to exhibit significant direct field effects.

Subsequently, we focus on possible voltage-driven oxygen migration (i.e., magneto-ionics) phenomena since this magnetoelectric mechanism is polarity dependent and it could result in strong permanent (non-volatile) changes [18–22]. As can be seen in figure 3.14 a and b, the magnetic moment at saturation remains virtually constant during the voltage protocol, changes are lower than 2% and the maximum change is related to an increase in magnetic moment, indicating that no oxidation occurs during voltage actuation.

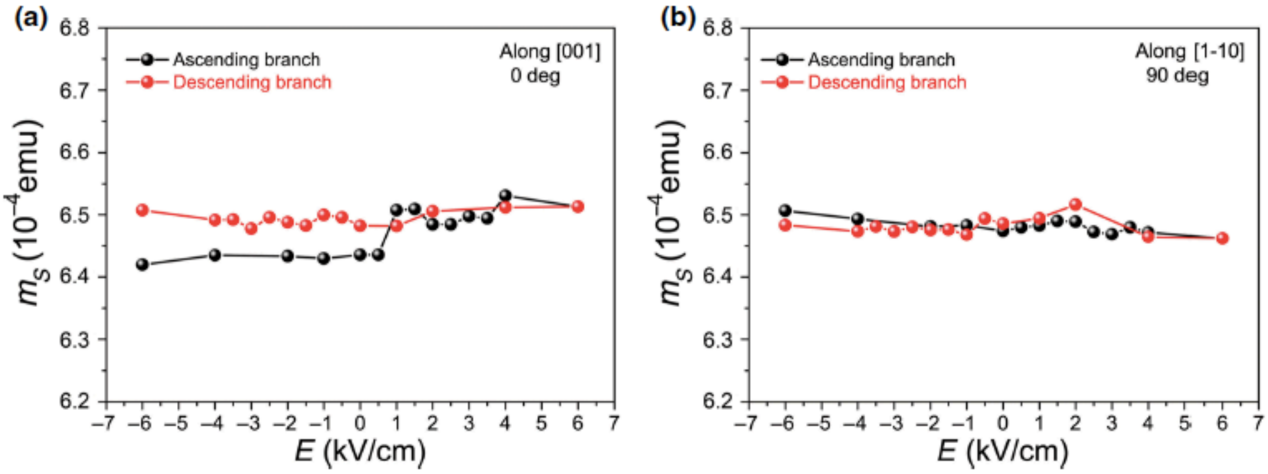

Figure 3.14: (a) and (b) dependences of the magnetic moment at saturation with the applied electric field when the magnetic field is applied along the [001] (0° configuration) or [1–10] (90° configuration) directions, respectively.

This in agreement with the structural characterization, which evidences the formation of an interfacial layer based on Al_2O_3, which acts as a barrier for oxygen migration, isolating and protecting the system from further oxidation.

3.1.6 Discussion

The magnetoelectric behavior of 50-nm thick $Fe_{75}Al_{25}$ (at. %) films grown onto [110] PMN-32PT substrates is investigated in detail by performing in-plane vibrating sample magnetometry along the [001] and [1–10] directions of the [110] PMN-32PT while applying an external out-of-plane electric field.

Concerning the measurements along the [001] direction, the dependence of the magnetic moment at remanence normalized by the magnetic moment at saturation (m_R/m_S) and coercivity (H_C), represented in figure 3.11 (a) and (b) respectively, show an asymmetric behavior and an important component with a butterfly-like shape. This reminds the variation of strain with voltage in a piezoelectric material, figure 3.8.

This is consistent with the converse magnetoelectric effect being dominated by strain coupling via inverse magnetostriction. In addition to the strain contribution, the observed asymmetry with electric field polarity could be a fingerprint of the coexistence of strain and charge effects through magneto-electro-elastic effects [23], since strain is proportional to P^2 whereas direct field effects are a function of P. However, considering that the electric field in metals (e.g., $Fe_{75}Al_{25}$) is strongly screened at the surface, resulting in no penetration beyond the Thomas-Fermi screening length (which is around 0.5 nm) [24, 25], charge effects due to the accumulation of electrostatic charges at the surface are rather unlikely to be significant since the $Fe_{75}Al_{25}$ layers are 50-nm thick. Anyhow, this in-plane magnetic asymmetry could be linked to the non-symmetric perpendicular-to-plane ferroelectric behavior of the PMN-32PT [i.e., non-saturated (i.e., minor) ferroelectric loop], envisaging that path-dependent mechanisms of electric polarization reversal could also be a source of magnetic asymmetry.

However, the measurements performed along the [1-10] direction show a notable difference. On the one hand, the magnetic coercivity dependency on the electric field applied is very weak, on the other hand, the squareness, (i.e., m_R/m_S), exhibits a looplike shape with an asymmetry with respect to the electric polarity much more pronounced if compared with the measure along the [001] direction.

Although the $Fe_{75}Al_{25}$ film is exceedingly thick to present significant charge-mediated effects, the effects of charge accumulation might propagate within the spin-spin exchange correlation length, which extends several nm toward the interior of the alloy [25]. To verify this possibility, a thinner $Fe_{75}Al_{25}$ film (20-nm thick) is grown in the same fashion with the aim to enhance eventual surface charging effects. As can be seen in figure 3.15, the dependence of the squareness (i.e., m_R/m_S), along [1–10] (i.e., 90° configuration), with the applied electric field also exhibit a loop-like dependence but the relative changes are, in fact, less pronounced in this thinner sample.

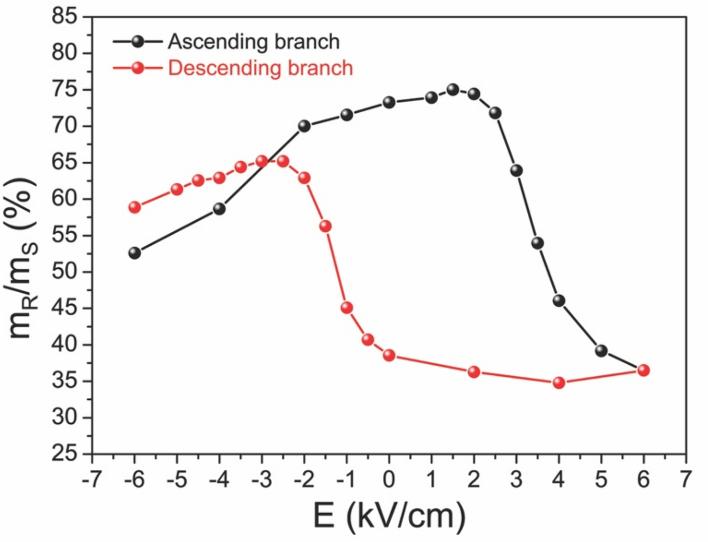

Figure 3.15: Magnetic moment at remanence normalized by the magnetic moment at saturation (m_R/m_S) as a function of the applied electric field corresponding to a 20 nm-thick $Fe_{75}Al_{25}$ film characterized along in-plane direction [1–10]. The piezoelectric is always brought to ferroelectric saturation at –6 kV/cm before registering the hysteresis loop at a given voltage, following an analogous protocol to that presented in the main text. Ascending and descending refers to the branches of the ferroelectric hysteresis loop.

Considering the magnetic moment at saturation, it remains virtually unaltered with voltage, ruling out voltage-driven O migration as an operative magnetoelectric mechanism [figure 3.14 (a) and (b)]. Conversely, both the remanence (i.e., m_R/m_S) and the coercivity (H_C) exhibit a strong dependence on the applied voltage (amplitude and sign, figures 3.11 (a) and (b) and 3.13 (a) and (b)).

In addition, the $\theta/2\theta$ XRD measurement of a sample subjected to a full voltage protocol shows no traces of phases other than $Fe_{75}Al_{25}$, further confirming the protective character of the amorphous Al_2O_3-based interface layer (figure 3.16) and the resistance of $Fe_{75}Al_{25}$ to oxidation.

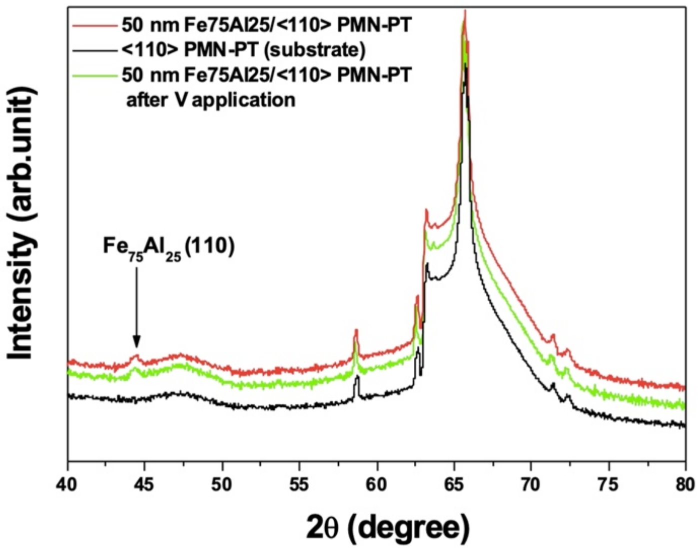

Figure 3.16: $\theta/2\theta$ X-ray diffraction patterns corresponding to a pristine (i.e., as-deposited) 50 nm-thick $Fe_{75}Al_{25}$/[110] PMN-32PT sample (black line), a bare [110] PMN-32PT substrate (red line) and a 50 nm-thick $Fe_{75}Al_{25}$/[110] PMN-32PT sample subjected to a full voltage protocol (green line).

Concerning the asymmetry in the measured ferroelectric hysteresis loop of the PMN-32PT [figure 3.8 (a)] and ruling out voltage-driven electronic charging and oxygen migration effects, the magnetoelectric behavior of the sample seems to be solely governed by strain-mediated effects (i.e., by the ferroelectric and/or piezoelectric nature of the PMN-32PT). Thus, the strong in-plane magnetoelectric asymmetry along in-plane [001] and [1–10] axes in our [110]-oriented crystals might be related to the specific symmetry related ferroelectric response of our [110]- oriented PMN-32PT crystals as compared to the more usual [100]-oriented substrates. PMN-PT compositions around the morphotropic phase boundary exhibit a complex phase diagram. Specifically, poling along [110] results in [111] and [11−1] as statistically equivalent spontaneous polarization directions [19]. Moreover, considering a pseudo-cubic cell for [110] PMN-32PT, [111] fully falls in the plane determined by [110] and [001], figure 3.17.

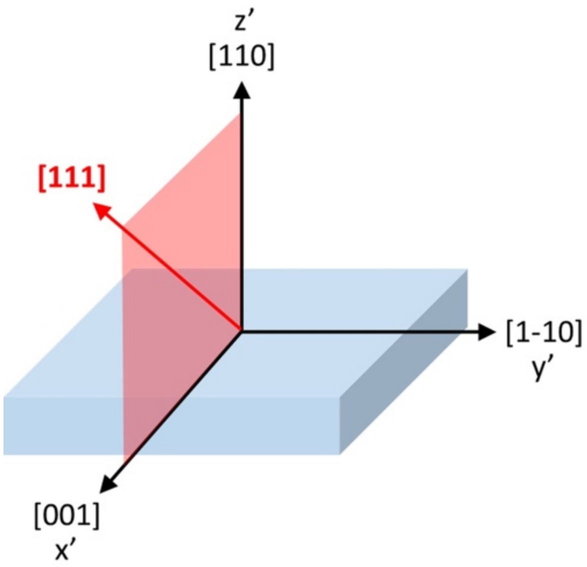

Figure 3.17: Scheme of the main crystallographic directions corresponding to a [1–10] PMN-PT single crystal. [111] fully falls in the plane determined by [110] and [001].

Ferroelectric reversal in this material can take place via nucleation and domain wall movements of 71°, 109°, and 180° domain walls [26–29]. In $BiFeO_3$, which is a model multiferroic with a rather similar crystalline structure, the domain wall energy γ follows the sequence: $\gamma_{109^\circ} < \gamma_{180^\circ} < \gamma_{71^\circ}$[27]. Specifically, on top of single 180° switching, there are consecutive 71°+109° switching events. Domain walls of 180° and 71° imply a polarization reversal, which takes place in the same plane (i.e., the plane where [111] lies), resulting in minimized in-plane distortions along [1–10]. Conversely, 109° domain walls lead to a 90° twist of the polarization (the polarization rotates out of the plane of the domain wall), giving rise to significant in-plane distortions along [1–10]. To some extent, 109° domain walls resemble ferromagnetic Bloch domain walls [28]. In other words, particularly when loops are unsaturated, a path-dependent polarization reversal, on top of 180° switching events, is enabled through ferroelastic switching, consecutive 71°+109° switching.

In crystals oriented with [001] out of the plane, and thus parallel to the electric field, this occurs isotropically: all in-plane switching directions are energetically equivalent, therefore, all ferroelastic switching events are equally probable and happen in the same proportion. In contrast, [110]- oriented crystals are not isotropic in-plane (i.e., [001] and [1–10] orthogonal axes are not equivalent), and hence, the out-of-plane switching asymmetry of electric polarization (figure 3.7 and 3.8 respectively) translates, via the in-plane anisotropy, into an in-plane switching asymmetry in these crystals.

In addition, in order to investigate the ferroelectric reversal of the PMN-32PT, we performed in-plane reciprocal space mappings around the (001) and (1–10) X-ray diffraction reflections of a PMN-32PT substrate in pristine conditions (i.e., 0 V in Fig. 3.18) and at 0 V after applying −6 kV/cm (i.e., remanence from −6 kV/cm in Fig. 3.18). The (001) and (1–10) XRD reflections of [110] PMN-32PT correspond to the in-plane orthogonal [001] and [1–10] directions, respectively.

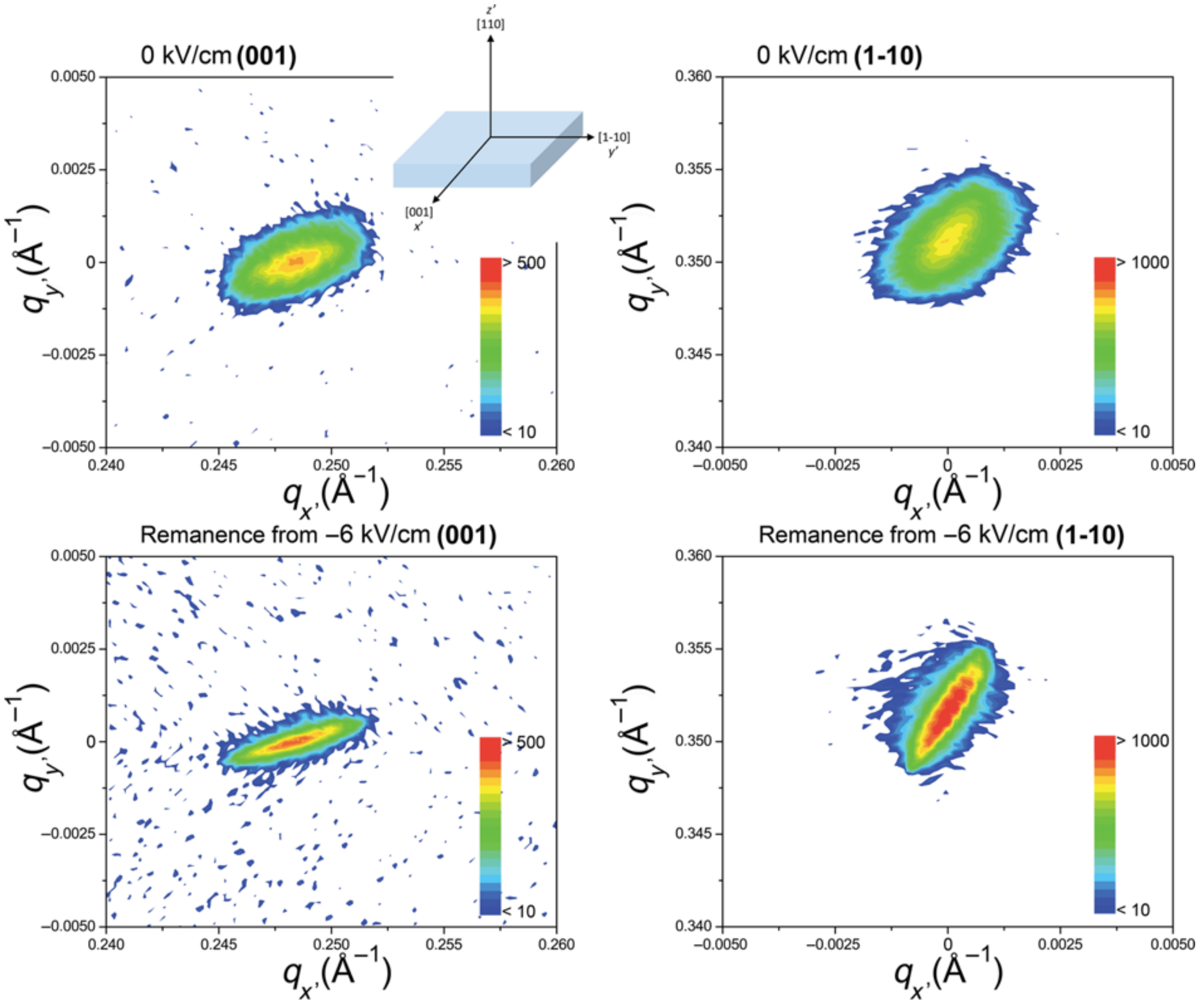

Figure 3.18: (a) and (b) in-plane reciprocal space mappings around the (001) and (1–10) planes of a pristine substrate (i.e., 0 kV/cm), respectively. (c) and (d) in-plane reciprocal space mappings around the (001) and (1–10) planes of a PMN-PT substrate at negative ferroelectric remanence (measured at 0 kV/cm after being subjected to −6 kV/cm), respectively.

This allows us to investigate the influence of the electric field on the interplanar distances d_{001} and d_{1-10} and thus on the electric field-induced deformation along the shortest and longest dimensions of the sample. To estimate these interplanar distances, the maximum intensity of the peaks is considered. Prior to the voltage application, the interplanar distances are d_{001}=4.02385 Å ($q_{x'}$=0.24852 $Å^{-1}$) and d_{1-10}=2.84725 Å ($q_{y'}$ =0.35122 $Å^{-1}$). Upon voltage actuation at negative ferroelectric remanence, d_{001} = 4.02375 Å ($q_{x'}$ =0.24852 $Å^{-1}$) and d_{1-10} =2.84275 Å ($q_{y'}$ =0.35177 $Å^{-1}$). In absolute values, along [001], the interplanar distance remains almost unaltered (0.0025% of change), whereas along [1–10], there is a permanent change of around 0.16% of the initial value. Interestingly, it is along this direction where the magnetic properties exhibit a pronounced nonvolatile behavior (loop-like dependence). In contrast to the 71° and 180° domains, the electric polarization reversal through the 109° domains takes place via a 90° twist when reversing the electric field, which results in additional stress-induced anisotropy along [1–10], thus explaining the strong asymmetry with voltage polarity of the magnetic properties in this direction and their nonvolatility upon removing the electric voltage. As can also be seen in figure 3.18, electric field actuation results in sharpened peaks. This could be ascribed to a decrease of the mosaic degree in the sample plane due to the undergone deformation. Concerning the role of the Al_2O_3 based interfacial layers in these piezostrain-mediated effects, the strain transfer from PMN-32PT to the $Fe_{75}Al_{25}$ layer should not be significantly weakened by the Al_2O_3-based interfacial layer because, as can be seen in figure 3.5 (b), this layer is very thin, and it grows rather epitaxially with the PMN-32PT.

The results reveal that, in order to properly understand magnetoelectric mechanisms in artificial FM-FE heterostructures, it is necessary to clearly assess the intrinsic polarization reversal of the ferroelectric material, especially when using PMN-32PT or other complex ferroelectric materials in these artificial multiferroic materials. Finally, even though the sign of magnetization cannot be switched with electric polarization, the magnitude of magnetization can be changed with voltage polarity (i.e., different magnitudes of electric polarization between plus and minus $\Delta V_{applied}$), implying that strain-mediated effects could eventually be used for memory purposes.

3.2 Voltage control of magnetism in patterned FeAl dots on PMN-32PT

The second part of this thesis focuses on the voltage control of magnetism in microscale patterned FeAl dots on [011]-oriented PMN-32PT substrates.

Micro and nanofabrication have opened a new opportunity for preparing structures in the mm - nm range, using robust semiconductor technology methods. To manufacture novel electronic, magnetic, mechanical, optical, or chemical/biologic devices with a wide range of applications: from sensors to computation and control, the available six orders of magnitude dimensional span from mm to nm can be used.

The key is in the structural (physical) restrictions at the nanometer scale (in one or more dimensions). Huge efforts have been made in the synthesis of magnetic nanostructures for spintronic devices. Compared to their bulk counterparts, nanoscale materials often have new and improved properties. The scaling-down process makes new properties arise as the sample size becomes comparable to, or smaller, than certain characteristic length scales (e.g., magnetic domain wall width) [30]

UV-lithography is one of the most used techniques in microelectronic manufacturing. UV-lithography utilizes the ultraviolet (UV) light source as described in Chapter 2. This technology allows for the creation of magnetic microstructures with a very precise shape, ranging from dots to lines and zig-zag patterns. Another technique used to fabricate nanoscale structures is the so-called electron-beam lithography (EBL) [31]. In this technique, a focused beam of highly energetic electrons is used to write a very high-resolution pattern, e.g., down to 8 nm, on a substrate coated with a sensitive film resist.

In this part of the thesis, we have correlated the macroscopic measurements of ferroelectric polarization (and its corresponding induced strain) with local magnetic properties as measured by Magneto-optical Kerr effect (MOKE) and Magnetic Force Microscopy (MFM), and local measurements of Piezoresponse Force Microscopy (PFM) that have allowed for a direct correlation between strain and local magnetic ordering in the patterned microstructures.

3.2.1 Heterostructure preparation

Before sample preparation steps for the UV-lithography, described in section 2.1.2, a 10nm of Cu layer is grown, by sputtering at room temperature, on [011]-oriented PMN-32PT single crystals using an AJA international, Inc. magnetron sputtering system. The deposition is carried out at a rate of around 5 Å/s. For the photolithographic process, a conventional microfabrication sequence was used. It consists of standard photolithography to define the micrometric features using a positive resist (figure 3.2.1), followed by the thin film deposition (sputtering) and liftoff.

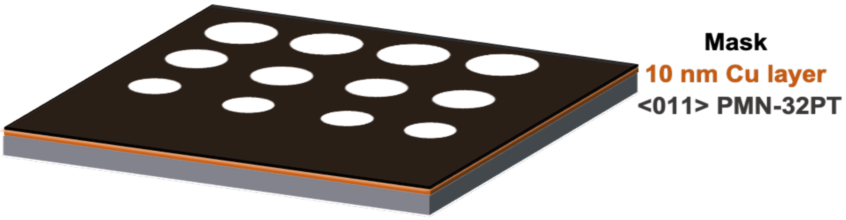

Figure 3.2.1: Schematic representation of a section of a [011]-oriented PMN-32PT (in gray) with a 10 nm Cu layer (in orange) on top and an aligned mask (represented in black).

Subsequently, $Fe_{75}Al_{25}$ dots are grown on 0.25 mm thick and 5x5 mm^2 square-shaped (10nm Cu)/ [011]-oriented PMN-32PT coated with 10 nm Cu, using an AJA international, Inc. magnetron sputtering system. Depositions are carried out at a rate of around 0.6 Å/s.

In figure 3.2.2, we represent the patterned heterostructure after the liftoff process.

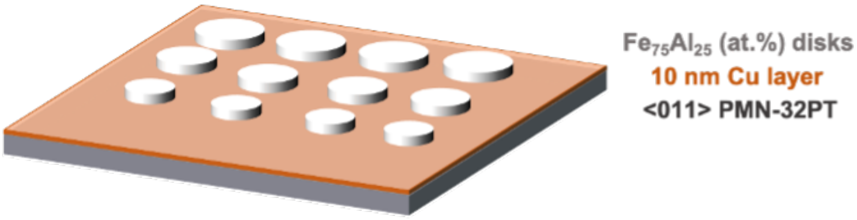

Figure 3.2.2: Schematic illustration of the patterned heterostructure. The Cu buffer layer guarantees the homogeneous distribution of the current due to its conducting character; dots with different diameters of 24, 27 and 48 μm have been grown.

3.2.2 Morphological characterization

The surface morphology characterization was carried out by scanning electron microscopy (SEM), using secondary electrons in an EI MERLIN FE-SEM microscope. In figure 3.2.3 (a), it is shown the whole array of dots with different shapes: triangles, squares, donuts, and disks. Panel (b) shows a couple of zoomed dots with a diameter of 27 (top) and 24 μm (bottom).

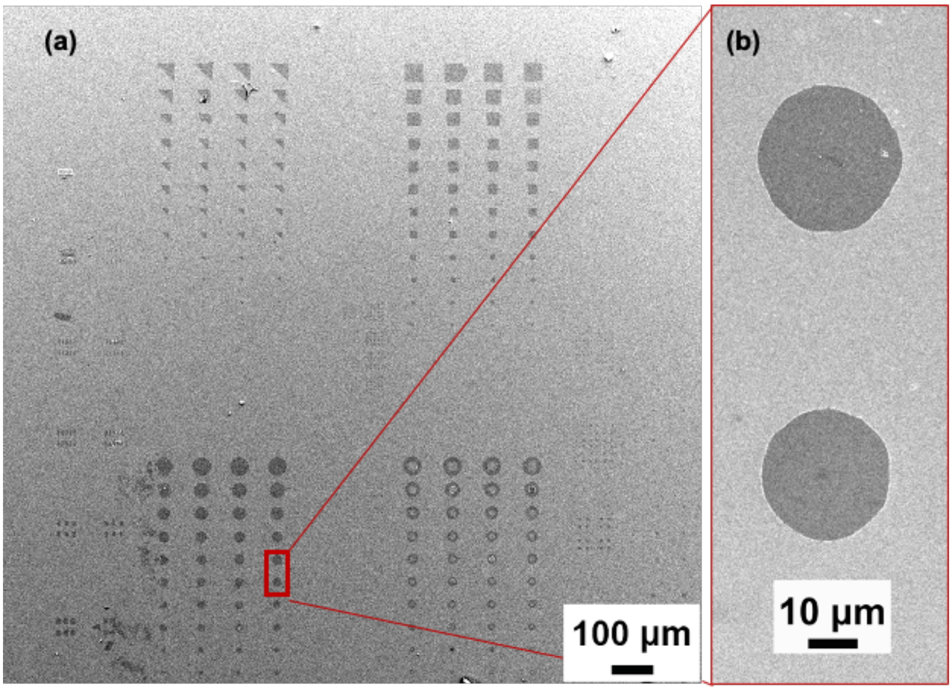

Figure 3.2.3: Scanning electron microscopy (SEM) image of all the arrays of different shapes after liftoff (a). Panel (b) shows a couple of zoomed dots with a diameter of 27 (top) and 24 µm (bottom). The bottom disk was the measured one.

3.2.3 Ferroelectric characterization

The ferroelectric polarization of the <011>-oriented PMN-32PT single crystals were characterized both, at the macroscale, by ferroelectric characterization of the full heterostructure and, also at the nanoscale, by performing local PFM on the single crystals. PFM is a contact Atomic Force Microscopy based technique in which the cantilever and tip are used as top and movable electrodes to locally apply electric fields to the sample, while simultaneously using them as mechanical sensors to detect the sample-induced deformation as an electromechanical response to the stimulus. In general, an ac field is used, and the electromechanical response is detected as the amplitude of the periodic deformation of the sample. In this way, it is possible to observe the ferroelectric distribution of domains and their evolution as a function of the electric field. While the amplitude of the PFM signal is proportional to the magnitude of the polarization (and strain response induced by electric fields), the phase is indicative of the direction of polarization, that is, whether the polarization is pointing out of the surface or towards the bulk. Finally, vectorial PFM allows us to detect the vectorial nature of the polarization by detecting not only the vertical PFM signal but also the lateral one, inducing torsional movements of the cantilever that are proportional to the in-plane component of the ferroelectric polarization that is perpendicular to the axis of the cantilever (for our experiments, that is y-axis). It is worth mentioning that while lateral PFM only arises from in-plane ferroelectric polarization, the vertical PFM signal can also have its origin in the buckling effects of the cantilever that are sensitive to the in-plane ferroelectric polarization that is parallel to the axis of the cantilever (in our case it is x-axis).

Figure 3.2.4 shows the full PFM response of the as-prepared heterostructure, i.e., with the native distribution of nanoscale domains on the surface. It is well known that some single crystals, despite having a homogeneous crystallographic phase and bulk polarization, can show some “skin layer” on their surfaces characterized by a local redistribution of polarization into small domains to facilitate polarization screening and stabilize the bulk polarization by compensating the unstable surface stray electric fields.

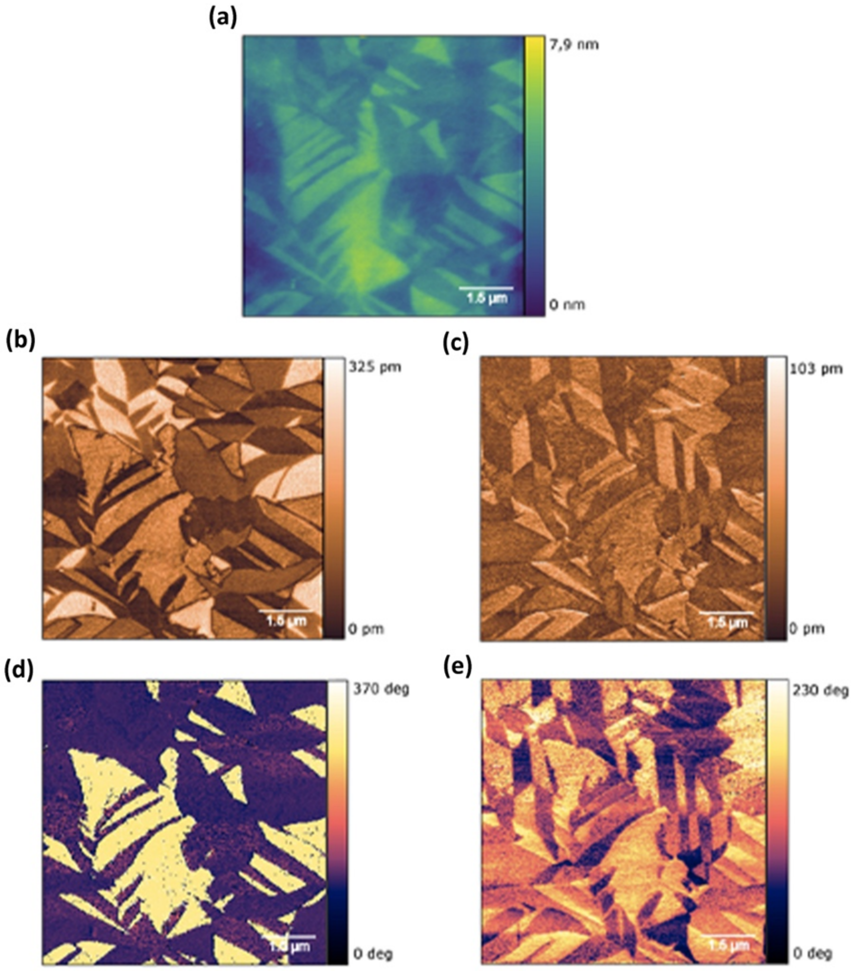

Figure 3.2.4: (a)Topography of the surface of a [011]-oriented PMN-32PT single crystal. Vertical and lateral PFM images of a [011]-oriented PMN-32 PT single crystal showing the vectorial distribution of the ferroelectric polarization in native domains before the application of electric fields. (b) and (c) correspond to the vertical PFM amplitude (b) and phase (c), respectively, showing the domains with predominant out-of-plane polarization while lateral PFM amplitude (d) and phase (e) highlight the domains with a predominant in-plane ferroelectric polarization in the y-axis direction.

It is obvious from the image that the skin layer of these single crystals is formed by a complex distribution of nanodomains, either in the shape of a_1/a_2 in-plane domains, a/c domains, or a combination of them. In an example reported by Li and co-authors [32], for the [001]-oriented film grown in a [001] cubic substrate, the shapes of a-domains are different from those of c-domains. The shape of a-domains has a tetragonal axis parallel to the film surface, while the c-domains have a tetragonal axis perpendicular to the film surface. Furthermore, depending on the degree of substrate constraint, all three types of tetragonal domains might be able to coexist, as for our sample. As a result, the domain structure has become much more complicated.

While the lateral PFM image clearly depicts the y-axis in-plane ferroelectric polarization, the vertical PFM shows a convolution of out-of-plane signal and bucking (i.e., the oscillation that occurs when domains with in-plane polarization are aligned parallel to the long axis of the AFM cantilever) arising from in-plane polarization in the y-axis that is difficult to disentangle. Furthermore, PFM amplitude images denote, with dark lines, the boundaries between domains with different polarization. In any case, this ferroelectric pattern has a strong impact on the topography which reproduces the domain morphology.

PFM is not only an imaging technique, but it can also be used for ferroelectric lithography: when applying enough V_{dc} voltages to the tip, we can locally switch the ferroelectric polarization of the sample. In this sense, Figure 3.2.5 shows the PFM image of the sample surface after applying a V_{dc} voltage of 100 V to the surface, corresponding to an electric field of E = 4 kV/cm.

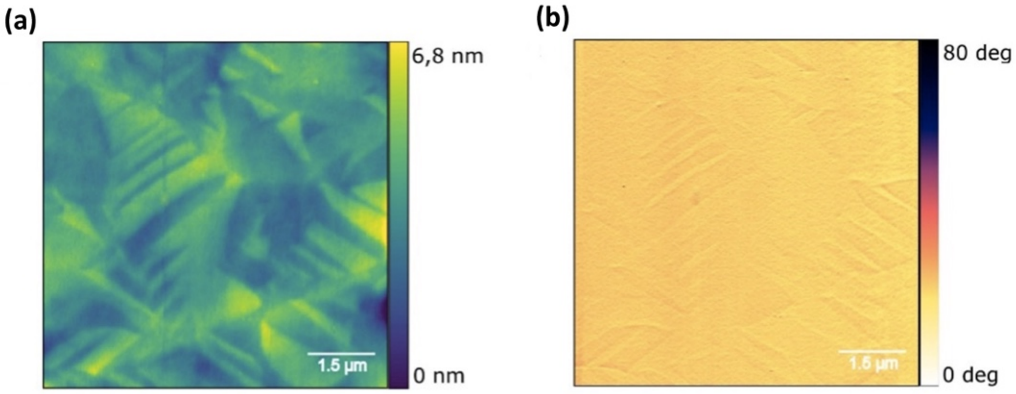

Figure 3.2.5: (a) Topography of the surface of a [011]-oriented PMN-32PT single crystal after writing the surface area with E = 4 kV/cm. Panel (b) corresponds to the vertical PFM amplitude We can see that, in this case, the ferroelectric domain distribution has disappeared, and the sample shows a uniform out-of-plane polarization pointing towards the bulk (i. e., downwards).

Upon the application of E ≥ 4 kV/cm, the ferroelectric polarization becomes uniform over the sample surface, but the reminiscent topographical features of the original domain pattern remain. This fact will be crucial for the coupling of the strain with the magnetization of the patterned FeAl magnetic disks on the surface.

Once the microstructure of the ferroelectric single crystals has been characterized, we proceed with the characterization of the macroscopic properties of the heterostructures.

Figure 3.2.6 shows, schematically, the sample and the main crystallographic directions of the 0.25 mm thick [011] PMN-32PT crystals.

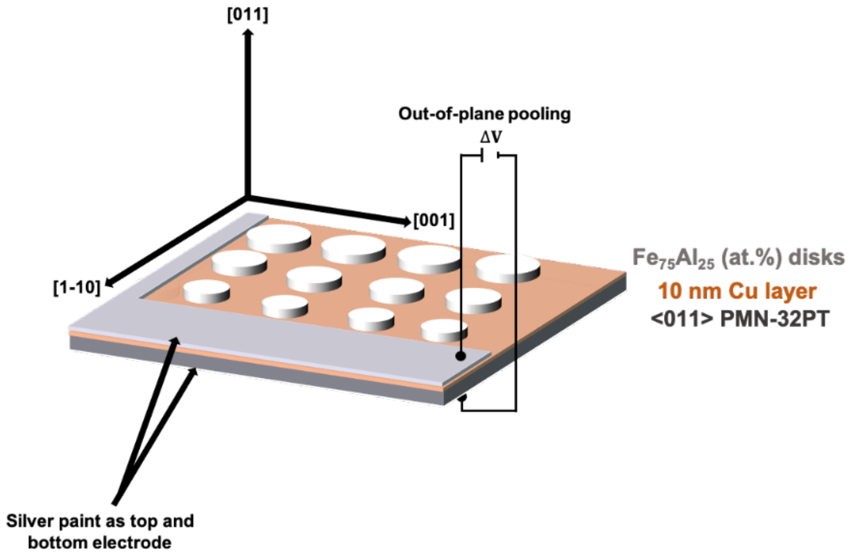
[011]
Out-of-plane pooling
ΔV
[001]
[1-10]
$Fe_{75}Al_{25}$ (at.%) disks
10 nm Cu layer
<011> PMN-32PT
Silver paint as top and bottom electrode

Figure 3.2.6: Schematic representation of the out-of-plane poling applied to the heterostructure.

As for the 0.50 mm thick PMN-32PT, the ferroelectric polarization (P) vs. the electric field (i.e., hysteresis loop) is shown in figure 3.2.7 (a). The ferroelectric hysteresis loop was measured in a quasi-static condition. Figure 3.2.7 (b) shows the dependence of the square of the electric polarization (P^2) as a function of the electric field, E.

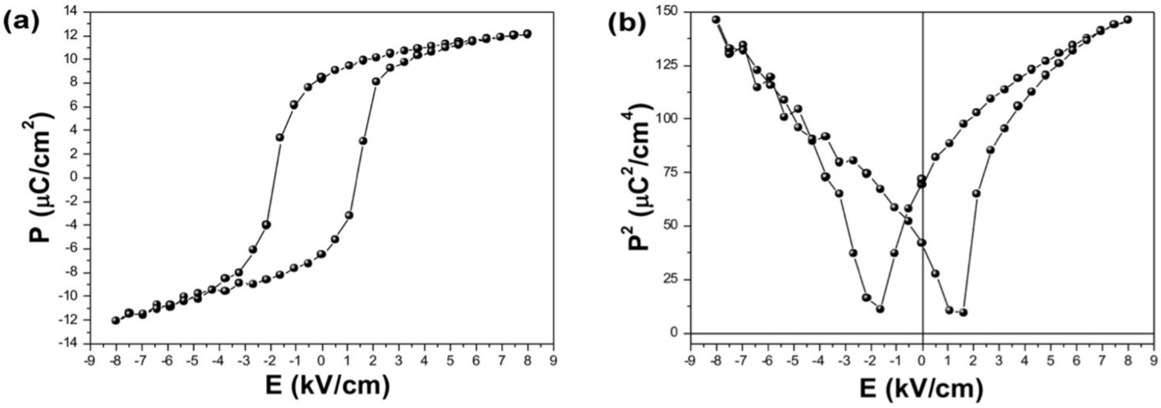

Figure 3.2.7: (a) Ferroelectric hysteresis loop (electric polarization, P, vs. applied electric field, E) of an as-deposited 50 nm thick $Fe_{75}Al_{25}$/ [011]-oriented PMN-32PT sample. (b) Square of P (which is proportional to the piezoelectric strain) vs. E.

As for the continuous sample described in paragraph 3.1.3, P^2 is proportional to the deformation (figure 3.2.7 (a)) that the PMN-32PT undergoes when subjected to an electric field due to its piezoelectricity [30]. The ferroelectric loop, shown in figure 3.2.7 (a) is more symmetrical when compared with the continuous heterostructure[12]. This could be ascribed to an improvement in electrode engineering. In contrast to the continuous sample, a 10 nm Cu layer was deposited before the patterning to guarantee the homogeneous distribution of the electric field. Furthermore, the thickness of the piezoelectric material must be considered. A 0.25mm thick <011>oriented PMN-32PTwas used, hence, the saturation of the electrical polarization should be easier to achieve in terms of voltage.

3.2.4 Magnetoelectric characterization

The magnetoelectric characterization was first carried out by in-plane magneto-optical Kerr effect (MOKE) while out-of-plane poling (i.e., the electric field is applied along the [011] direction, which is perpendicular to the sample plane). Figure 3.2.8 shows the longitudinal-MOKE (L-MOKE) characterization as a function of the applied voltage while applying the in-plane magnetic field along [001].

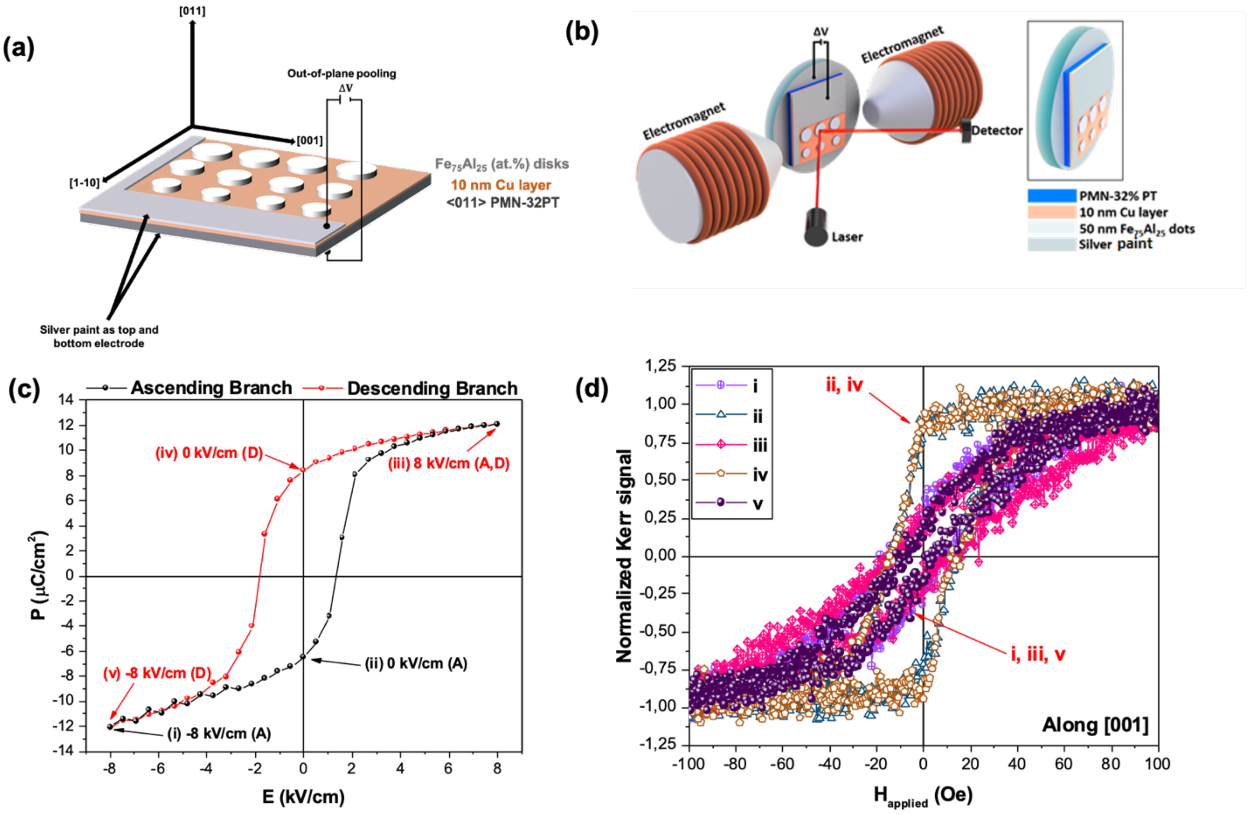

Figure 3.2.8: (a) Schematic representation of the sample, the main crystallographic directions of the 0.25 mm thick [011] PMN-32PT crystals and the out-of-plane pooling, (b) L-MOKE setup, (c) ferroelectric loop and (d) MOKE hysteresis loops recorded along [011] direction by in-plane magneto-optical Kerr effect at a given applied electric field, applied out-of-plane, for the disk with diameter of 24 μm. The loops shown correspond to the points indicated in the ferroelectric loop in panel (c), e.g., point (iv) in the ferroelectric loop corresponds to the yellow loop (iv) in panel (d). As for the continuous heterostructure, before registering the magnetic measurements, at a given electric field, the piezoelectric is always brought to ferroelectric saturation at -8 kV/cm.

The protocol applied was a little different with respect to the continuous film sample, described in chapter 3 section 2. The hysteresis loops are recorded while following the ascending branch (A), of the ferroelectric loop (see figure 3.2.7 (a)). To avoid partial or uncomplete switching of the ferroelectric polarization of the sample, and thus achieve better control of the sample state, the piezoelectric is always brought to ferroelectric saturation (-8 kV/cm, violet loop in figure 3.2.8) before applying the indicated voltages for each measurement. After that, the protocol is reversed, namely from positive to negative saturation, to collect the loops, applying a specific electric field, corresponding to the descending branch (D) of the ferroelectric loops (red line in figure 3.2.8 (c)). In table 3.2.1, the main points collected are resumed.

Saturation before measuring for Ascending branch	The electric field applied (kV/cm)
-8 kV/cm	-8
-8 kV/cm	0.8
…	…
-8 kV/cm	2.4
…	…
-8 kV/cm	4
-8 kV/cm	8
Saturation before measuring for Descending branch	**The electric field applied (kV/cm)**
-8 kV/cm; 0 kV/cm; 8 kV/cm	-0.8
-8 kV/cm; 0 kV/cm; 8 kV/cm	-1.6
…	…
-8 kV/cm; 0 kV/cm; 8 kV/cm	- 3.2
…	…
-8 kV/cm; 0 kV/cm; 8 kV/cm	-8

Table 2: Used voltage protocol. (Left column) Before each measurement the sample was brought at the ferroelectric saturation, -8 kV/cm for the loops collected following the ascending branch of the ferroelectric loop (figure 3.2.7) and, -8 kV/cm; 0 kV/cm; 8 kV/cm for the loops collected following the descending branch of the ferroelectric loop; (right column) electric field applied to collect the loops.

The most representative loops collected on a FeAl disk of 24 μm in diameter under the voltage through the ascending branch (A) of the ferroelectric hysteresis loop are shown in Fig.3.2.9.

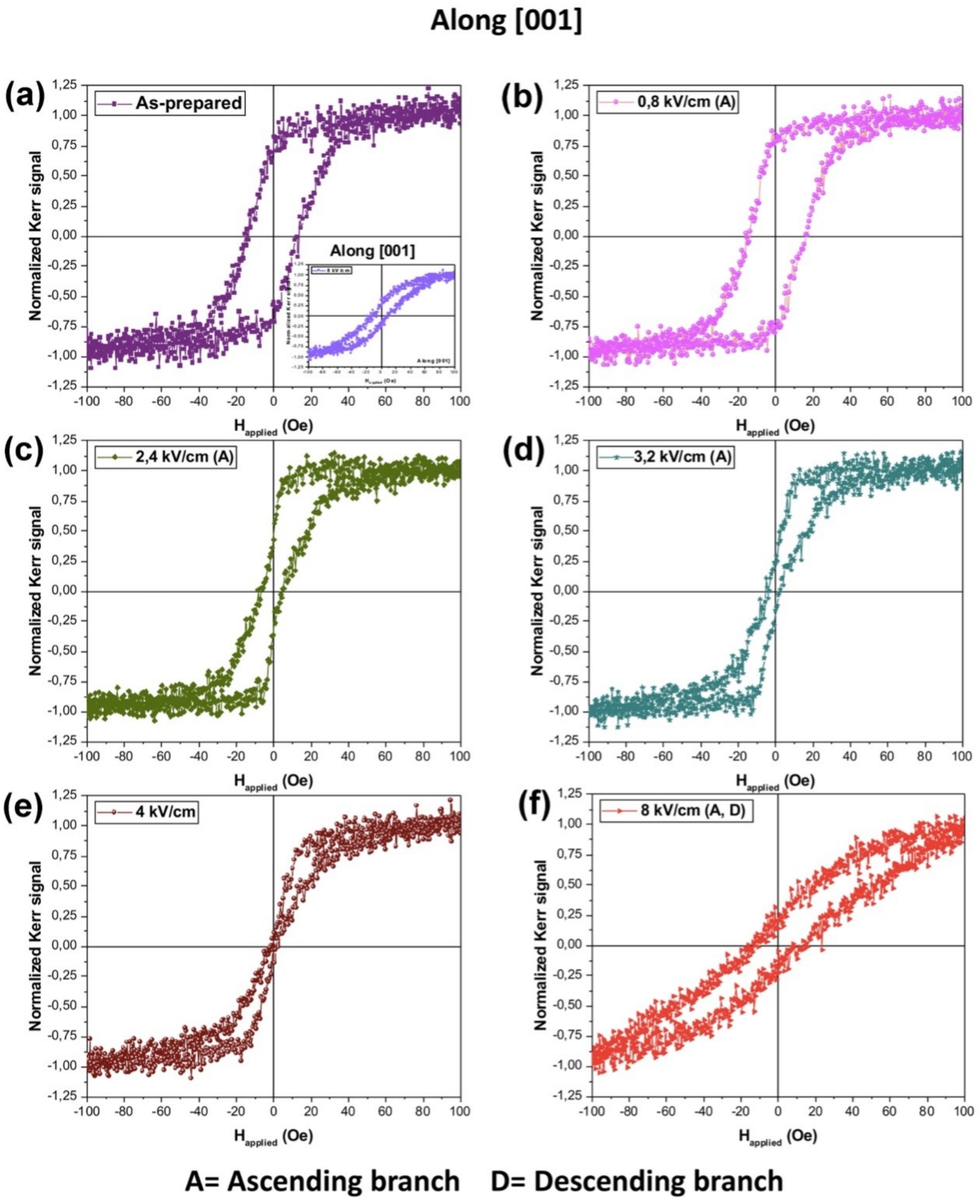

Figure 3.2.9: Hysteresis loops recorded along the in-plane direction [001] by magneto-optical Kerr effect at a given applied out-of-plane electric field. (a) MOKE loops of the as-prepared sample, in the box the sample's loop subjected to -8 kV/cm; (b) at 0.8 kV/cm; (c) at 2.4 kV/cm; (d) at 3.2 kV/cm; (e) at 4 kV/cm and (f) at 8 kV/cm. The piezoelectric is always brought to ferroelectric saturation at -8 kV/cm.

The application of increasing positive voltages leads to a progressive decrease of the coercive fields until we observe the formation of a possible vortex-like loop (i.e., constrained loop) under an electric field of 4 kV/cm for a disk of 24 μm in diameter, represented in figure 3.2.9 (e). We also performed the same measurements for the descending branch of the ferroelectric loop as shown in figure 3.2.10. We concluded that this effect seems to be independent of the direction of the ferroelectric polarization if we end up in a compressive strain situation since the formation of a vortex-like loop is also observed for a negative applied electric field of at -4 kV/cm, as shown in figure 3.2.10 (e).

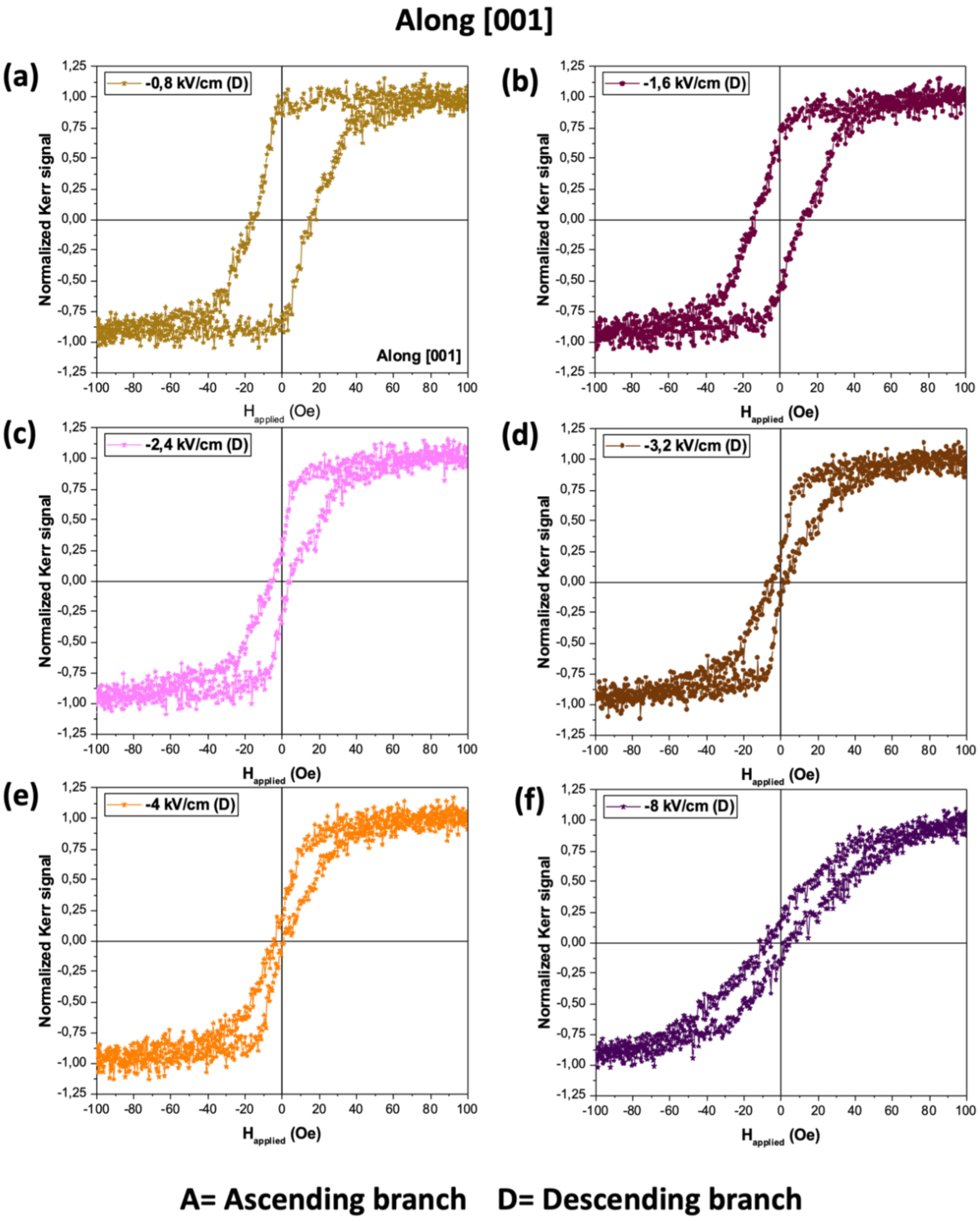

Figure 3.2.10: Hysteresis loops recorded along the in-plane direction [001] by magneto-optical Kerr effect at a given applied electric field along the out-of-plane direction, for the descending branch of

the ferroelectric loop. (a) -0.8 kV/cm; (b) -1.6 kV/cm; (c) 2.4 kV/cm; (d) -3.2 kV/cm; (e) -4 kV/cm and (d) -8 kV/cm. In this case, the piezoelectric is always brought to ferroelectric saturation at -8 kV/cm and then at 8 kV/cm before recording the loop at a given applied electric field.

Thus, we observe that, under a certain compressive strain in the [001] direction, the magnetic polarization seems to orient predominantly in a perpendicular direction to the applied magnetic field, like that of the core of a vortex-like structure.

To complete the magnetic characterization of the FeAl micropatterned disks under strain, we finally performed measurements of the magneto-optical Kerr effect by applying the magnetic field out-of-plane of the sample (i.e., polar MOKE) as represented in figure 3.2.11.

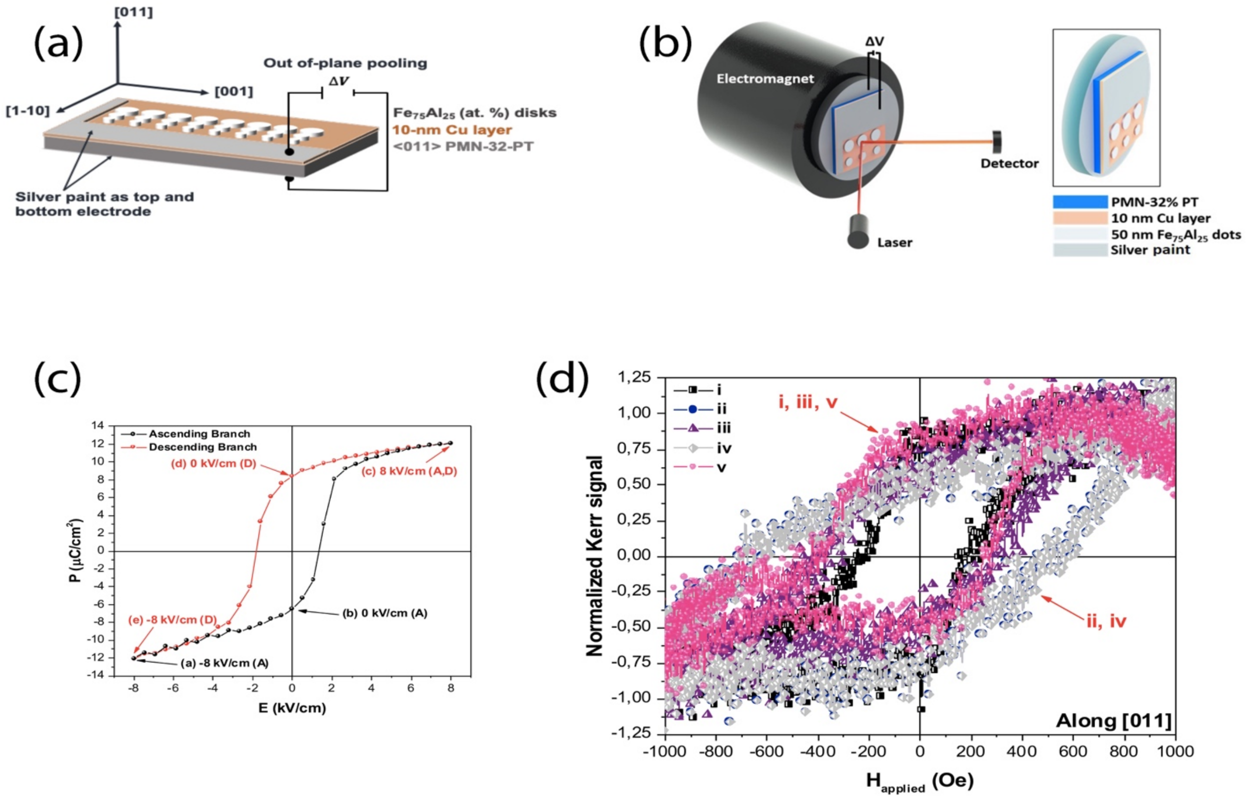

Figure 3.2.11: (a) Schematic representation of the sample, the main crystallographic directions of the 0.25 mm thick [011] PMN-32PT crystals and the out-of-plane pooling, (b) P-MOKE setup, (c) ferroelectric loop and (d) MOKE hysteresis loops recorded along [011] direction by out-of-plane magneto-optical Kerr effect at a given applied electric field, applied out-of-plane. The loops shown correspond to the points indicated in the ferroelectric loop in panel (c), e.g., point (iv) in the ferroelectric loop correspond to the light grey loop (iv) in panel (d). As for the continuous heterostructure, before registering the magnetic measurements at a given electric field, the piezoelectric is always brought to ferroelectric saturation at -8 kV/cm.

Figures 3.2.12 and 3.2.13 show the corresponding out-of-plane magnetic signals under different strains. As observed, the vortex-like loops of the in-plane [001] MOKE measurements correspond to the maximal coercive field of the magnetic configuration, indicating that the compressive strain is inducing a switch of the net magnetic moment from in-plane to out-of-plane, overcoming the shape magnetic anisotropy.

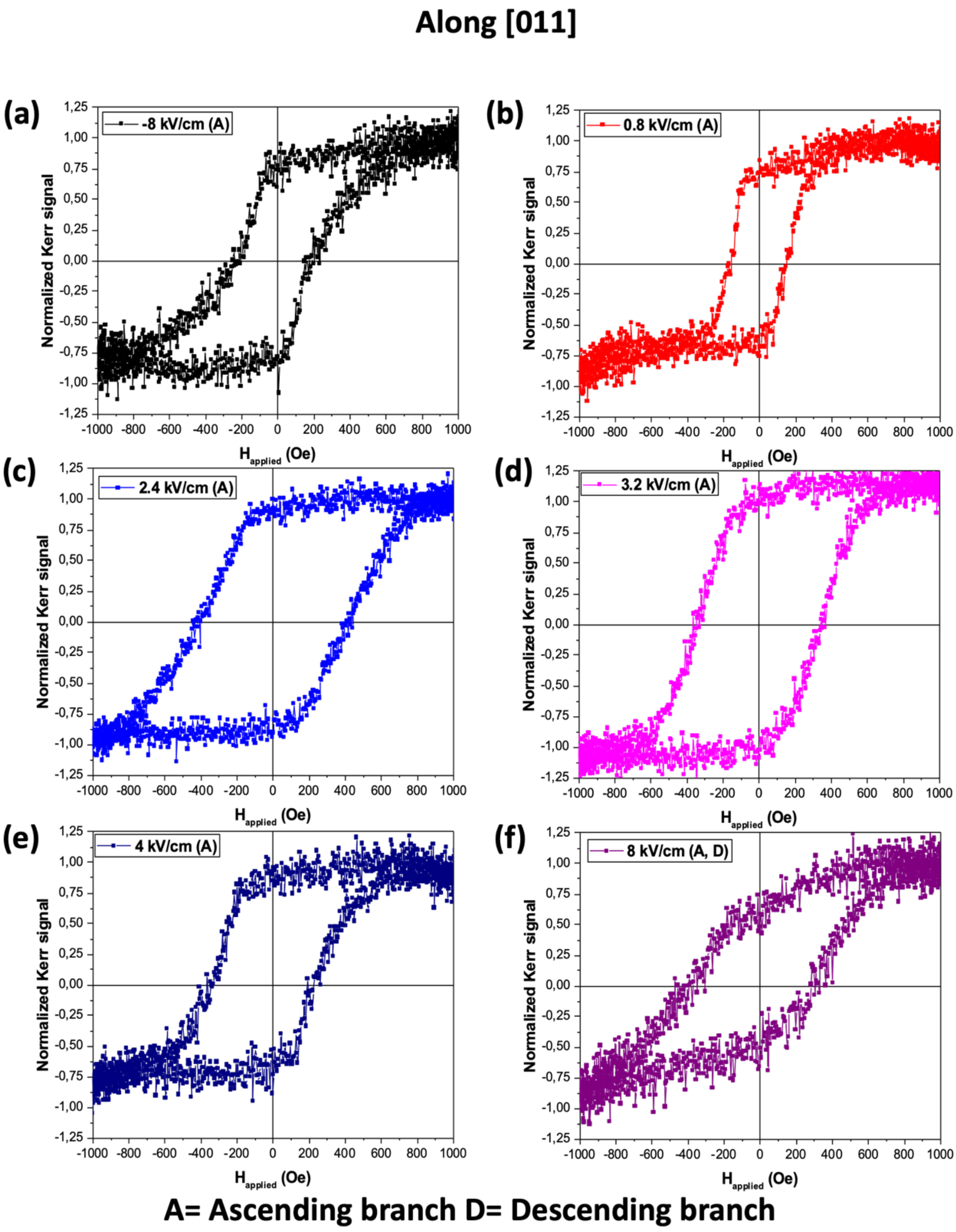

Figure 3.2.12: Hysteresis loops recorded along the out-of-plane direction [011] by magneto-optical Kerr effect at a given applied out-of-plane electric field, for the ascending branch of the ferroelectric loop. (a) -0.8 kV/cm; (b) 0.8 kV/cm; (c) 2.4 kV/cm; (d) 3.2 kV/cm; (e) 4 kV/cm and (d) 8 kV/cm. As for the in-plane measurements, the piezoelectric is always brought to ferroelectric saturation at -8 kV/cm.

Along [011]

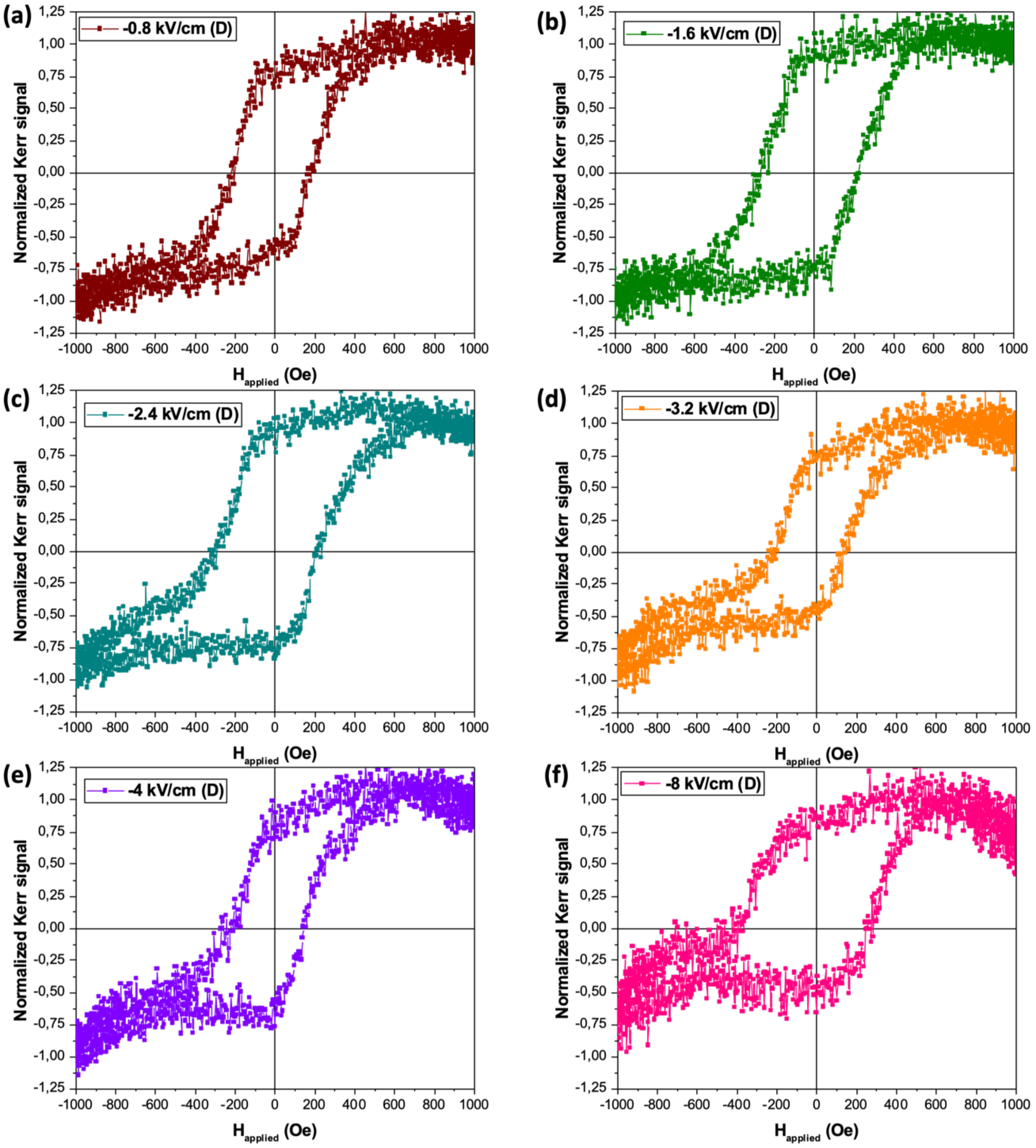

A= Ascending branch D= Descending branch

Figure 3.2.13: Hysteresis loops recorded along the out-of-plane direction [011] by magneto-optical Kerr effect at a given applied out-of-plane electric field, for the descending branch of the ferroelectric loop. (a) -0.8 kV/cm; (b) -1.6 kV/cm; (c) -2.4 kV/cm; (d) -3.2 kV/cm; (e) -4 kV/cm and (d) 8 kV/cm. As for the in-plane measurements, the piezoelectric is always brought to ferroelectric saturation at -8 kV/cm and then at 8 kV/cm before recording the loop at a given applied electric field

To clarify the evolution of the local magnetic configuration of the FeAl micro-disks under strain that lead to the observed macroscopic signals, it was required to correlate structural and magnetic properties by Atomic Force Microscopy (AFM)/ Magnetic Force Microscopy (MFM) measurements. Magnetic Force Microscopy measurements (MFM) were performed on the same investigated disks while simultaneously applying an electric field to the PMN-32PT single crystal through the delivery of high V_{dc} voltages on the Cu electrode underneath the FeAl micro-disks.

MFM is a two-pass, non-contact Atomic Force Microscopy technique that detects magnetostatic interactions between tip and sample, imaging magnetic stray fields [30]. To perform these measurements, schematic representation in figure 3.2.14, the tip is magnetized, with a magnetization perpendicular to the plane of the sample, and thus, following equation 3.2.1 becomes mainly sensitive to gradients of stray fields perpendicular to the sample surface.

$$\vec{F} = \vec{\nabla}\left(\vec{m} \cdot \vec{H}\right) \qquad \text{eq. 3.2.1}$$

$$F_z = \int_{V_{layer}} \left(M_x \frac{\partial H_x}{\partial z} + M_y \frac{\partial H_y}{\partial z} + M_z \frac{\partial H_z}{\partial z} \right) dV' \qquad \text{eq. 3.2.2}$$

In the first pass, the tip scans the surface to detect the sample’s topography. Then, in the second pass, the tip follows the morphology of the sample, as recorded in the first pass, but at a constant distance from the surface to keep the van der Waals and other surface interactions constant. In this way, the tip will only react to variable long-range interaction forces. During the second pass, the magnetostatic interactions between tip and sample are recorded, giving information about the distribution of magnetic domains on the sample’s surface. Due to the tip´s direction of the magnetization, this technique is sensitive mainly to magnetic lines perpendicular to the sample´s surface.

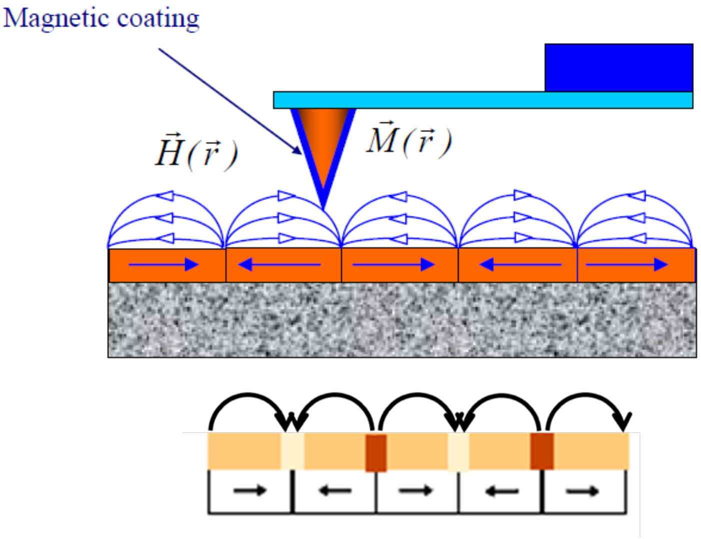

Figure 3.2.14: Schematic representation of the working principle of a MFM setup.

Figure 3.2.15 shows the topographical features of the PMN-32PT surface at the same scale as the MFM patterns. Interestingly, the initial magnetic configuration comprises an overall distribution of magnetic moments in the plane of the sample, resembling the geometrical features observed in the native ferroelectric domains pattern, and imprinted in the topography of the PMN-32PT single crystal. It thus becomes clear that there is a strong coupling of the substrate topography with the magnetization distribution already in the relaxed configuration, i.e., before the application of a strain (before voltage actuation).

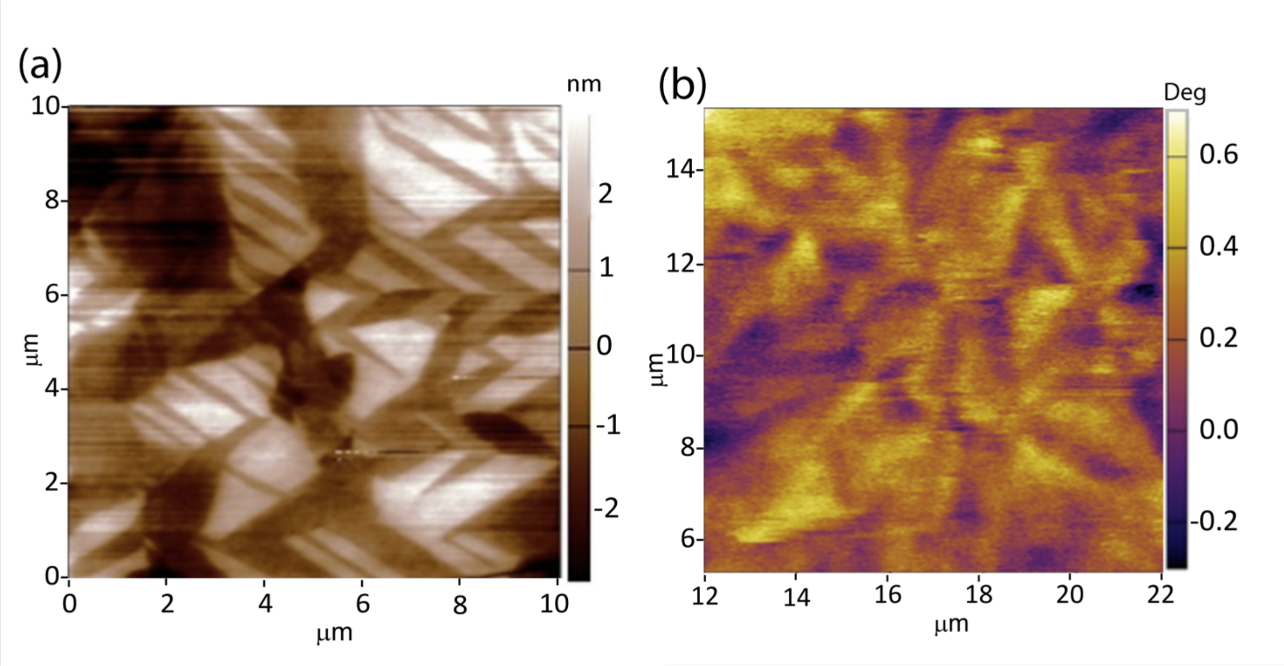

Figure 3.2.15: (a) PMN-32PT topography and (b) MFM image of a 10 T 10 μm area. The characteristic geometrical features in both cases are very similar and have the same sizes. For these measurements, we used an Asylum MFM tip with a CoPt magnetic coating and k = 2 N/m. Topography was measured at Asp/A0 = 0.7, and the MFM image was taken at h = 45 nm, using A_{mfm}/A_0 = 0.4 ratio. The x-axis of these MFM images corresponds to the [001] crystallographic in-plane direction, that is, the direction of the compressive applied strain from the single crystal relaxor substrate.

The same protocol used to acquire the loops by MOKE measurements was utilized to correlate the macroscopic magnetic measurements with the microscopic ones by MFM. The results of MFM images as a function of strain (voltage actuation) are shown in Figure 3.2.16.

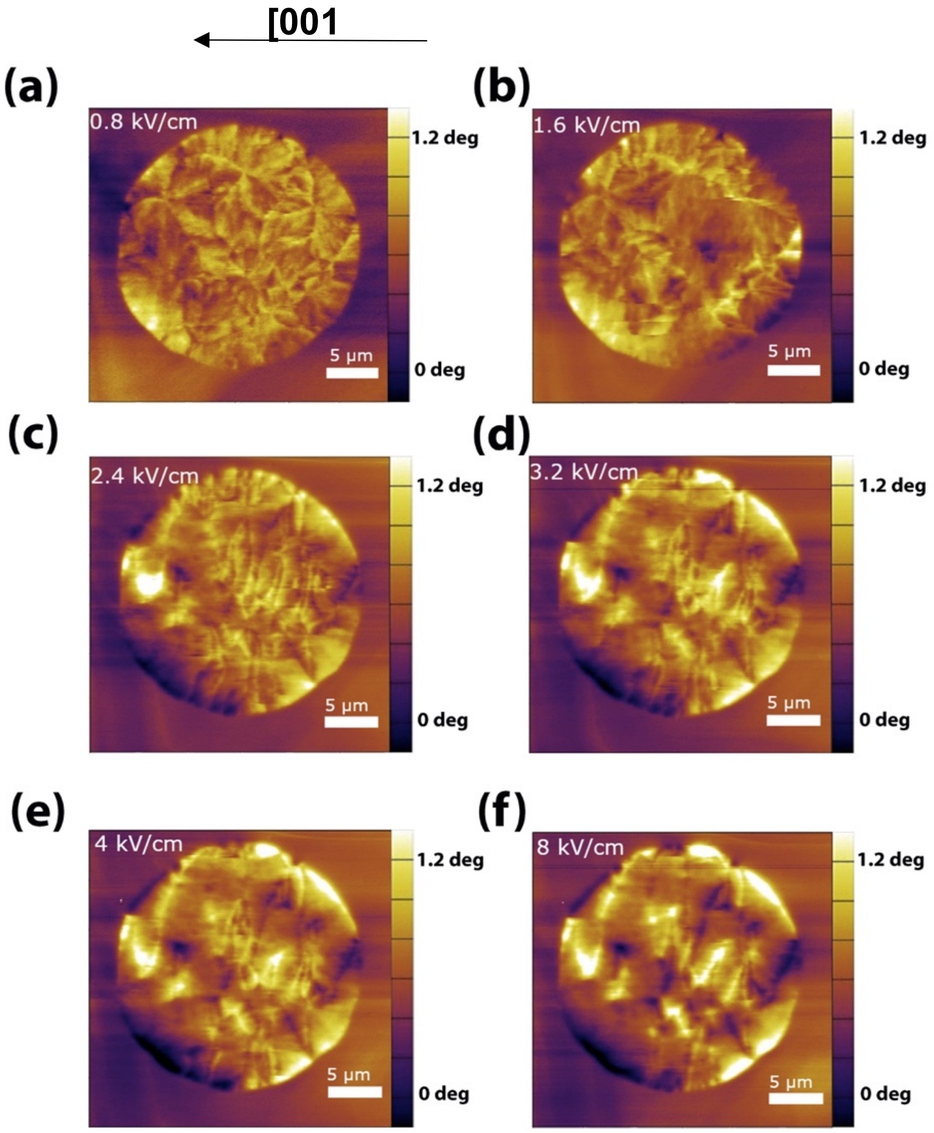

Figure 3.2.16: Magnetic Force Microscopy measurements at a given applied out-of-plane electric field. (a) -0.8 kV/cm; (b) -1.6 kV/cm; (c) 2.4 kV/cm; (d) -3.2 kV/cm; (e) -4 kV/cm and (d) -8 kV/cm.

As shown in Figure 3.2.16, the application of increasing electric fields leads to a strong change in magnetic configuration of the FeAl disks, led by the associated induced compressive strain in the [001] direction (x-axis of the MFM images). For an applied electric field of 4 kV/cm (e), we reach a configuration that is characterized by a predominant distribution of vertical bright lines in the images over imposed to a neutral background. In this case, bright contrast is associated with strong attractive interactions between the tip and the sample, indicating a dominant out-of-plane magnetization signal.

3.2.5 Discussion

The magnetoelectric behavior of 50-nm thick $Fe_{75}Al_{25}$ (at%) disks grown onto 10-nm thick Cu/[011]-oriented PMN-32PT substrates was investigated by performing in-plane Magneto-optical Kerr effect (longitudinal MOKE, or L-MOKE) along [001] direction, and by performing out-of-plane MOKE (perpendicular MOKE, or P-MOKE) along [011] direction, while applying, for both configurations, an external out-of-plane electric field, i.e., along [011] direction.

To complete the characterization, we also performed local imaging by Piezoresponse Force Microscopy (PFM) and Magnetic Force Microscopy (MFM).

A preliminary substrate study, using PFM, reveals that [011]-oriented PMN-32PT single crystal, has a “skin layer” on its surface, figure 3.2.4. Local redistribution of polarization into a small domain, in particular a complex network of nanodomains, characterizes this "skin layer." The boundaries between domains with different polarization are also shown in the PFM amplitude images.

Most single crystals exhibit bulk polarization and a homogenous crystallographic phase. However, this skin layer may be seen in some of them. The polarization screening and stabilization of the bulk polarization is made easier by the local redistribution of polarization into a small domain, which compensates for the unstable surface stray electric field.

Furthermore, using PFM as ferroelectric lithography, the ferroelectric polarization on the sample surface becomes homogenous by applying an electric field$\geq$ 4 kV/cm. The topographic features of the original model, however, remain. This will be critical for the strain-magnetization coupling of the patterned FeAl disks on the surface.

The macroscopic characterization of the heterostructure was investigated using MOKE. When a positive out-of-plane electric field was applied, along [011] direction, it causes an expansion of the single crystal. This is strongly entangled with a highly anisotropic in-plane compressive strain, that falls in the [001] direction, with tensile strain in the other in-plane axis, the [1-10]. A negative out-of-plane electric field, on the other hand, causes a tensile strain in the same direction until the applied voltages overcome the coercive field, at which point the ferroelectric polarization of the PMN-32PT single crystal is switched. The magnetic characteristics of the patterned FeAl disks are clearly affected by strain changes in the [001] direction, as seen by the strong variations in the shape of the ferromagnetic hysteresis loops and related magnetic coercive fields.

The sign of the applied electric field does not influence the formation of a hypothetical vortex-like loop. When a positive or negative electric field is applied, the magnetic hysteresis and coercive magnetic fields gradually decrease until the formation of a potential vortex-like loop (figures 3.2.9 (e) and 3.2.10 (e)). Therefore, under the compressive strain along [001] direction, the magnetic polarization orients primarily perpendicular to the applied magnetic field, like the center of a vortex-like structure.

However, when measuring in the P-MOKE configuration (i.e., when the magnetic field is applied out-of-plane, along [011] direction) the vortex-like loop is no longer observed. Indeed, the compressive strain induces a switch of the net magnetic moment from in-plane to out-of-plane, overcoming the shape magnetic anisotropy.

The evolution of the local magnetic configuration, of the FeAl micro-disks, is studied by AFM/MFM measurements. Before an electric field is applied to the substrate, the topography and MFM images shown in figure 3.2.15 confirm a correlation between the topography of the substrate and the distribution of the magnetization. Subsequently, the same protocol used for MOKE measurements was applied at the MFM setup to correlate the macroscopic magnetic measurements to the microscopic ones.

This characterization revealed a strong change in the magnetic configuration of the FeAl discs. At E=4 kV/cm, a configuration with a predominant distribution of vertical brilliant lines was achieved.

Despite the lack of micromagnetic simulations, these bright lines could be related to the formation of extended core (elongated vortices cores) lying on the z-axis. Following the observed patterns, ferromagnetic moments would be aligned primarily in the z-direction, resulting in a net magnetic moment in the x-axis near zero. Alternatively, the bright patterns can also be associated with pinned elongated Bloch domain walls separating different in-plane magnetization areas on the z-axis.

In both cases, the images show a strong asymmetry of the vortex cores or Bloch domain walls in the plane, taking preferentially the direction perpendicular to the in-plane compressive strain. This could be explained by the FeAl's magnetoelastic behavior: when a compressive strain is applied, the magnetic moments tend to rotate towards the relaxed axis, generating a strain-induced out-of-plane rotation of the polarization (figure 3.2.17).

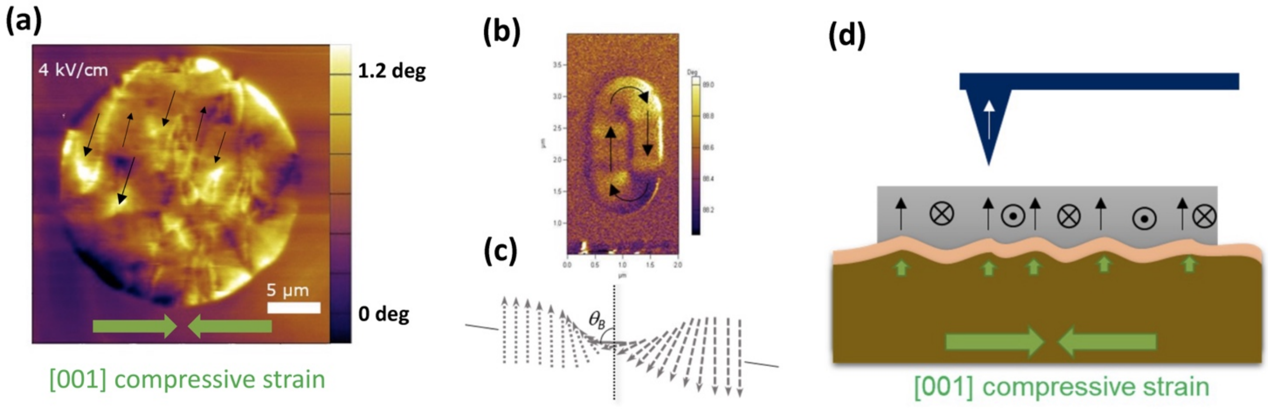

Figure 3.2.17: (a) Strained MFM image under E = 4 kV/cm, corresponding to the vortex-like magnetic hysteresis loop as measured by MOKE along the [001] direction. The compressive strain on the [001] axis forces the magnetization to align preferentially in a perpendicular direction to the strain. (b) MFM image of a vortex structure in a nanostructure pattern of permalloy in the shape of a stadium, of 1 μm width and 2 μm long. (c) Configuration of a Bloch-type domain wall with spins pointing out of the surface of the sample. (d) Scheme of the coupling between the magnetic configuration and the background topography.

The position of the shiny lines, on the other hand, remains constant over numerous hysteresis cycles as well as positive and negative applied electric fields. This indicates that the out-of-plane polarization appears to be structurally pinned and that this pinning is likely controlled by the domain boundaries, as shown by the symmetry with the PMN-32PT topographical features.

The question arises as to how topographical limits and magnetization are pinned together. Different hypotheses can be considered here. On one hand, the initial topographical features can lead to inhomogeneities on the FeAl thin film thickness. This can turn into thinner lines located on top of the domain boundaries that can accommodate out-of-plane magnetization much easier than thicker neighborhoods. A second explanation would be based on strain gradients and flexomagnetism: the topographical boundaries of the PMN-32PT substrate emerge as a distribution of peaks and valleys that translate into strong inhomogeneities on the delivered strain to the FeAl magnetic disk. Even though the polarization of the single crystal relaxor substrate is homogeneous and delivers a uniform deformation of the crystal, the nanopatterned surface will concentrate the strain into hot points at the peaks turning into locally strong strain gradients. The gradients will locally enhance the total strain transmitted from the domain boundaries onto the FeAl film thus leading to local pinning of the out-of-plane magnetization.

The results show that, despite the difficulty of studying the magnetic properties of disks due to the small signal, the interplay of in-plane magnetic actuation and voltage actuation can produce a wide range of magnetic properties, ranging from multidomain to vortex-like behavior. Furthermore, the magnetoelectric properties of these structures differ significantly from those of a continuous film of the same material, i.e., the magnetization process, and hence the hysteresis loop, maybe radically different. This allows the use of these nanostructures in fields like magnetic recording, MRAM, sensor and magnetoelectronics.

References

1. S. W. Choi, T. R. Shrout, S. J. Jang, and A. S. Bhalla, *Phys. Rev B* **100**, 29 (1989).
2. S.-E. Park and T. R. Shrout, *J. Appl. Phys*. **82**, 1804 (1997)
3. T. Wu, P. Zhao, M. Bao, A. Bur, J. L. Hockel, K. Wong, K. P. Mohanchandra, C. S. Lynch, and G. P. Carman, *J. Appl. Phys.* **109**, 124101 (2011)
4. G. Sébald, L. Lebrun, and D. Guyomar, *Phys. Rev B* **51**, 1491 (2004)
5. P. Kumar, C. Prakash, and T. C. Goel, *Sci. Technol. Adv. Mater.* **8**, 463 (2007)
6. Y. Wei, G. Yang, H. Yang, and S. Xi, *Appl. Phys. Lett.* 1**14**, 082404 (2019)
7. J. H. Westbrook and R. L. Fleischer, *Intermetallic Compounds, Structural applications of intermetallic compounds*, (John Wiley & Sons, New York, 2000), 2nd ed., Vol. 3.
8. Y. Wei, C. Gao, Z. Chen, S. Xi, W. Shao, P. Zhang, G. Chen, and J. Li, *Sci. Rep.* **6**, 30002 (2016)
9. P. Weaver and M. G. Cain, Chapter: Temperature dependence of ferroelectric and piezoelectric properties of PZT ceramics, in *Characterisation of ferroelectric bulk materials and thin films*, edited by M. G. Cain (Springer, 2014). Series in Measurement Science and Technology, Vol. 2.
10. H. Ouchi, K. Nagano, and S. Hayakawa, *J. Am. Ceram. Soc*. **48**, 630 (1965)
11. H. Ouchi, *J. Am. Ceram. Soc.* **51**, 169 (1968)
12. A. Biancoli, C. M. Fancher, J. L. Jones, and D. Damjanovic, *Nat. Mater.* **14**, 224 (2015)
13. M. Foerster, I. Fina, S. Finizio, B. Casals, A. Mandziak, F. Fauth, and L. Aballe, *J. Phys.: Condens. Matter.* **31**, 084003 (2019)
14. S. Zhang, Y. Zhao, X. Xiao, Y. Wu, S. Rizwan, L. Yang, P. Li, J. Wang, M. Zhu, H. Zhang, X. Jin, and X. Han, *Sci. Rep.* **4**, 3727 (2014)
15. S. Zhang, Y. G. Zhao, P. S. Li, J. J. Yang, S. Rizwan, J. X. Zhang, J. Seidel, T. L. Qu, Y. J. Yang, Z. L. Luo, Q. He, T. Zou, Q. P. Chen, J. W. Wang, L. F. Yang, Y. Sun, Y. Z. Wu, X. Xiao, X. F. Jin, J. Huang, C. Gao, X. F. Han, and R. Ramesh, *Phys. Rev. Lett*. **108**, 137203 (2012)
16. P. Li, Y. Zhao, S. Zhang, A. Chen, D. Li, J. Ma, Y. Liu, D. T. Pierce, J. Unguris, H.-G. Piao, H. Zhang, M. Zhu, X. Zhang, X. Han, M. Pan, and C.-W. Nan, *ACS Appl. Mater. Interfaces* **9**, 2642 (2017).
17. E. Menèndez. V. Sireus, A. Quintana. I. Fina, B. Casals, R. Cichelero, M. Kataja, M. Stengel, G. Herranz, G. Catalàn, M. D. Barò, S. Suriñach and J. Sort, *Phys. Rev. Applied* **12**, 014041 (2019) http://link.aps.org/supplemental/10.1103/PhysRevApplied.12.014041 for further structural, compositional, magnetic and magnetoelectric characterization
18. U. Bauer, L. Yao, A. J. Tan, P. Agrawal, S. Emori, H. L. Tuller, S. van Dijken, and G. S. D. Beach, *Nat. Mater.* **14**, 174 (2015)

19. D. A. Gilbert, A. J. Grutter, E. Arenholz, K. Liu, B. J. Kirby, J. A. Borchers, and B. B. Maranville, *Nat. Commun.* **7**, 12264 (2016)
20. L. Zhang, S. Zeng, X. Yin, T. C. Asmara, P. Yang, K. Han, Y. Cao, W. Zhou, D. Wan, C. S. Tang, A. Rusydi, Ariando, and T. Venkatesan, *ACS Nano* **11**, 9950 (2017)
21. Q. Zhang, X. He, J. Shi, N. Lu, H. Li, Q. Yu, Z. Zhang, L.-Q. Chen, B. Morris, Q. Xu, P. Yu, L. Gu, K. Jin, and C.-W. Nan, *Nat. Commun*. **8**, 104 (2017)
22. C. Bi, Y. Liu, T. Newhouse-Illige, M. Xu, M. Rosales, J. W. Freeland, O. Mryasov, S. Zhang, S. G. E. te Velthuis, and W. G. Wang, *Phys. Rev. Lett*. **113**, 267202 (2014)
23. J. Heider, M. Fechner, R. V. Chopdekar, C. Piamonteze, J. Dreiser, C. A. Jenkins, E. Arenholz, S. Rusponi, H. Brune, N. A. Spaldin, and F. Nolting, *Phys. Rev B* **94**, 014401 (2016)
24. I. V. Ovchinnikov and K. L.Wang*, Phys. Rev. B* **79**, 020402(R) (2009)
25. M. Zhernenkov, M. R. Fitzsimmons, J. Chlistunoff, J. Majewski, I. Tudosa, and E. E. Fullerton, *Phys. Rev. B* **82**, 024420 (2010).
26. T. Zhao, A. Scholl, F. Zavaliche, K. Lee, M. Barry, A. Doran, M. P. Cruz, Y. H. Chu, C. Ederer, N. A. Spaldin, R. R. Das, D. M. Kim, S. H. Baek, C. B. Eom, and R. Ramesh, *Nat. Mater.* **5**, 823 (2006)
27. Y. Wang, C. Nelson, A. Melville, B. Winchester, S. Shang, Z.-K. Liu, D. G. Schlom, X. Pan, and L.- Q. Chen, *Phys. Rev. B* **110**, 267601 (2013)
28. P. Marton, I. Rychetsky, and J. Hlinka, *Phys. Rev. B* **81**, 144125 (2010)
29. Z. Gareeva, O. Diéguez, J. Íñiguez, and A. K. Zvezdin, *Phys. Rev. B* **91**, 060404(R) (2015)
30. J.I. Martìn, J. Nogués, K. Liu, J.L. Vicent, I.K. Schuller, *J. Magn. Magn. Mater*, **256**, 449 (2003)
31. R.F.W. Pease, *Contemp. Phys*, **22**, 3, 256 (1981)
32. Y.L. Li, S.Y. Hu, z.K. Liu, L.Q. Chen, *Acta Mater.*, **50**, 395 (2002)

4

Conclusions

4. Conclusions

This section presents the key conclusions drawn from this Thesis, which is focused on controlling the magnetism of ferroelectric/ferromagnetic heterostructures by means of voltage rather than current. Continuous and patterned FeAl films were investigated.

4.1 Voltage control of magnetism in continuous FeAl/PMN-32PT

The magnetoelectric behavior of 50 nm thick $Fe_{75}Al_{25}$ (at. %) films grown onto [110] PMN-32PT substrates is investigated in detail by performing in-plane vibrating sample magnetometry along either the [001] or [1–10] directions of the PMN-PT while applying an external out-of-plane electric field.

The magnetic moment at saturation remains virtually unaltered with voltage, ruling out voltage-driven O migration as an operative magnetoelectric mechanism. Conversely, both the remanence (i.e., m_R/m_S) and the coercivity (H_C) exhibit a strong dependence on the applied voltage (amplitude and sign). In perfect PMN-PT crystals with symmetric electrodes such asymmetry should not exist. However, crystals are never perfectly symmetric, and the ferroelectric hysteresis measurements show that the positive and negative polarities are nonequivalent in our substrates.

Likewise, along [001], m_R/m_S and H_C show a slightly asymmetric butterflylike dependence, while along [1–10], m_R/m_S exhibits a clear looplike behavior, evidencing strong nonvolatile properties. Asymmetry can sometimes be attributed to interfacial charging effects. However, electrostatic charge effects are mostly significant when dealing with ultrathin films. Therefore, a thinner $Fe_{75}Al_{25}$ film (20 nm) grown in the same fashion was also investigated. No significant differences were observed with respect to the 50 nm thick one, so interfacial charging is ruled out as a possible origin of the asymmetry. Thus, the combination of macroscopic crystal asymmetry plus strain is left as the most plausible mechanism to modulate the magnetoelectric response of the investigated system.

Indeed, detailed structural characterization by reciprocal space mappings around the (001) and (1–10) X-ray diffraction reflections of a PMN-PT substrate reveal that the application of an electric field results in permanent strains only in the [1–10] direction. This explains the strong nonvolatility of the magnetic properties, which is linked to ferroelastic switching (consecutive 71°+109° switching) rather than single 180° switching events. 109° domain switching implies a 90° twist of the polarization when reversing polarity, thus causing a stress-induced magnetic anisotropy along [1–10], explaining the dissimilar magnetic behavior with voltage polarity along the direction, which shows irreversible and permanent strain upon removing the electric voltage.

Our results reveal that, to properly understand magnetoelectric mechanisms in artificial FM-FE heterostructures, it is necessary to clearly assess the intrinsic polarization reversal of the ferroelectric material, especially when using PMN-PT or other complex ferroelectric materials in these artificial multiferroic materials. Finally, even though the sign of magnetization cannot be switched with electric polarization, the magnitude of magnetization can be changed with voltage polarity (i.e., different magnitudes of electric polarization between plus and minus $\Delta V_{\text{applied}}$), implying that strain-mediated effects could eventually be used for memory purposes.

4.2 Voltage control of magnetism in patterned FeAl dots on PMN-32PT

The magnetoelectric behavior of 50 nm thick $Fe_{75}Al_{25}$ (at%) disks grown onto 10 nm thick Cu/[011]-oriented PMN-32PT substrates was investigated by performing in-plane magneto-optical Kerr effect (longitudinal MOKE) along [001] direction, and by performing out-of-plane MOKE (perpendicular MOKE) along [011] direction, while applying, for both configurations, an external out-of-plane electric field, i.e., along [011] direction.

When an electric field is applied, the macroscopic characterization of the heterostructure via MOKE exhibits a different behavior depending on the sign. The single crystal expands when a positive out-of-plane electric field is applied (i.e., along [011] direction). This is strongly entangled with a highly anisotropic in-plane compressive strain, that falls in the [001] direction, with tensile strain in the other in-plane axis, the [1-10].

A negative out-of-plane electric field, on the other hand, causes a tensile strain in the same direction. When the applied voltages overcome the coercive field, the ferroelectric polarization of the PMN-32PT single crystal is switched. However, the sign of the applied electric field does not influence the formation of the vortex-like loop. Nonetheless, when a positive or negative electric field is applied, the magnetic hysteresis and coercive magnetic fields gradually decrease until the formation of a vortex-like loop. Moreover, the vortex-like loop disappears when measuring in the polar-MOKE configuration.

The microscopic characterization, via magnetic force microscopy, has revealed a strong change in the magnetic configuration of the FeAl micro-disks. The vertical brilliant lines achieved at E=4 kV/cm could have two possible interpretations. First these lines could be related to the formation of an extended core (i.e., elongated vortices cores) lying on the z-axis. Second, the bright patterns can also be associated with pinned elongated Bloch domain walls, separating different in-plane magnetization areas on the z-axis. In both cases, the images show a strong asymmetry of the vortex cores or Bloch domain walls in the plane, preferring the direction perpendicular to the in-plane compressive strain. Furthermore, the position of these shine lines remains constant over numerous hysteresis cycles, for both signs.

This indicates that the out-of-plane polarization appears to be structurally pinned and that this pinning is likely controlled by the domain boundaries, as shown by the symmetry with the PMN-32PT topographical features.

Despite the difficulties of investigating the magnetic properties of these micro-disks due to the small signal, the results reveal that the interaction of in-plane magnetic actuation and voltage actuation can yield a wide range of magnetic properties, from multidomain to vortex-like behavior. Furthermore, the magnetoelectric properties are dramatically different from those of a continuous film of the same material, implying that the magnetization process, and hence the hysteresis loop could be radically different. This could allow the use of these heterostructures in fields like magnetic recording, MRAM, sensor and magnetoelectronics.

5

Future prospectives

5. Future prospectives

Several potential study lines can be identified based on the findings provided in this thesis:

- The use of ferromagnetic/ferroelectric heterostructure, such as FeAl/PMN-32PT to control the magnetism by voltage. This would allow to reduce the Joule effect. When these continuous heterostructures are exposed to an electric field, they show that the piezostrain-mediated effect is the only way to modulate the magnetoelectric response.

- Engineering the perfect heterostructure. Thickness of ferromagnetic materials (i.e., $Fe_{75}Al_{25}$ at.%) play an important rule to avoid the electronic charging effect. In addition, the alloy with large Fe contents is magnetostrictive, highly resistant to oxidation and exhibit soft ferromagnetism.

- The use of PMN-32PT as ferromagnetic material. Investigate the intrinsic polarization reversal in detail is the key to properly understand magnetoelectric mechanism in FM-FE heterostructure.

- Miniaturize the system. As the sample size gets closer to, or smaller than, certain characteristic length scales, new properties emerge as a result of the scaling-down process (e.g., magnetic domain wall width). A wide range of magnetic properties, ranging from multidomain to vortex-like behavior can be obtained.

6

Curriculum Vitae

6. Curriculum vitae

Veronica Sireus

Contact Information

Address Departament de Física, Grup de Física de Materials II, building C2, Universitat Autònoma de Barcelona

City, State 08193 Bellaterra, Spain

e-mail veronica.sireus@uab.cat

2016-Currently

Education

PhD in Materials Science

Universitat Autònoma de Barcelona, Barcelona, Spain

Group: Smart nanoengineered Materials, Nanomechanics and Nanomagnetism (Gnm^3)

Supervisors: Prof. Jordi Sort and Dr. Enric Menéndez

2013-2016

Master in Chemical Science

University of Sassari, Sassari, Italy

Master Thesis: Preparation and characterization of new materials for wine's protein stabilization

Supervisors: Prof. Gabriele Mulas and Dr. Sebastiano Garroni

2006-2013

Bachelor degree in Chemistry

University of Sassari, Sassari, Italy

Degree thesis: TiO_2-based mesoporous materials: synthesis procedures via hard templating and evaluation of photocatalytic activity.

Supervisors: Prof. Maria Pilo, Prof. Gabriele Mulas and Dr. Sebastiano Garroni.

Experience

Apr-Jul 2018

Co-supervision of the End-of-grade Thesis in Nanoscience and Nanotechnology of Manel Pelayo Garcia

Degree thesis: Controlling exchange bias in Pt/IrMn/(Pt/Co) ×3/PMN-PT heterostructures by voltage.

UAB, Barcelona, Spain

Languages

Italian	Mother tongue
English	Vantage
Spanish	Threshold

Publications

A. Quintana, E. Menéndez, M. O. Liedke, M. Butterling, A. Wagner, **V. Sireus**, P. Torruella, S. Estradé, F. Peiró, J. Dendooven, C. Detavernier, P. Murray, D. A. Gilbert, Kai Liu, E. Pellicer, J. Nogués and J. Sort.

Voltage-controlled ON-OFF ferromagnetism at room temperature in a single metal oxide film. ACS Nano, 12, 10291–10300 (2018)

E. Menéndez, **V. Sireus**, A. Quintana, I. Fina, B. Casals, R. Cichelero, V. M. Kataja, M. Stengel, G. Herranz, G. Catalán, M. D. Baró, S. Suriñach and J. Sort.

Disentangling magnetoelectric effects in engineered multiferroic heterostructures. Phys. Rev. Appl., 12, 014041 (2019)

J. de Rojas, A. Quintana, A. Lopeandía, J. Salguero, B. Muñiz, F. Ibrahim, M. Chshiev, M. O. Liedke, M. Butterling, A. Wagner, **V. Sireus**, L. Abad, C. Jensen, K. Liu, J. Nogués, J. L. Costa-Krämer, E. Menéndez, J. Sort.

Voltage-driven motion of nitrogen ions: a new paradigm for magneto-ionics. *Nat. Comm., 11, 5871, (2020*)

J.de Rojas, A. Quintana, A. Lopeandía, J. Salguero, B. Muñiz, F. Ibrahim, M. Chshiev, M. O. Liedke, M. Butterling, A. Wagner, **V. Sireus**, L. Abad, C. J. Jensen, K. Liu, J. Nogués, J. L. Costa-Krämer, E. Menéndez, J. Sort.

Nitrogen magneto-ionics (arXiv:2003.11137v1)

Congresses

January 2020

V. Sireus, E. Menéndez, A. Quintana, I. Fina, B. Casals, R. Cichelero, M. Kataja, M. Stengel, G. Herranz, G. Catalán, M. D. Baró, S. Suriñach and J. Sort. *Disentangling Highly Asymmetric Magnetoelectric Effects in Engineered Multiferroic Heterostructures.*

712. WE-Heraeus-Seminar “Energy Efficient Magnetoelectric Materials by Ionic Approaches: Fundamentals, Challenges and Perspectives” Physikzentrum Bad Honnef, Germany. Poster

November 2019

V. Sireus, E. Menéndez, A. Quintana, I. Fina, B. Casals, R. Cichelero, M. Kataja, M. Stengel, G. Herranz, G. Catalán, M. D. Baró, S. Suriñach and J. Sort. *Voltage Control of Magnetism in $Fe_{75}Al_{25}$/PMN-32PT multiferroic heterostructure*.

MMM2019, Las Vegas, United States. Poster

May 2018

V. Sireus, A. Quintana, E. Menèndez, S. Suriñach, D. Baró, J. Sort.

Voltage-Controlled Magnetism in FeAl/PMN-PT multiferroic heterostructure.

IW-MAG’18: Gavà, Barcelona, Spain. Oral contribution

November 2017

V. Sireus, A. Quintana, E. Menéndez, S. Suriñach, M. D. Baró, and J. Sort. Voltage-Controlled magnetism in $Fe_{60}Al_{40}$ (at. %)/[100]PMN-PT multiferroic heterostructure

JPhD2017. Institut de Ciència de Materials de Barcelona, Barcelona, Spain. Poster

Attendance at courses

20-26 February 2018	**Introduction to Scanning Electron Microscopy for material and life science** Servei de Microscòpia – Universitat Autònoma de Bacelona (UAB), Bacelona Spain.
19-23 March 2018	**Introduction to Transmission Electron Microscopy for material and life science** Servei de Microscòpia – Universitat Autònoma de Bacelona (UAB), Bacelona Spain.
20 February-20 June 2018	**Language course of English** Language Service - Universitat Autònoma de Bacelona (UAB), Bacelona Spain.
20 February-20 June 2018	**Language course of Spanish** Language Service - Universitat Autònoma de Bacelona (UAB), Bacelona Spain.
12 February, 24 April 2019	**Becoming a Scientific Writer: Putting Why before How** Universitat Autònoma de Bacelona (UAB), Bacelona Spain.

Courses delivered

Practical session: Thermodynamics, **Bachelor Degree in Nanoscience and Nanotechnology**

Course: 2016-2017

Practical session: Thermodynamics, **Bachelor Degree in Nanoscience and Nanotechnology**

Course: 2017-2018

Practical session: Thermodynamics, **Bachelor Degree in Nanoscience and Nanotechnology**

Course: 2018-2019

Skills and Expertise

Technique	X-Ray diffraction (XRD), Vibrating sample magnetometer (VSM), Magneto-Optica Kerr effect (MOKE), Sputtering
Image Processing	Image J, Photoshop
Graph and data Analysis	Origin Pro, X’Pert HighScore